Growth, Doping, and Characterization of ZnO Nanowires: Application in a Miniaturized Gas Ionization Sensor

Svetlana Spitsina

A Thesis
In the Department
of
Electrical and Computer Engineering

Presented in Partial Fulfillment of the Requirements
for the Degree of
Doctor of Philosophy (Electrical and Computer Engineering) at
Concordia University
Montréal, Québec, Canada

April 2013

CONCORDIA UNIVERSITY
SCHOOL OF GRADUATE STUDIES

This is to certify that the thesis prepared

By: Svetlana Spitsina

Entitled: Growth, Doping, and Characterization of ZnO Nanowires: Application in a Miniaturized Gas Ionization Sensor

and submitted in partial fulfillment of the requirements for the degree of

DOCTOR OF PHILOSOPHY (Electrical & Computer Engineering)

complies with the regulations of the University and meets the accepted standards with respect to originality and quality.

Signed by the final examining committee:

_____ Chair
Dr. A. Bulgak

_____ External Examiner
Dr. V.K. Arora

_____ External to Program.
Dr. A. Dolatabadi

_____ Examiner
Dr. Z. Kabir

_____ Examiner
Dr. L. Landsberger

_____ Thesis Supervisor
Dr. M. Kahrizi

Approved by _____
Dr. J.X. Zhang, Graduate Program Director

April 12, 2013

_____
Dr. Robin A.L. Drew, Dean
Faculty of Engineering & Computer Science

ABSTRACT

Growth, Doping, and Characterization of ZnO Nanowires: Application in a Miniaturized Gas Ionization Sensor

Svetlana Spitsina, Ph. D.

Concordia University, 2013

Semiconductor ZnO has been the subject of research for many applications for the past several years, because the material is nontoxic, biosafe, chemically stable, and biocompatible. In this work we report studies on ZnO nanowires (NWs), its fabrication and applications. Techniques are developed to control the morphology and distribution of ZnO Nanowires (NWs). We have also investigated the conductivity of nanowires and its manipulation using various doping materials and their concentrations. Fabricated nanowires have potential applications such as integration in nano optoelectronics, solar cells, gas or humidity sensors, and many other devices. In this thesis we have explored its application to develop a gas sensor based on the ionization of gases, so-called Gas Ionization Sensor (GIS).

A GIS based on metallic nanowires (NWs) had been previously designed and developed in the Micro/Nano Laboratories in the ECE Department at Concordia University. However, the reported device suffered from very low durability. The high voltages induced at the NWs tips damage the apexes (due to their thin structure) and device loses its sensitivity after several episodes of usage.

High performance GIS sensors demand specific morphology of NWs, uniform distribution, low density, and demand that NWs be made of highly conductive and chemically stable materials. In this work we have introduced ZnO nanowires to replace the metallic nanowires in the GIS. It is the core of thesis to fabricate ZnO NWs having the characteristics to improve the functioning of the GIS.

In these investigations we have focused on the electrochemical synthesis of nanowires. We used this technique due to its advantages such as low cost, high

throughput, repeatability, uniform and large area synthesis of NWs, strong adhesion of NWs to the substrate, ability to grow them with desired morphologies, as well as the possibility of effective doping during the growth. Effects of various growth parameters on the nanowire structures are investigated. Studies on doping the nanowires, p-type and n-type, were carried out. ZnO NWs with desired structures and conductivity were used to design and fabricate a GIS. The device was tested for various gases. Significantly improved performance of the GIS was demonstrated. GISs with p-type ZnO NWs illustrated high field enhancement factors because of the morphology, distribution, and conductivity of nanostructures. Also, the novel gas detectors illustrated superior sensitivity, reliability, and repeatability.

To my family

ACKNOWLEDGEMENTS

I would like to thanks my supervisor Mojtaba Kahrizi for long term dedicated consultations towards this long and arduous journey. It has been an honor for me to be his Ph. D. student. He generously contributed his time, ideas, and funding to make my Ph. D. experience productive and stimulating. I took a lot of motivation and strength from his exemplary leadership as a physicist and professor, deriving much success in completing this work.

Also, S. Prasad deserves a special word of appreciation for his technical help in microfabrication and nanotechnology laboratories. I thank my colleagues in nanotechnology lab for their support and friendship. A special mention is due to postdocs R. B. Sadeghian, I. Stateikina, A. Hajiaboli. All my ex-colleagues and present members of nanotechnology group including N. Azmoodeh, E. Fard, M. Etezad, C. Ren, N. Seirafianpour, Sh. N. Alam, F. N. Salik, B. Yaghootkar, M. Amouzgar, Parsoua, Mehdi, Aminreza, Mahsa, and Nassim were around to extend a helping hand as needed.

I gratefully acknowledge the financial support from Concordia Accelerator Award and internal funding for labs without which it was not possible to complete this work.

The last but not the least, I thank my family for their love, support and encouragement. Parents supported me in all my scholarly pursuits. My precious, caring, and loving son Sergey has provided much desired support during all stages of this Ph. D. that is ardently appreciated. There are many unsung heroes providing support and services. I salute them all.

Svetlana Spitsina
Concordia University
March 2013

Table of Contents

List of Figures

List of Tables

List of Acronyms

1D	One dimensional
2D	Two dimensional
3D	Three dimensional
AAM	Anodic Alumina Membrane
AC	Alternating Current
DC	Direct Current
EDXS	Energy-Dispersive X-ray Spectroscopy
FE	Field Emission
FE-SEM	Field Emission-Scanning Electron Microscopy
FI	Field Ionization
GIS	Gas Ionization Sensor
IHP	Inner Helmholtz Plane
MBE	Molecular Beam Epitaxy
mM	milli Molar concentration
MOCVD	Metal-Organic Chemical Vapour Deposition
NWs	Nanowires
OHP	Outer Helmholtz Plane
PDE	Partial Differential Equation
PEC cell	Photoelectrochemical cell
PLD	Pulsed Laser Deposition
PVD	Physical Vapor Deposition
SCR	Space Charge Region
SEM	Scanning Electron Microscopy

List of Symbols

F_{app}	Applied electric field	[V/cm]
V_{app}	Applied voltage	[V]
V	Applied voltage	[V]
Φ_s	Augmentation of effective work function in semiconductor due to band bending	[eV]
k_B	Boltzmann constant	[$m^2 \cdot kg \cdot s^{-2} \cdot K^{-1}$]
V_{bd}	Breakdown voltage	[V]
τ	Characteristic time for ionization	[s]
n	Concentration of charged particles	[# charged particles/cm^3]
n_e	Concentration of electrons	[#/cm^3]
n_i	Concentration of ions	[#/cm^3]
$v(f)$	Correlation factor	
λ_z	Correlation factor in Fowler-Nordheim equation	
$v(f)$	Correlation function	
x_c	Critical distance	[nm]
r_c	Critical distance between the tip and a point, where the dipole attraction is larger than or equal to the centrifugal force of the approaching gas molecule	[nm]
A	Cross-section area	
i	Current	[A]
j	Current density	[A/cm^2]
i_o	Current leaving cathode	[A]
λ_d	Decay-width correlation factor	
d	Distance between anode and cathode in capacitive device	[cm]

E	Electric field	[V/cm]
F_{vac}	Electric field in vacuum	[V/cm]
F	Electric field near the tip	[V/cm]
e	Electron charge	[C]
λ_B	Electronic-band-structure correlation factor	
E_g	Energy band gap in semiconductor	[eV]
E_F	Fermi energy level	[eV]
λ	Field penetration depth	[nm]
α	First Townsend ionization coefficient	[cm^{-1}]
a	Fowler-Nordheim coefficient	[$AeVV^{-2}$]
b	Fowler-Nordheim coefficient	[$eV^{-3/2}nm^{-1}$]
s	Interspacing in nanowires array	[nm]
γ_o	Intrinsic field enhancement factor	
I_{FL}	Ion current in field limited regime	[A]
I_{SL}	Ion current in supply-limited regime	[A]
U_I	Ionization voltage	[eV]
L	Length of nanowire	[nm]
F_{loc}	Local electric field	[V/cm]
m	Mass of the gas molecule	[kg]
r_t	Metal tip curvature	
μ_e	Mobility of electrons	[$cm^2/V{\cdot}s$]
μ_i	Mobility of ions	[$cm^2/V{\cdot}s$]
Y	Number of particles impinging on a unit surface per unit time	[$cm^{-2}{\cdot}s^{-1}$]
α	Polarizability	[$C{\cdot}m^2{\cdot}V^{-1}$]
ΔU	Potential barrier height	[eV]
r	Radius of nanowire	[nm]
ε_r	Relative permittivity	
f	Scaled barrier field	
γ	Second Townsend ionization coefficient	[cm^{-1}]
$\Phi_{semicond}$	Semiconductor work function	[eV]

λ_T	Temperature correlation factor	
T	Temperature in Kelvin	[K]
c_t	The equilibrium gas concentration near the tip	[Moles]
γ	The field enhancement factor	
E_φ	The field needed to reduce to zero a Schottky-Nordheim barrier	[eV]
φ	The metal work function	[eV]
Φ	The metal work function	[eV]
r_0	Tip radius	[cm]
P_F	Tunneling prefactor	
R	Universal gas constant	[J/(Mol·K)]
v	Velocity of the gas molecule	[nm/s]
E	Voltage of the working electrode	[V]
β	Voltage-to-barrier-field conversion factor	[m^{-1}]

1. Introduction

In this Chapter an introduction to nanoscience and nanotechnology as well as applications of nanostructures are presented. Semiconductor nanostructures, in particular the structure of ZnO nanowires and its applications, are discussed. Details of a gas ionization sensor are introduced, and finally the objectives of the thesis and its organization are elaborated at the end of the chapter.

1.1. An Overview of Nanoscience and Nanotechnology

Nanotechnology deals with fabrication of structures with dimensions in order of nanometers, 10^{-9} meter. Nanoscience is the understanding of principles behind operation at a nanoscale. The nanostructures have either one, or two, or three dimensions in nanoscale, usually in the range of 1 nm to 100 nm. Nanostructures can be synthesized from metallic, semiconductive, or insulating materials. Their categories include nanodots or nanoparticles where all three dimensions are in nanoscale, nanowires where only two dimensions are in nanoscale, and nanowalls where only one dimension is in nanoscale. Generally, in the nanoscale region most physical, chemical, mechanical, and biological properties of the materials become size dependent. Hence, most properties of the nanostructures are different compared to the bulk materials.

In semiconductors, for example, crystal and energy band structures change as the size of materials reduces from bulk to nanoscale dimensions. In these ranges quantum

effects dominate most properties of the materials. Indeed, the energies of the carriers become quantized in nanostructures. As a result, the density of states, which describes the electronic states versus energy in the band diagram, is quite different from those in the bulk materials as shown in Figure 1.1.

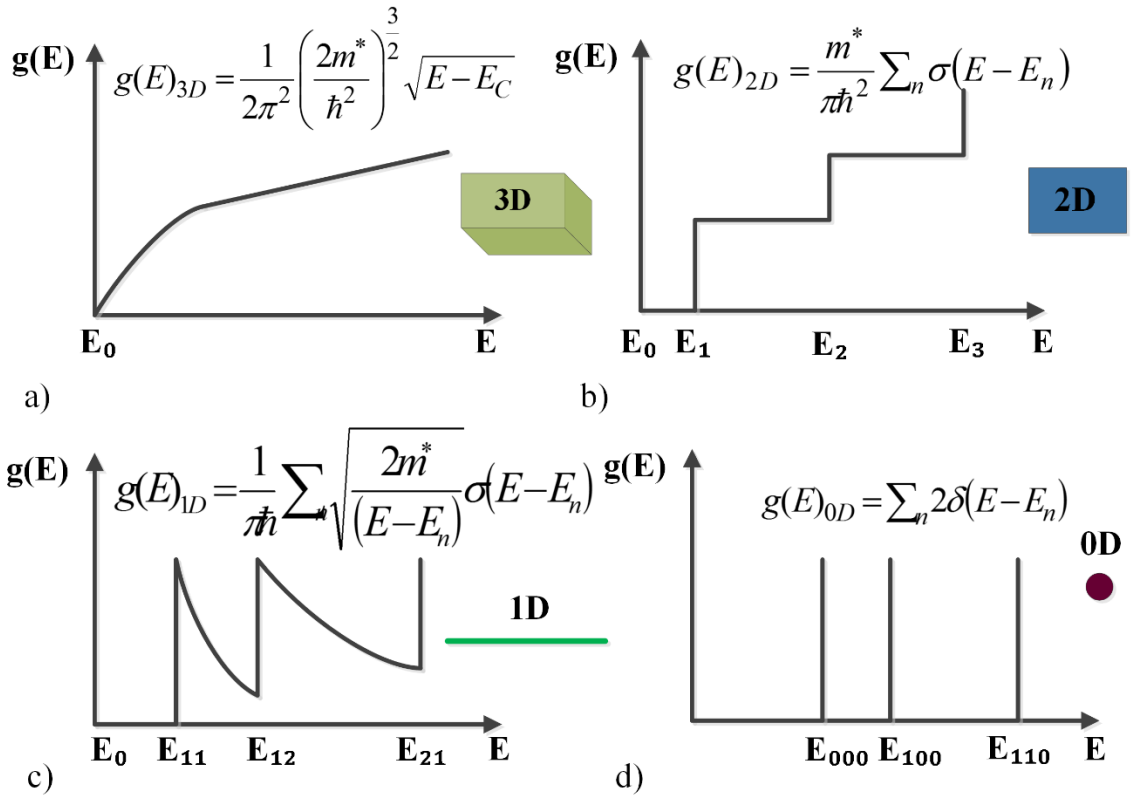

Figure 1.1. The electron density of states (g(E)) with single-valley, isotropic and parabolic band ($E_0 = E_C$) in bulk semiconductor (a), in quantum well (b), in quantum wire (c), and in quantum dot (d).

In bulk semiconductors the density of states is a continuous function as shown in Figure 1.1(a). When one of the dimensions is quantized, as in a quantum well, the constant energy surface for single-valley, isotropic band in k-space from spherical shape, as it was in bulk material, becomes an area in two nonquantized directions. As a consequence, the density of states becomes a step function (σ(E)), and has constant values between energy

levels. One-dimensional semiconductor such as nanowires has two quantized dimensions. The constant energy for single-valley, isotropic band in k-space is represented by a continuous energy along the length of nanowire. Thus, the density of states is proportional to $1/\sqrt{\Delta E}$ between energy levels. In the case of a one-dimensional system like nanowires, which are the research topic in this work, electrons travel along the NWs through fixed energy channels. They can generate ballistic or diffusive transport. Ballistic transport happens when there is no scattering of electrons; the mean free path is larger than the length of the channel. In this case, the length of the nanowire channel is usually less than 1 micrometer. However, with increasing of the NW length the electron transport becomes diffusive. Thus, the increasing aspect ratio of nanowires leads to increase in resistance in this 1D nanostructure. Quantum dot is confined in all three spatial directions. Therefore, density of states depends on the number of confined levels and is described as the series of delta functions (δ-functions).

Nanostructures such as metallic nanowires and nanotubes are investigated by many researchers, and they have already found their way into the fabrication of many novel devices like gas ionization sensors, field emission devices (because of high field-enhancement factor), switches (because of the lack of resistance in the channel along the nanowires), and in biosensors due to large sensitivity [1, 2]. Semiconductor nanowires are successfully applied in bio, gas, humidity, temperature sensors, solar cells, nanolasers, light-emitting diodes [3]. Nanowires made of piezoelectric materials are employed as nanogenerators. Ferromagnetic nanowires are used in bio applications, as drug delivery systems, and as microwave resonators [4].

The semiconducting nanowires can be elemental such as Si and Ge, or compound, comprising binary semiconductors such as AlP, AlAs, GaP, GaAs, InP, ZnO, or ternary semiconductors such as $Al_xGa_{1-x}As$. Among them ZnO nanowires have illustrated that their applications are quite broad because of their electrical, optical, and piezoelectrical properties. As ZnO nanowires are the central topic in this research work, an introduction to their properties and their applications is presented in the following section.

1.2. Zinc Oxide Nanowires

ZnO NWs have high popularity, because this material is nontoxic, biosafe, chemically stable, and biocompatible. Pure ZnO is colorless and clear. ZnO (II-VI group) is a compound semiconductor, and is n-type without intentional doping. The n-type conductivity of ZnO arises because of the intrinsic defects and residual impurities such as hydrogen interstitials, which remain in the material during the fabrication process [5, 6]. The density of states (DOS) in intrinsic ZnO is illustrated in Figure 1.2.

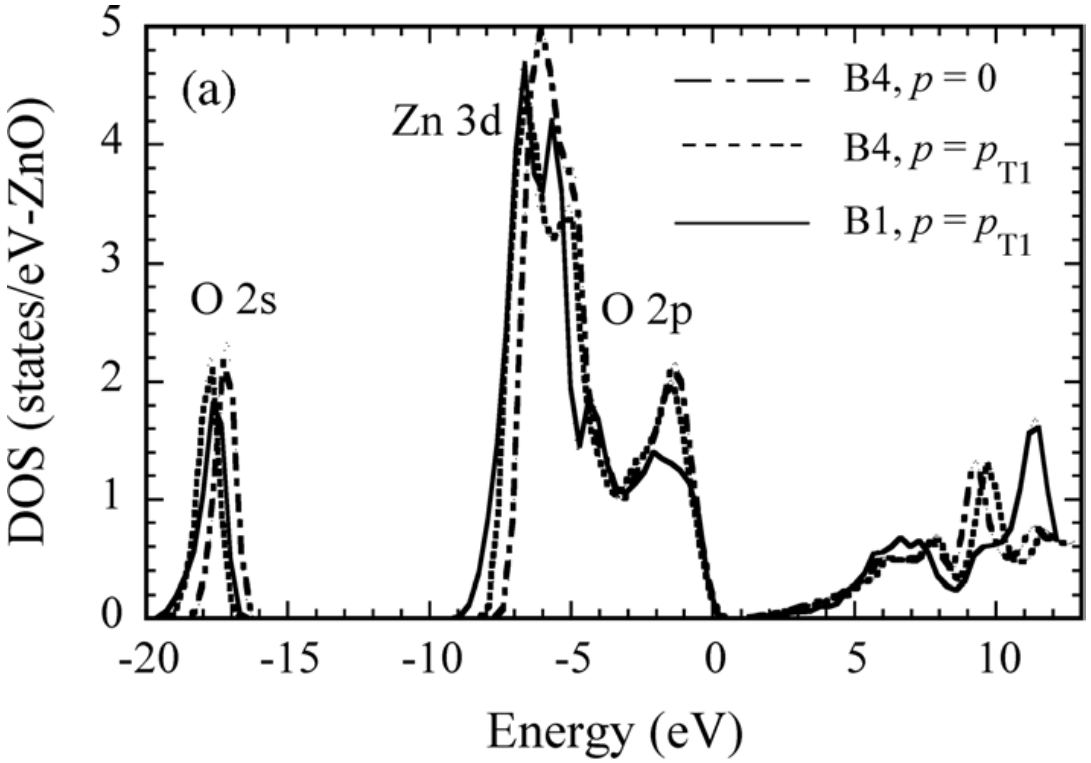

Figure 1.2. DOS in wurtzite hexagonal structured ZnO (B4) [7].

Hydrogen interstitials lie in the conduction band of ZnO and serve as donors. ZnO has a direct wide bandgap (3.37 eV at T = 300K), where the bottom of the conduction band is formed from the 4s levels of Zn^{2+} and the top of the valence band is built from the 2p orbitals of O^{2-}. It has strong ionic bonding and exciton binding energy of 60 meV [5, 6]. The bond polarity in ZnO occurs because of the strong negativity of the oxygen and different ionic bond radii of zinc and oxygen ions 0.074 and 0.14 (Pauling scale), respectively. Thus, ZnO is a piezoelectrical material due to its noncentrosymmetric crystal structure and bond polarity. Also, its bond polarity supports the wurtzite structure instead of the zinc-blend formation of ZnO. Specifically, the tetrahedral arrangement of ZnO occurs, where each zinc ion is connected to four oxygen neighbour ions and vice versa as illustrated in Figure 1.3.

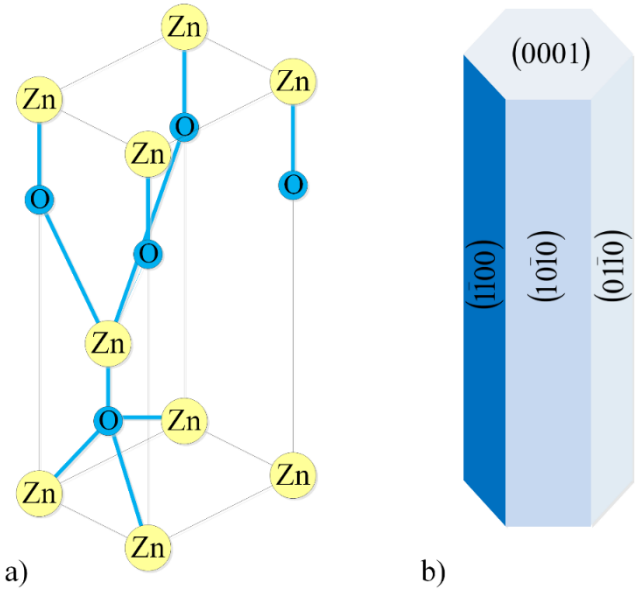

Figure 1.3. Schematics of ZnO crystal structure: illustration of primitive unit cell (a) and the crystal shape of ZnO NW with indicated Miller-Bravais indices (b).

Hexagonal wurtzite lattice with polar hexagonal axis, Zn^{2+}-terminated (0001) and O^{2-}-terminated $(000\bar{1})$, is uniaxial and is classified by its hexagonal closed packed structure 6 mm point group symmetry (international notation), and by its space group $P6_3mc$ as illustrated in Figure 2.1(b). Also, ZnO has high thermal stability (melting point = T_m = 2242 K), because the coherent energy of ZnO per bond is 7.52 eV [6].

To fabricate one dimensional structures of this material vapour phase processes or wet chemical processes can be employed. The vapour phase processes include molecular beam epitaxy (MBE), metal-organic chemical vapour deposition (MOCVD), the sputtering method, pulsed laser deposition (PLD), infrared irradiation, and thermal decomposition. These processes involve high temperature, high vacuum, expensive equipment, and have low throughput. On the other hand, wet chemical methods, like electrochemical and hydrothermal processes, are performed at low temperature. Also,

they are not expensive. Further, the electrochemical process has potential in uniform and large area synthesis of nanowires, fast growth, and strong adhesion to the substrate. The electrochemical growth of ZnO NWs in templates and self-assembled ZnO NWs on planar or patterned substrates were extensively investigated. For example, studies of template-based growth of ZnO NWs in anodic alumina membranes (AAM) [8, 9] and in polycarbonate membranes [10] were performed. Self-assembled ZnO NWs were studied, and reported [11 - 13]. Conducted research on the n-type [14, 15], p-type [16], and ferromagnetic n-type [17] ZnO NWs, which were obtained during wet chemical synthesis, are already reported.

Synthesized ZnO NWs with varying morphologies because of polar charges at the surface, various conductivities, magnetic properties, and distributions are used to fabricate various nanodevices. It is known that the morphology of ZnO NWs, their doping types, and their uniform distribution control the photoluminescence, field-emission, magnetic, and electrical characteristics of novel applications. Thus, novel devices with improved performance, repeatability, and durability can be engineered by controlling ZnO nanowires shape, their distribution and their conductive parameters. Recently, ZnO NWs have been extensively investigated for integration in various devices such as nanogenerators [18 - 21], nanolasers [22 - 25], solar cell electrodes [26 - 31], gas sensors [32 - 38], humidity sensors [39, 40], biosensors [41, 42], and as templates used to grow other nanostructures [43 - 45]. Furthermore, the achievement of the ferromagnetic ZnO NWs at room temperature by doping of NWs using dopants as Mn, Co [46], or Fe opens the door for applications in spintronic and spinplasmonic devices.

In numerous novel applications including gas sensors, biosensors, solar cell electrodes, nanolasers, and nanogenerators, well distributed and highly oriented NWs are of crucial importance. Also, controllable fabrication of p-type or n-type ZnO NWs is important for applications in nano optoelectronics and solar cells. It is the goal of this thesis to design the synthesis of ZnO nanowires with specific parameters best suited in fabricating a low voltage, low cost, and sensitive gas ionization sensor (GIS).

1.3. Gas Sensors

A gas sensor monitors the atmospheric air with the intention to prevent contamination of the surroundings, to protect people from hazardous gases in industrial milieu, in aircraft, and in living environments, and to detect the loss of the planetary atmospheric gases to outer space in exosphere. Gas detectors that identify the concentration of gas or gas mixtures are divided into optical, electrical, and chemical types. Optical gas detectors are based on detection of gas concentration by the power change of the light which was transmitted through the gaseous atmosphere. Chiefly, detected light power is compared with a reference light, and the difference between the powers of transmitted and a reference light provides the information about the quantity of the gas in the atmosphere. Since, difference between the reference and transmitted light is proportional to the concentration of gas. Chemical gas detectors are based on the change of the current in the electrochemical cell attributable to the voltage variation between working and reference electrodes at different amounts of the gas. The electrolyte of the chemical gas sensor is usually aqueous acid or salt. Electrical gas detectors are divided into physical and chemical. Chemical type gas detector is based on the adsorption of the gas. When the

active layer between two oppositely charged electrodes adsorbs the gas, its resistance value is changed. This variation in resistance of the active layer depends on an amount of the adsorbed gas. Thus, gas concentration is measured by detection of changes in resistance of the gas detector. The physical type of gas sensor is based on the physical phenomena, ionization of gas molecules. Gas ionization inside GIS operates at high electric field generated between capacitive plates of this device and lead to creation of conductive path between oppositely charged plates. In general, a gas ionization sensor (GIS), made of two parallel plates, has a big drawback as it needs a very high voltage (few thousands volts) to breakdown the gases. However, the latest developments in nanotechnology field gave GIS the advantage: the nanostructures placed on one or both capacitive plates create high local electric fields, which result in ionization of the gases at comparably very low voltages. The fundamental design of gas ionization sensor employed for detection of the gas with incorporated nanowires is illustrated in Figure 1.4.

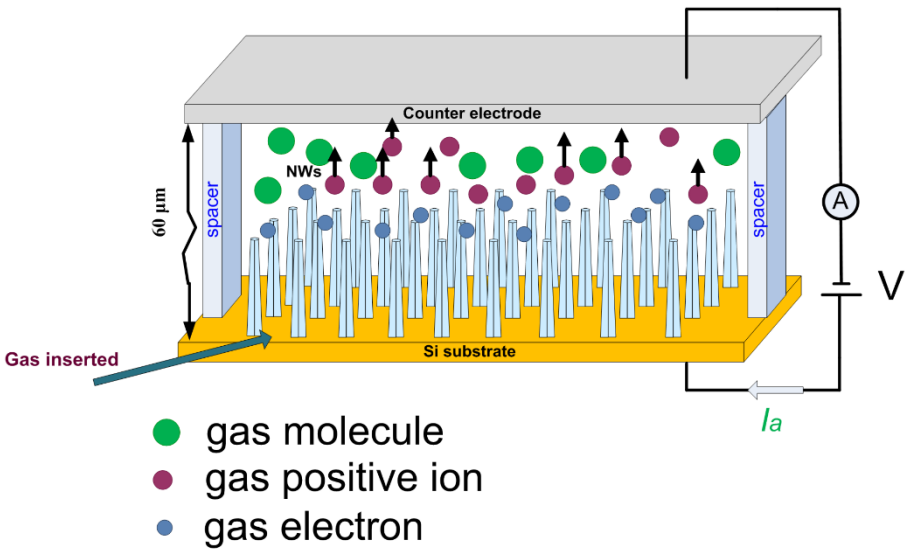

Figure 1.4. Schematics of gas sensor based on gas ionization.

Two capacitive oppositely charged plates with incorporated NWs as anode and insulating spacer are essential components of this gas detector. The insulating spacer is placed between capacitive plates to separate the oppositely charged electrodes and let gas enter into the active area of the gas detector. High electric field created between capacitive plates ionizes the gas in the gap. The resulting breakdown voltage created by the ionic current is generated between two oppositely charged capacitive plates and represents the amount and type of the gas.

Normally, the desired characteristics of the gas sensor include fast response, reversibility, low noise, selectivity, superior durability, low power consumption, non-intrusiveness, noncontaminating properties, low cost, and high throughput during fabrication. However, the available gas detectors have diverse disadvantages such as high power, high cost, susceptibility to contaminants or to changes in environmental conditions, detection of only high gas concentrations or identification of limited range of gases, etc.

Ongoing research on low and uniform distributed nanowires incorporated into GISs in Concordia University (Micro/Nano fabrication laboratories at ECE department) resulted in numerous publications on metallic nanowires, silicon hillocks, and metal oxide nanowires integrated into GIS [1, 47 – 56]. Grown arrays of metallic nanowires result in observed breakdown voltages around 30-40 Volts compared to thousand volts between two parallel plates. However, the application of metallic nanowires has drawbacks such as low durability, since high electric field intensity destroys the sharp tips of the metallic nanostructures. Therefore, the replacing of metallic nanowires with

materials, which have strong binding and very high stable structure, may be a solution to the above issue.

1.4. Research Objectives

The goals of this research is

- to study the morphology and the type of ZnO NWs conductivities for various applications; in particular, for the purpose of designing a novel gas ionization sensor to detect low concentrations of gases at a low voltage. The investigations are focused on the electrochemical synthesis of ZnO NWs with controlled morphology, distribution, and doping. The electrochemical technique to grow ZnO NWs is chosen because of its beneficial characteristics such as low cost, high throughput, repeatability, uniform and large area synthesis of NWs, strong adhesion of NWs to the substrate, ability to grow them with desired morphologies, as well as possibility of effective doping during the growth. n-type or p-type ZnO NWs with designed shapes and uniform distributions integrated into gas ionization sensor can improve the performance of a gas ionization sensor, because the high doping, specific shape and distribution can significantly increase the induced local electric field inside the gas detector.
- using the best suited arrays of ZnO NWs to design and fabricate a low voltage, low cost, and sensitive GIS. Performance, selectivity, sensitivity, recovery time, reversibility, and durability of the gas detectors were examined.

1.5. Organization of the Dissertation

The research efforts to synthesis ZnO NWs with certain specifications are presented in following chapters. Chapter 2 gives basics of electrochemistry and the methodology of the electrochemical growth of zinc oxide nanowires. In Chapter 3 we present the synthesis and doping of the nanowires. Chapter 4 illustrates the experimental work done to fabricate ZnO NWs. Chapter 5 discusses gas ionization, field emission, and field ionization phenomena in gases. We have also reported the simulation results on field emission by nanowires. It follows with the design, fabrication and characterizations of the GIS based on ZnO nanowires. Finally, Chapter 6 concludes with the noteworthy achievements and the contributions of the present work, and directions for future research.

2. Background on Electrochemistry

In this chapter an introduction to electrochemistry is given, including the derived equations, which characterize the electrochemical process in terms of the ionic transport and rates of the reactions. The electrochemical process to fabricate ZnO NWs will follow.

2.1. Overview of Electrochemical Processes

Generally, an electrochemical system comprises a potentiostat connected to the electrochemical cell. The potentiostat is the device engaged to control a three electrode cell. The electrochemical system can work in two modes: potentiostatic mode and galvanostatic mode. In potentiostatic mode this hardware measures and controls the voltage difference between the working electrode and the reference electrode, and it measures the current flow between the working and counter electrodes versus time at a given area of the deposition. In galvanostatic mode, constant current is applied between the working electrode and the auxiliary electrode, and the potential between working and reference electrodes versus time is recorded.

Another element of the electrochemical system is the electrochemical cell. It includes anode, cathode, and reference electrode as shown in Figure 2.1.

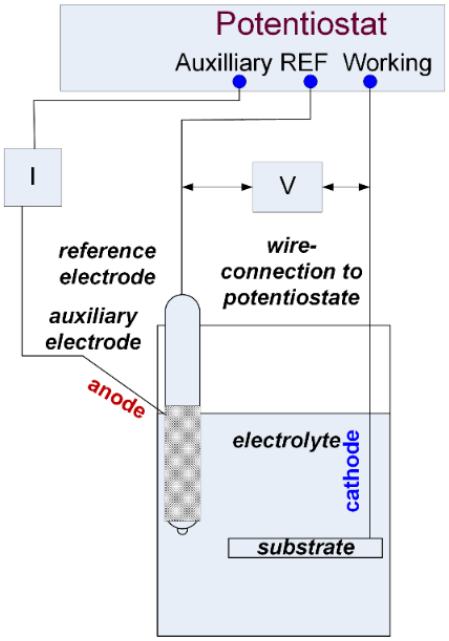

Figure 2.1. Schematic of the electrochemical cell.

An electrolyte consists of dissolved chemicals in deionized water, which dissociate and form both positive and negative ions. The anode can be any conducting material but mostly a platinum gauze is used. The cathode can be a metal or a semiconductor electrode. The next component of the electrochemical cell is the reference electrode which has a stable potential drop and is used to measure the working electrode potential. The homogeneous electrolyte is made of an equal numbers of cations and anions. The electroneutrality condition is given as

$$\sum_{i=1}^{s} z_i C_i = 0 \tag{2.1}$$

where z_i is the elementary charge of the i_{th} species, C_i is the concentration of the i_{th} species, and s is the number of species inside the electrolyte [57].

Furthermore, at an applied electric field, the reactive processes of reduction and oxidation take place inside the electrochemical cell. A reduction process happens, when

an electrode provides electrons into the electrolyte, where the minimum energy of the electrons is comparable with the energy of the orbital of the valence electron to be received. Thus, the negatively charged electrode provides electrons with energy equivalent to the energy of the orbital of the valence electrons. Oxidation happens when electrons from a higher orbital of the species inside the electrolyte move to the lower energy level provided by the positively charged electrode. In other words, the chemical species in solution provide electrons. Oxidation or reduction occurs at critical potentials, which depend on the standard potentials of the species inside the electrolyte [57]. An example of the reduction process in an electrochemical cell is when the positive ions of zinc accept the electrons and reduce at the negatively charged electrode, when the electrode potential is equal to or more negative with respect to the standard electrode potential. This reaction is expressed as

$$Zn^{2+} + 2e^{-} \rightarrow Zn(s) \tag{2.2}$$

An example of the oxidation process is when zinc donates electrons to electrode and produces ions. The applied potential in an electrochemical cell is equal to or higher than the positive standard potential. An oxidation reaction is expressed as

$$Zn(s) \rightarrow Zn^{2+} + 2e^{-} \tag{2.3}$$

In general, the standard electrode potential (E°) (potential of reduction or oxidation process, redox) of any element in the electrolyte is expressed as

$$E^{0} = -\frac{\Delta G^{0}}{nF} = \frac{RT}{nF} \ln K_{eq} \tag{2.4}$$

where ΔG° is the standard Gibbs energy change in the electrochemical cell reaction, which is defined as the difference between the sum of Gibbs energies of the products and

the sum of Gibbs energies of the reactants, n is the number of ions in electrochemical cell, F is the Faraday constant (96485 C/mol), and nF is the charge involved in the chemical reaction, R is the ideal gas constant (8.314 J/K·mol), T is the temperature in Kelvin, and K_{eq} is the equilibrium constant [57].

The thermodynamics of the reactions inside the electrochemical cell depends on the interfacial region between the working electrode and the electrolyte. Indeed, the interfacial region in solution consists of the double layer which is created between the working electrode (semiconductor or metal) and an electrolyte [57]. The double layer comprises the inner layer (Helmholtz layer), which is composed of solvent molecules and other species (ions or molecules) that are specifically adsorbed, and diffuse layer, which extends from the Helmholtz layer into the bulk of the solution [57]. The Helmholtz layer is defined by the inner Helmholtz plane (the place where the electrical centers of the specifically adsorbed ions are located) and outer Helmholtz plane (the location where centers of the solvated ions are placed (solvated ions are ions surrounded by solvent molecules)) as shown in Figure 2.2 [57].

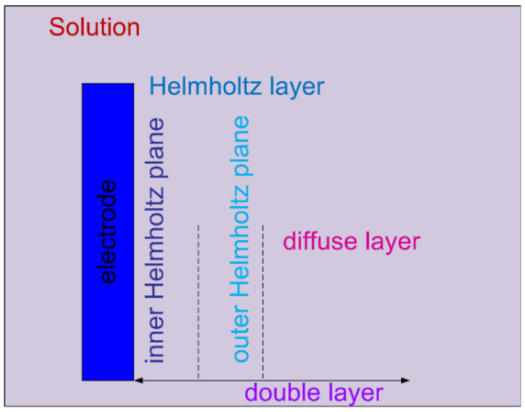

Figure 2.2. The interfacial region in a solution is the double layer. It consists of diffuse and Helmholtz layers, where Helmholtz layer comprises inner and outer Helmholtz planes.

The total excess charge density on the solution side is the sum of inner layer and diffuse layer charge densities and equals to negative value of the charge density on the metal or semiconductor surface. The interfacial region in the semiconductive working electrode comprises the space charge region (SCR) and surface states, which contribute to the charge creation. In the case of the metallic electrode, the charges are available on the surface without any voltage drop in the SCR. When the charges set on both sides of the interfacial region have equal and opposite sign, equilibrium is reached inside the electrochemical cell [58]. Without applied potential, electrons cannot enter the ions due to a high level of the ionic energies [59]. When external voltage is applied, the changes in the value of the density and charge carriers involved in the transport across the interface occur. Ohmic or rectifying contact arises between working electrode and electrolyte. On the electrolyte side, modification of the character and density of the ions electrostatically adsorbed at the surface of a working electrode happens [58]. On the working electrode the changes in the surface density of free carriers and the appearance of the band bending in the case of the semiconductive working electrode occur as illustrated in Figure 2.3.

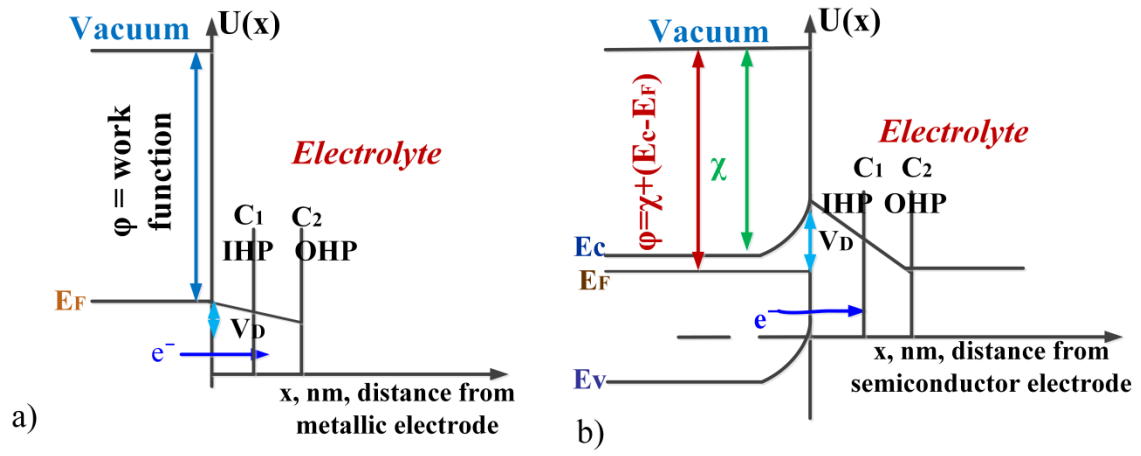

Figure 2.3. The energy schematics of a) the interfacial region in metallic electrode and b) the interfacial region in n-type semiconductor electrode under applied negative external voltage.

Figure 2.3 illustrates the potential drop in the Helmholtz layer. The inner and outer Helmholtz planes (IHP, OHP) represent two capacitors in series (C_1, C_2) created by charged particles as shown in Figure 2.3. The capacitive surface between the working electrode surface and OHP has equal amount of the charges with different sign. Helmholtz assumed linear voltage drop (V_D) in vicinity of the charged surface; however, the experimental results showed the exponential character of the voltage drop in this inner layer. At applied negative potential on the metallic working electrode the electrons with the ionic energy near or below the Fermi level tunnel through the working electrode into ions creating the current as illustrated in Figure 2.3 (a) [59]. For metallic electrode, the charge transport is fast. In the case of the semiconductor working electrode, the electrochemical reaction rates are limited due to the potential barrier present between a semiconductor and an electrolyte.

In general, the flux inside the electrochemical cell is created because of the applied electrochemical potential, and it is expressed as

$$J_i = -\left(\frac{u_i T k_B}{e} \nabla C_i + u_i z_i C_i \nabla \phi \right) = -\left(\frac{u_i RT}{F} \nabla C_i + u_i z_i C_i \nabla \phi \right) \tag{2.5}$$

where J_i is the molar flux in mol/(sec·cm²), F is the Faraday constant ($F=eN_A$), R is the ideal gas constant ($R = k_B N_A$), k_B is the Boltzmann constant ($1.38 \cdot 10^{-23}$ $m^2 kgs^{-2} K^{-1}$), N_A is Avogadro number, u_i is the molar mobility in cm²/(V·sec·mol) of species i ($u_i = \mu_i / N_A = \frac{D_i q}{k_B T N_A}$, where q is the total charge, μ_i is the mobility (cm²/V·sec) of species i). Also, ionic current equals the ion flux multiplied by the charge it carries. Accordingly, the current density (j_i) is defined as the molar flux multiplied by the total molar charge, $z_i F$, and it is given as

$$j_i = z_i F J_i = -(z_i u_i RT \nabla C_i + u_i F z_i^2 C_i \nabla \varphi) \tag{2.6a}$$

$$j_i = -F z_i D_i \nabla C - D_i \frac{F^2 z_i^2 C_i}{RT} \nabla \phi \tag{2.6b}$$

Equations (2.6a) and (2.6b) represent the current density in terms of molar mobility and in terms of diffusion coefficient, respectively. Total flux of the electric charge in the electrochemical cell is the current density (j_c), and it is given as

$$j_c = F \sum z_i J_i \tag{2.7}$$

where $\sum$ is summation over all i species in electrochemical cell.

Note that current inside the electrochemical cell is governed by the rates of mass transfer from the bulk solution to the electrode surface and the electron transfer at the electrode surface, where chemical reactions precede or follow the electron transfer [58]. Mass transfer modes include migration (movement of the ions under the influence of an electric field), diffusion (movement of the chemical species under the influence of the chemical potential gradient), and convection (stirring or hydrodynamic transport, and forced convection) [58]. Essentially, the surface reactions involved in the current creation are adsorption, desorption, or crystallization (electrodeposition). The Nernst-Planck equation describes the current inside electrochemical cell comprising all three mass transfer modes, and it is given as

$$\mathrm{i} = \mathrm{A} \sum\nolimits_{\mathrm{i}} \mathrm{j_i} = \frac{\mathrm{F^2 A}}{\mathrm{RT}} \cdot \nabla \phi \sum_{\mathrm{i}} \mathrm{z_i^2 D_i C_i} + \mathrm{FA} \sum_{\mathrm{i}} \mathrm{z_i D_i \nabla C_i} + C_i v(x) A \tag{2.8}$$

where A is the cross-section area, R is the ideal gas constant (8.314 J/(mol·K)), D_i is the diffusion coefficient (cm²/s), ∇C_i is the concentration gradient in the solution, $\nabla\phi$ is the potential gradient, z_i and C_i are the charge and the concentration of the i^{th} species,

respectively, and υ(x) is the velocity (cm/s) with which a volume element in a solution moves along the axis [60]. As it was discussed above the ionic current comprises the oxidation and reduction reactions on the same electrode, and it is expressed in the Buttler-Volmer equations of current which includes the kinetic rate constants:

$$i = nFA\left(k_a[Ox] - k_c[\mathrm{Re}\,d]\right) \tag{2.9a}$$

$$k_c = k_{0,c}\exp\left[-\frac{\alpha_c nF}{RT}\left(E - E_0\right)\right] \tag{2.9b}$$

$$k_a = k_{0,a}\left[\frac{\alpha_a nF}{RT}\left(E - E_0\right)\right] \tag{2.9c}$$

where A is the surface area of the electrode in m², k_a is the reaction rate in the forward direction, k_c is the reaction rate in the backward direction, [Ox] is the concentration of the oxidant, [Red] is the concentration of the redactor, n is the number of electrons transferred, E_0 (in V) is the standard potential of the redox reaction, E is the applied potential, k_0 (in m/s) is the standard rate constant of the electrode ($k_{0,c}=A'\exp(-\Delta G_{a,0}/RT)$ for oxidation and $k_{0,a}= A'\exp(-\Delta G_{c,0}/RT)$ for reduction), and α_a and α_c are the transfer coefficients of each redox couple [60]. The kinetic rate constants depend on the applied potential and on the value of the standard rate constant. Finally, the electrochemical system is fully specified by set of Poisson-Nernst-Planck Equations, which characterize transport inside the electrochemical cell, and it is given as

$$\frac{\partial C_i}{\partial t} = \nabla\left[D_i\left(\nabla C_i + \frac{z_i e C_i}{k_B T}\nabla\phi\right)\right] = D_i\left[\nabla^2 C_i + z_i\frac{F}{RT}\nabla\cdot\left(C_i\nabla\phi\right)\right] \tag{2.10a}$$

$$-\nabla\cdot\left(\varepsilon\nabla\phi\right) = \sum_i z_i e C_i \tag{2.10b}$$

where Equation (2.10a) is the general conservation of mass and describes the influence of an ionic concentration gradient and electric field gradient on the flux of the chemical species (ions) inside the electrochemical cell, and Equation (2.10b) is the charge density in the electrochemical cell and describes the free charge density defined by Poisson equation and by mean (volume averaged) ion concentrations summing up all the ions in the volume. In order to control the flux of charged species different variables can be altered in the electrochemical process as shown in Figure 2.4.

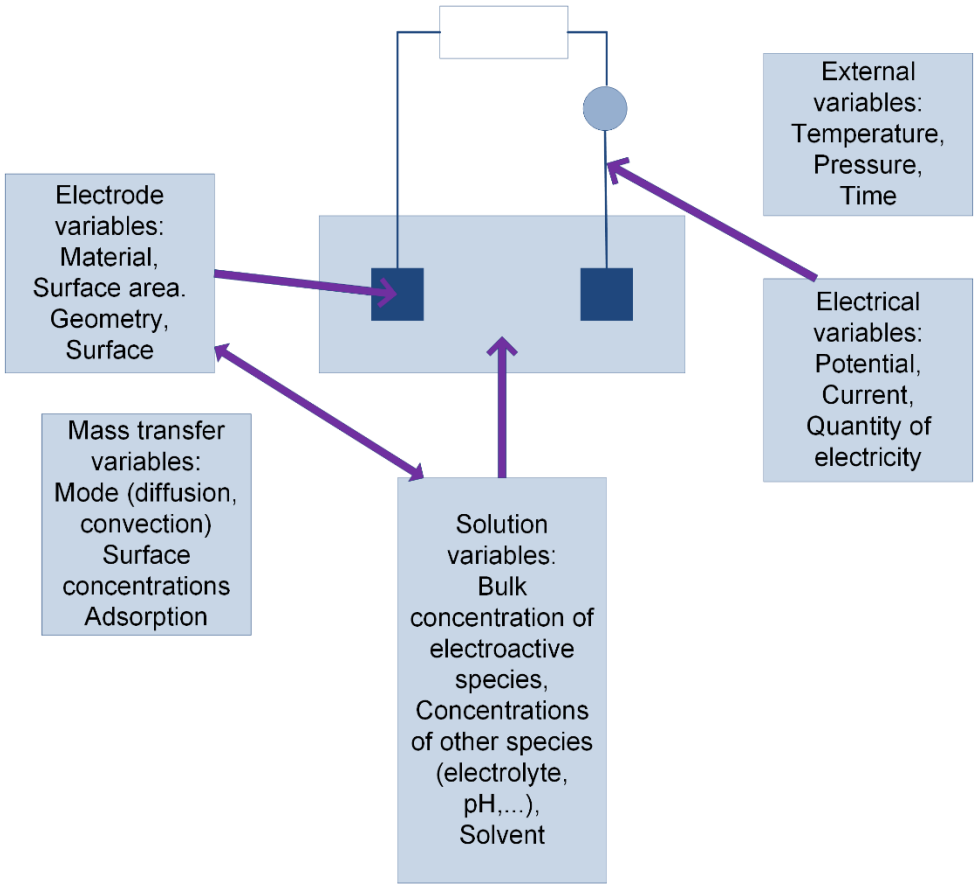

Figure 2.4. Synopsis of the variables in the electrochemical cell [57].

As it can be seen, the transport of species inside the electrolyte depends on the geometrical and the electrical characteristics of the material (electric field variations), on

the concentration and pH of the solution, on the electrical parameters such as potential, current, and type of the applied electricity (alternating (AC) or direct (DC)), on the growth temperature, and on the growth time as illustrated in Figure 2.4.

Therefore, to design the shape and conductivity type of the novel structures various variables can be applied in electrochemical cell to alter the ionic transport of chemical species.

2.2. Electrochemical Synthesis of ZnO Nanowires

Electrochemical growth of ZnO NWs can be performed in potentiostatic or galvanostatic modes in a three-electrode cell. The electrochemical cell comprises the auxiliary electrode (platinum wire gauze), the reference electrode (Ag/AgCl in saturated 4M KCl with potential drop +0.24 V vs. NHE (normal hydrogen electrode)), the working electrode (substrate, where ZnO NWs growth takes place), and the electrolyte. The electrolyte contains two equivalent concentrations of initial products, the source of zinc ions $Zn(NO_3)_2 \cdot 6H_2O$ (zinc nitrate hexahydrate) and the source of hydroxide ions $C_6H_{12}N_4$ (hexamethylenetetramine). The pH of the solution is between 6 to 7 which implies that there is no excess or deficiency of OH^- ions in electrolyte, and the solution is neutral. The major constituents for synthesis of ZnO NWs at 6-7 pH of electrolyte are zinc hydroxide (precipitates), nitrate, and zinc ammonia complexes. The governing reactions inside the electrochemical cell are [61, 62]

$$Zn^{2+} + 2OH^- \rightarrow Zn(OH)_2 \rightarrow ZnO + H_2O \tag{2.11a}$$

$$\begin{aligned} NO_3^- + H_2O + 2e^- &\rightarrow NO_2^- + 2OH^- \text{ at electrode and crystal surfaces} \\ NO_3^- + 6H_2O + 8e^- &\rightarrow NH_3 + 9OH^- \text{ at electrode and crystal surfaces} \end{aligned} \tag{2.11b}$$

$$Zn(NH_3)_4^{2+} + 2OH^- \rightarrow ZnO + 4NH_3 + H_2O \quad (2.11c)$$

In the bulk solution hexamine ($C_6H_{12}N_4$) contributes to the production of hydroxide ions (OH^-) and ammonia (NH_3), which react with Zn^{2+} ions. The product of these reactions are the precipitation of ($Zn(OH)_2$) and tetraammine zinc ($Zn(NH_3)_4^{2+}$) ions, which are the precursors to ZnO. $Zn(OH)_2$ is spontaneously dehydrated into ZnO and H_2O on the crystal surfaces at the applied temperatures usually more than 70°C as shown in Equation (2.11a). Ions of tetraammine zinc react with OH^- ions at the electrode surface and on the crystal surfaces as shown in Equation (2.11c).These reactions are governed by the diffusion mass transfer mode indicating that the above chemical reactions do not need the applied electric field. It is always occurs at high temperatures (>70°C). Another formed ions in solution that create ZnO are $Zn(OH)^+$. Furthermore, nitrate ions reduce to nitrite (NO_2^-) and hydroxide (OH^-) ions at electrode and crystal surfaces, when they accept electrons as demonstrated in Equation (2.11b). At higher amount of available electrons (higher applied electric field inside the electrochemical cell) nitrate ions produce ammonia and hydroxide ions and contribute to the increased density of the hydroxide ions in vicinity of the charged surface as illustrated in Equation (2.11b).

The investigation of the effect in the modification of the ionic current in electrochemical cell, in terms of the variations in the concentration of the electrolyte, in the growth temperature, and in the conductivity type of the substrate, on the geometric shape and distribution of ZnO NWs is disclosed subsequently, in Chapter 3.

3. Synthesis and Characterization of ZnO Nanowires

There are several techniques to synthesize ZnO nanowires including vapor phase [63 – 67] and wet chemical processes [8 – 13, 68 – 73]. Contrary to other techniques, wet chemical methods, like electrochemical and hydrothermal processes, are performed at low temperature, and have potential in large scale production. Furthermore, an electrochemical process has advantages such as potential to grow uniform and large area of nanowires, fast growth, and strong adhesion of NWs to the substrate, as well as much lower cost than the other techniques. In this work we have used this technique to grow ZnO NWs.

Here, the studies on growth of ZnO NWs emphasizing the effects of different growth parameters on NWs shape, size, and distribution are reported. The morphology and distribution of the ZnO NWs depend on the charge transfer kinetics based on the Buttler-Volmer equations of current (Equation (2.9)). Therefore, the effects of variations in the ionic flux by changing concentration of the electroactive species, the conductivity of the working electrode, and the growth temperature on the geometry of nanowires and their distribution were considered in this work. To characterize the fabricated nanowires, Field Emission-Scanning Electron Microscopy (FE-SEM) was used.

3.1. The Effect of the Electrolyte Concentration on ZnO NWs: Morphology and Distribution

Three different concentrations of constituents in electrolyte (6.3 mM (10^{-3}·Molar mass of chemical (g/L)), 5.4 mM, and 4.5 mM, at equal decrease of 0.9 mM, with equal concentrations of the zinc nitrate hexahydrate and hexamethylenetetramine diluted in deionized (DI) water) were used to study the effect of electrolyte concentration on morphology of ZnO NWs. The concentration amounts were chosen based on the previous researches [8 - 13, 17]. Indeed, it has been shown that high concentrations of chemicals in the electrolyte result in overgrowth and low concentrations lead to creation of a much dispersed distribution of nanostructures on the working electrode. A concentration of 6.3 mM of electrolyte was shown to generate ZnO NWs grown on the substrate with very uniform distribution. We further used 5.4 and 4.5 mM of electrolyte concentration to support the investigations on studying morphology of grown ZnO NWs. The electrolytes were stirred using magnet spinning for 15 minutes and heated to 80º C before electrochemical deposition. The growth time was chosen 30 minutes.

First, n-type (100) silicon ($\rho \approx$ 1-5 Ω·cm) was used as working substrate (electrode). One side of the working electrodes was always covered by Al using physical vapor deposition (PVD). Alloying at 450°C for 30 minutes was performed to create ohmic contact between Al and substrate (the purpose of the Al layer was to make sure that we have uniform distribution of charges on the silicon substrate). The applied voltage in the electrochemical cell was -1.5 V.

Image analyses of grown ZnO NWs on n-type Si in different concentrations of the electrolyte are demonstrated in Figure 3.1.

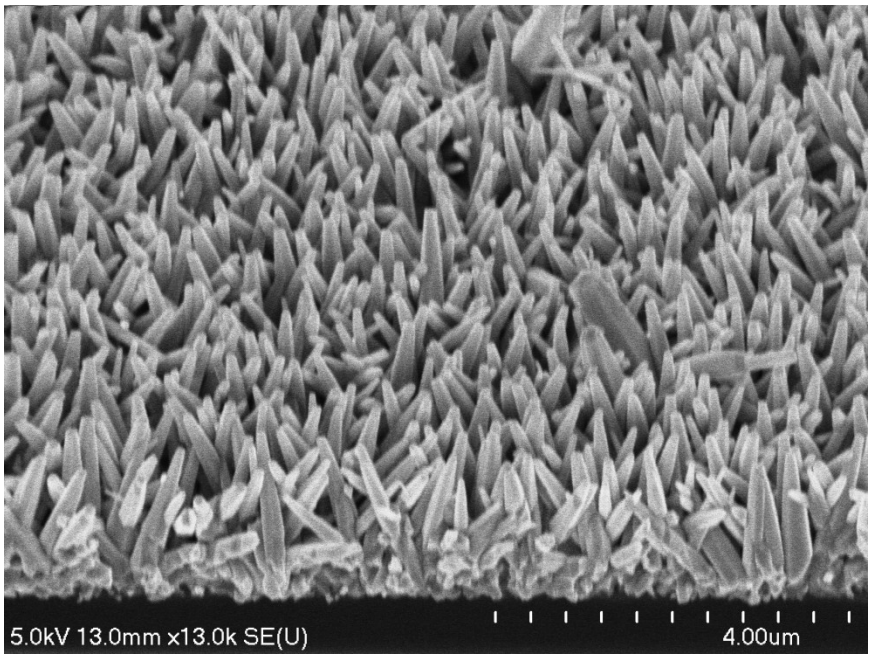

a)

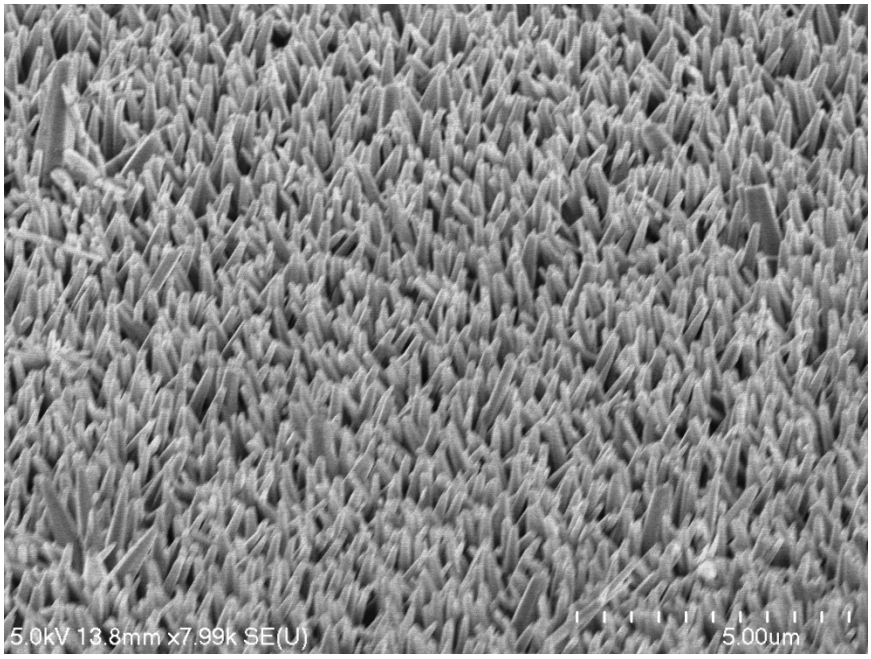

b)

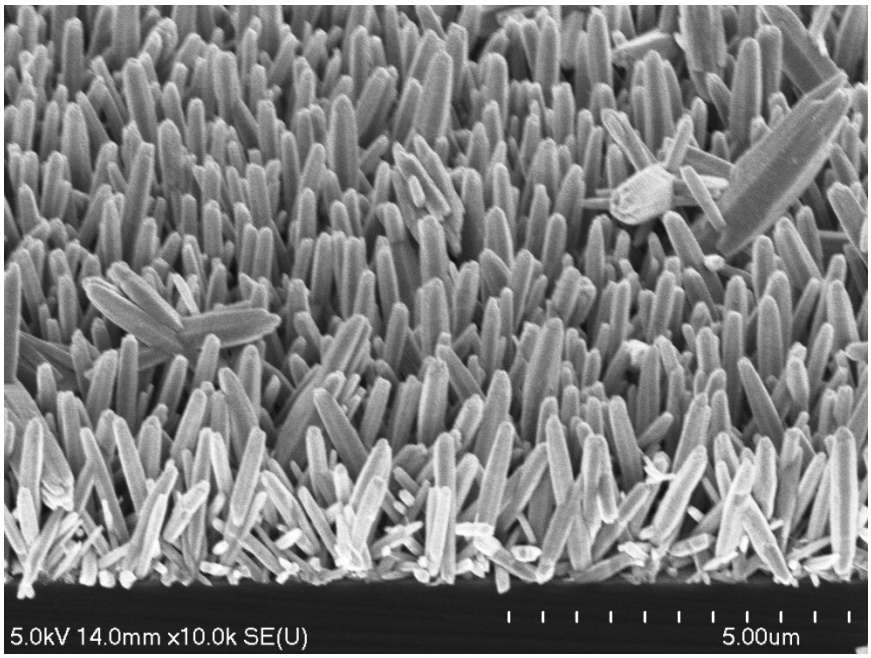

c)

Figure 3.1. SEM images of ZnO NWs electrochemically grown on n-type Si in electrolyte with equal concentrations of constituents: a) 6.3 mM, b) 5.4 mM, c) 4.5 mM.

The observations show the augmentation of ZnO NWs grown perpendicular to the surface as the concentration of the electrolyte decreases**.** ZnO NWs were grown on n-type substrate mostly making an angle smaller than 90° to the surface when the concentration of the electrolyte was 6.3 mM as demonstrated in Figure 3.1 (a). When concentration of the electrolyte was decreased to 5.4 mM, the angle between the majority of nanowires and the surface was increased, closer to a right angle as shown in Figure 3.1 (b). Further, at electrolyte concentration of 4.5 mM as Figure 3.1(c) illustrates, ZnO NWs mostly grown perpendicular to the working electrode.

Next, p-type (100) Si (resistivity = 7-30 Ω·cm, thickness = 525 μm) was used as the working electrode. Applied voltage in the electrochemical cell was -1.5 V.

Electrochemically grown ZnO NWs on p-type Si for various concentrations of electrolyte are shown in Figure 3.2.

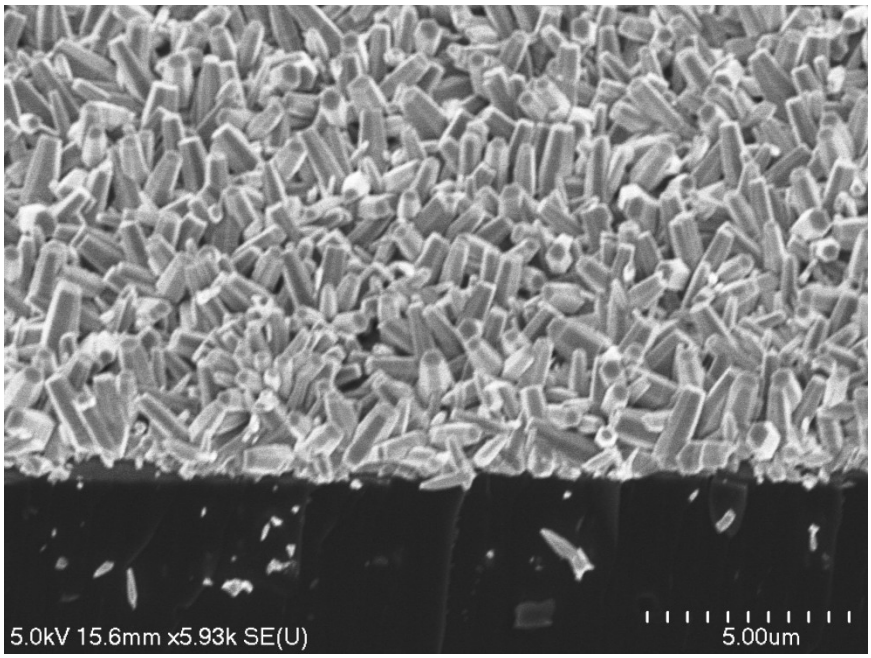

a)

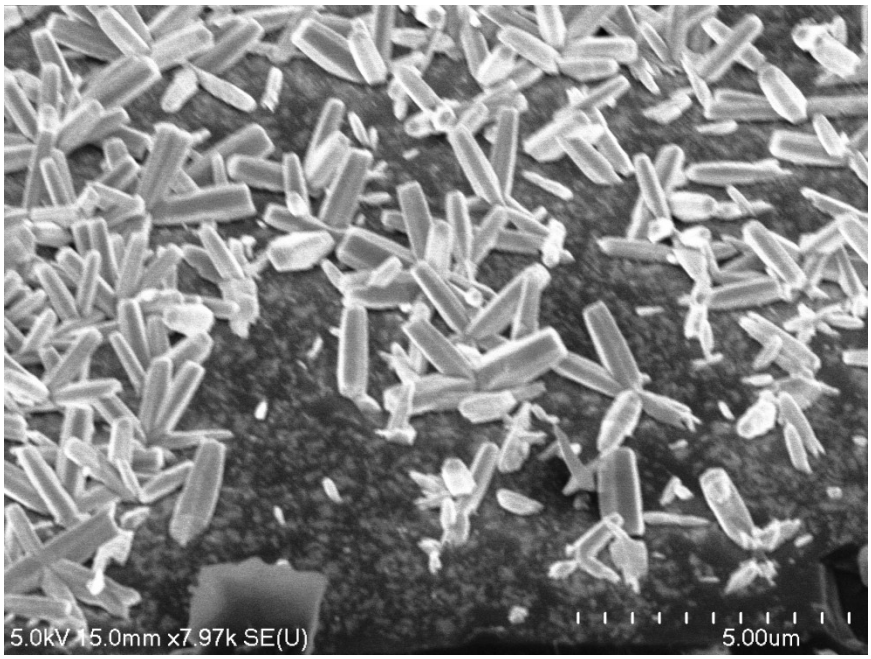

b)

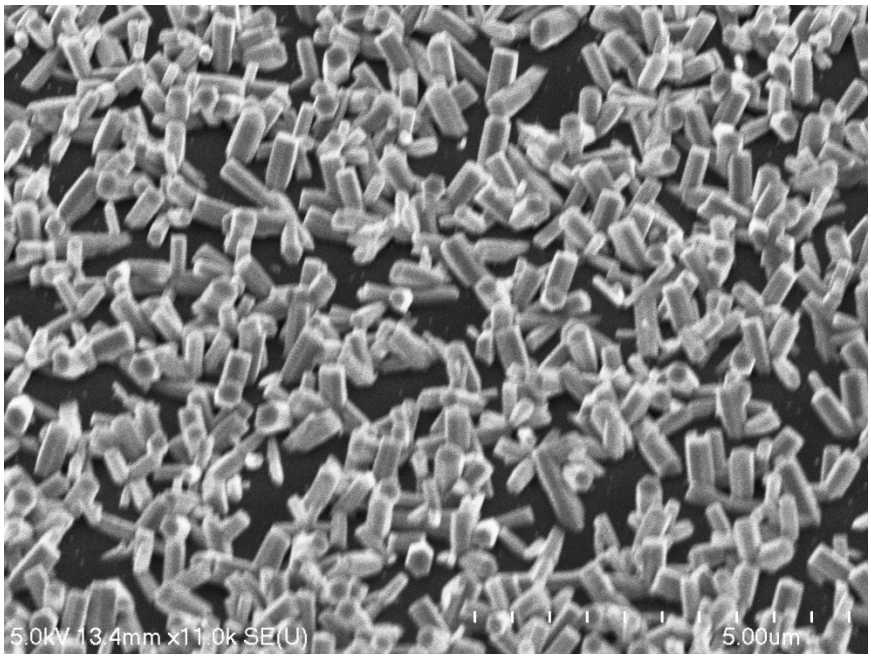

c)

Figure 3.2. SEM images of ZnO NWs electrochemically grown on p-type Si in electrolyte with equal concentrations of constituents a) 6.3 mM, b) 5.4 mM, c) 4.5 mM.

At high electrolyte concentration, dense hexagonal wurtzite nanowires with average length of about 2.5μm and with diameters of about 300 nm were grown on the substrate (l = 2.5 μm, d = 0.3 μm). The nanowires concentration as well as their length (around 2 μm), and the diameters (about 250 nm) were decreased, when the concentration of the electrolyte was reduced to 5.4 mM. The effect was more pronounced as the electrolyte was further diluted.

In the following studies, a working electrode of Ti/Au layer (50nm/100nm) sputtered on n-type Si was considered. Applied voltage in the electrochemical cell was -1.0 V. Electrochemically grown ZnO NWs on the Au layer are illustrated in Figure 3.3.

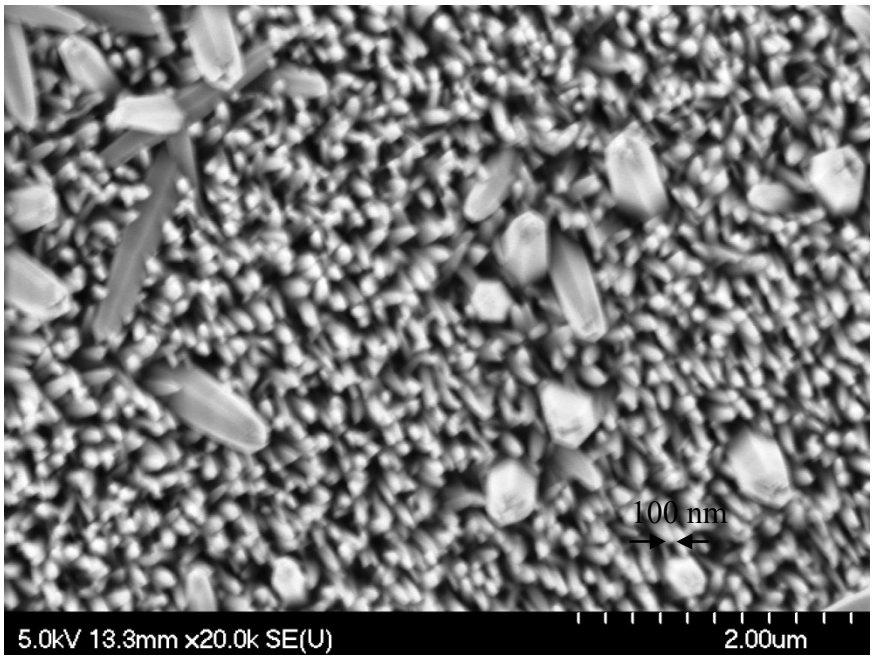
100 nm
5.0kV 13.3mm x20.0k SE(U)
2.00um

a)

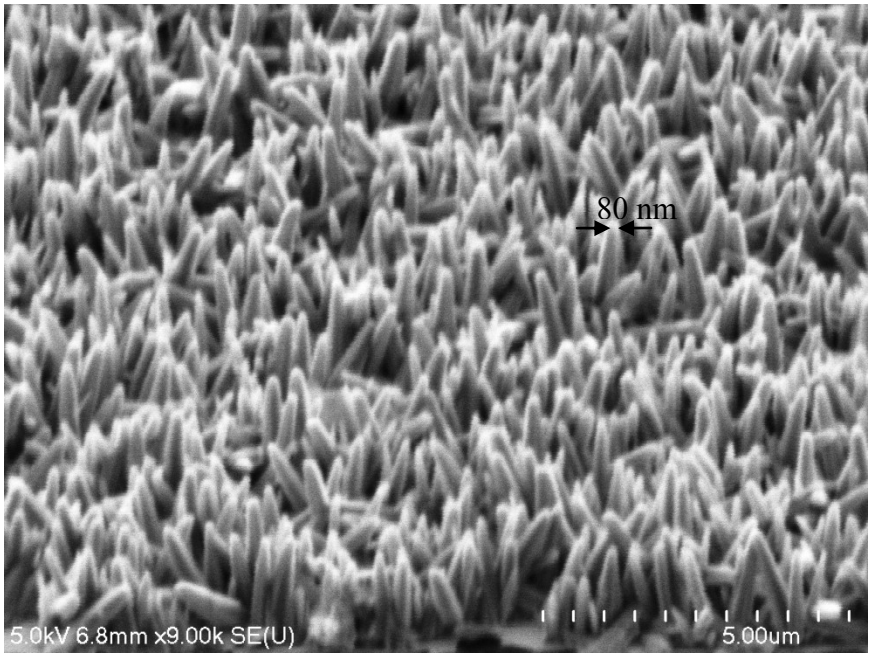
80 nm
5.0kV 6.8mm x9.00k SE(U)
5.00um

b)

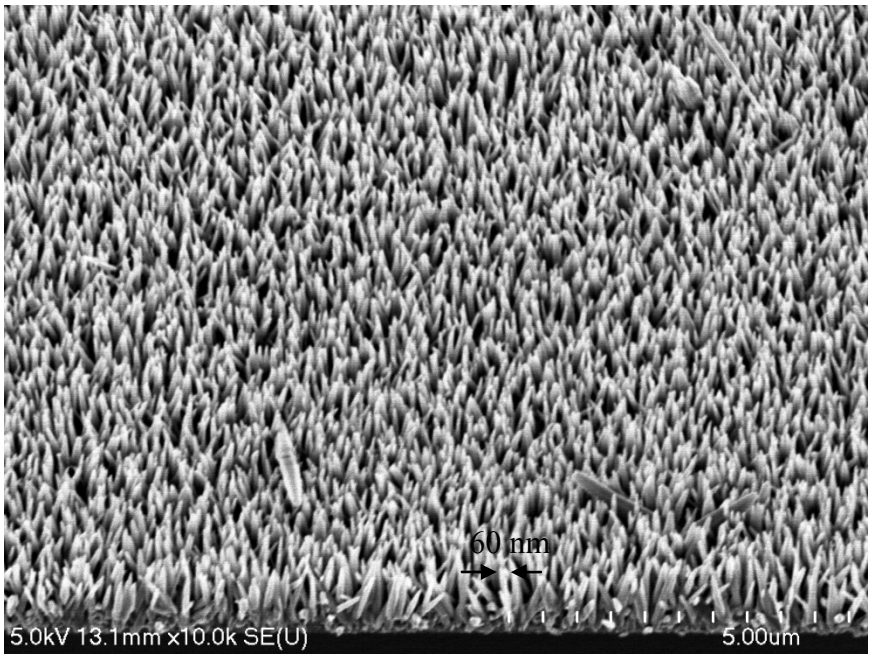

c)

Figure 3.3. SEM images of ZnO NWs electrochemically grown on Au/Ti layer in electrolyte with equal concentrations of constituents: a) 6.3 mM, b) 5.4 mM, c) 4.5 mM.

As the images show, at high concentrations of the constituents the grown nanowires had high density, with the tips around 100 nm. When concentration of electrolyte was decreased, the length of the nanowires and their diameters (around 80 nm) were decreased. For the further dilution of the electrolyte the nanowires tips became even sharper, with around 60 nm diameters.

Studies revealed that although the electrolyte concentration affects the size and geometrical structures of the grown nanowires, but it is their distribution that is most affected by this parameter. The reason is that the decrease in electrolyte concentration leads to:

- increased mobility of ions because of increased free mean path and diffusion coefficient;

- increased amount of hydroxide ions at the vicinity of the working electrode due to higher mobility ($20.6 \cdot 10^4$ $cm^2 s^{-1} V^{-1}$) compared to the mobility of zinc ions ($5.5 \cdot 10^4$ $cm^2 s^{-1} V^{-1}$) [60], causing to reduce amount of zinc ions at the vicinity of the nanowires base.

It is shown that the hydroxide ions (source of oxygen in ZnO NWs) are responsible for the directionality of ZnO NWs [36, 74 - 75]. Therefore, the increased amount of these ions leads to the improvement of the directionality and sharper nanowires tips.

3.2. The Effect of the Substrate Conductivity on ZnO NWs: Morphology and Distribution

To study the effect of the substrate on the grown nanowires structures, we have used four different working electrodes (substrates), a gold layer sputtered on an n-type Si wafer, two n-type (100) Si with two different resistivity ($\rho \approx 1$ - 5 $\Omega \cdot cm$ and $\rho \approx 10^{-3}$ $\Omega \cdot cm$), and a p-type Si (resistivity = 7 - 30 $\Omega \cdot cm$, thickness = 525 μm). Concentration of the electrolyte was kept constant at 5.4 mM. The growth temperature and time were 80° C and 45 minutes, respectively.

At any applied voltage inside the electrochemical cell, a rectifying contact will be formed between the working electrode and the electrolyte (a Schottky barrier between the metallic working electrode and the solution and a heterojunction between semiconductive electrode and the electrolyte).

We believe that the electrons on the surface of the substrate must be responsible for the nanowires structures grown on the substrate. To show this we have made a layer of gold film on a silicon substrate first, then in order to manipulate the concentration of

electrons on the surface we have done some post-treatments using annealing the gold layer at various temperatures and times. In the case of ZnO NWs grown on Au layer it was hypothetically assumed:

- that limited amount of electrons possessing equal energies is the reason of perpendicular growth of nanowires, decreased density of the nanowires and high curvature of the NWs' pinnacles;
- that nonuniform distribution of electrons (varying conductivity of Au layer) lead to creation of ZnO NWs on the areas of higher conductivity.

To test these hypotheses, electrochemical growth of ZnO NWs was performed on Au layer sputtered on n-type Si with various annealing parameters of Au layer. Parameters were chosen as 350°C for 20 minutes, 380°C for 40 minutes, and 380°C for 1 hour. Also, we have used a gold layer etched, briefly in diluted (1:100) HCl acid for 3 to 5 minutes. The applied voltage in electrochemical cell was -1.0 V. Grown ZnO NWs on the treated metallic surfaces are illustrated in Figure 3.4.

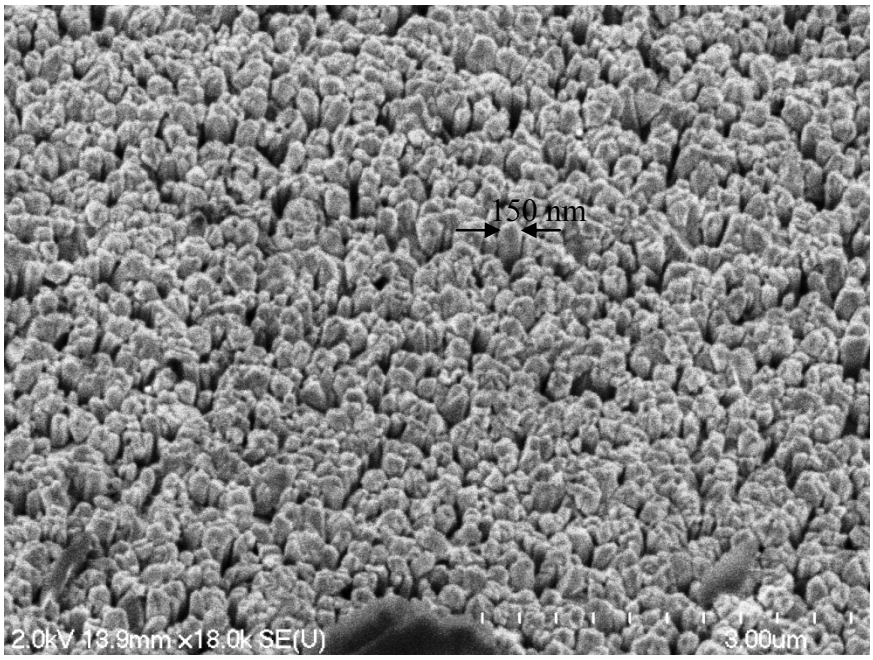
150 nm
2.0kV 13.9mm x18.0k SE(U)
3.00um

a)

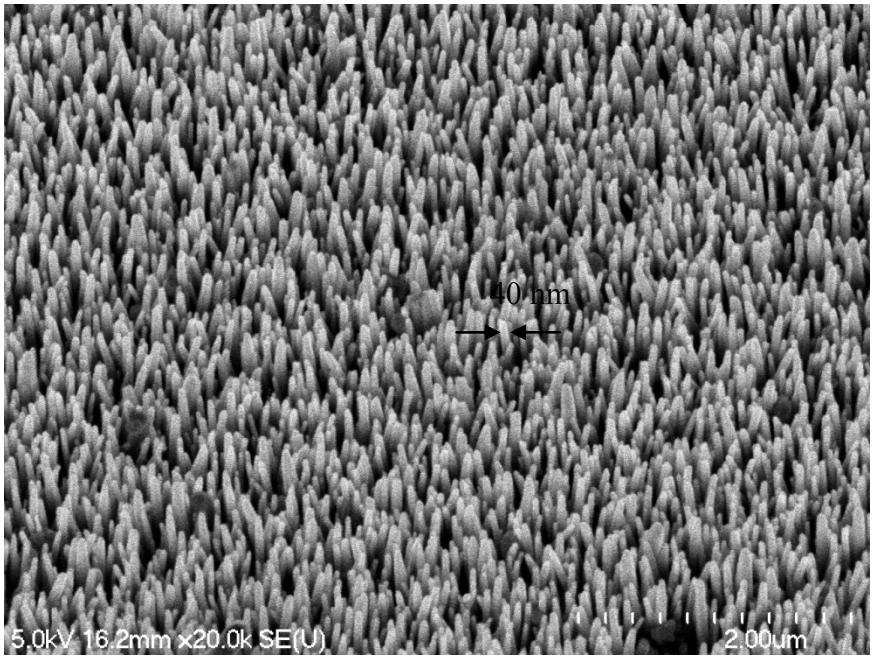
40 nm
5.0kV 16.2mm x20.0k SE(U)
2.00um

b)

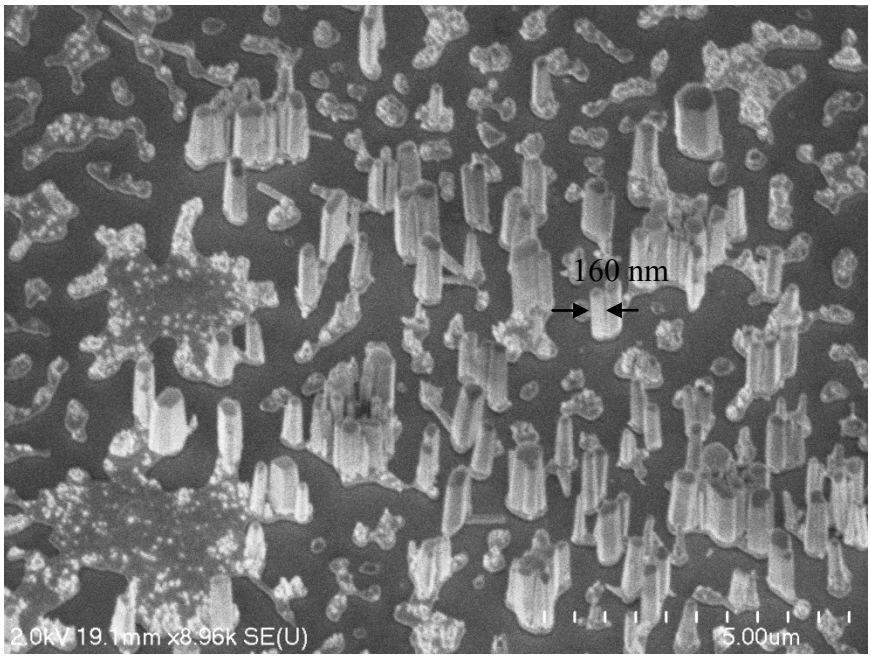

c)

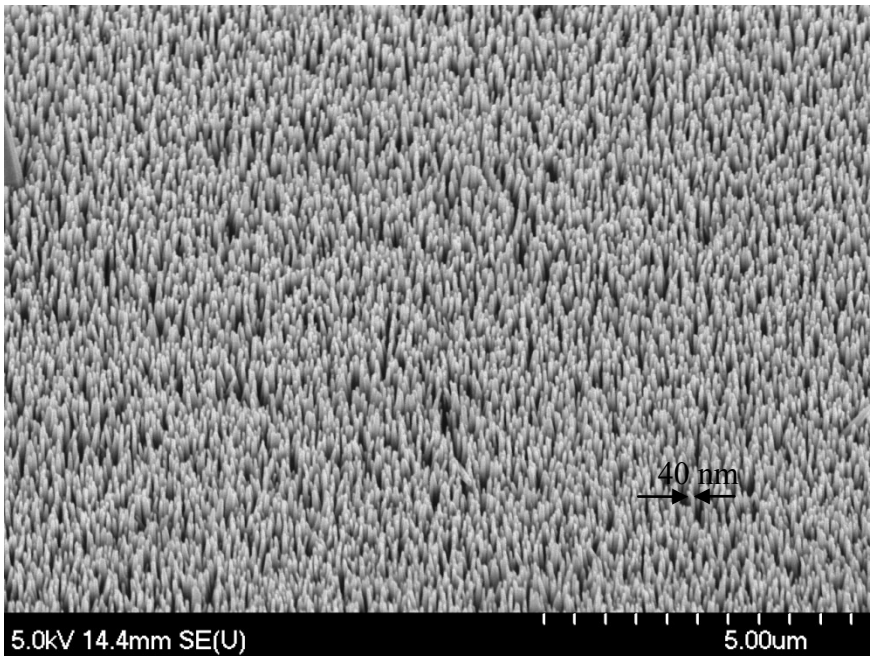

d)

Figure 3.4. SEM images of ZnO NWs electrochemically grown on Au layer in electrolyte concentration of 5.4 mM, where Au layer was annealed a) at 350° C for 20 min., b) at 380° C for 40 min., c) at 380° C for 1 hour, and d) ZnO NWs grown on a Au layer briefly etched in HCl.

The results show that as we have altered the thickness of the gold on the silicon substrate the structure and the concentration of the grown nanowires are changed. For example, for annealing the layer at 350° C (a temperature less than the eutectic temperature of the gold, 363° C), short ZnO NWs with large diameters were grown on the substrate as illustrated in Figure 3.4 (a). Formation of the thin and long ZnO NWs with high curvature of the tips and low density was achieved, when annealing temperature was at 380° C, larger than the eutectic temperature of the gold (this causes the creation of uneven surface and thickness of the gold layers). Nanowires grown under this condition had lower density with varying diameters. The variations are dependent on the conductivity of the particular place on the substrate where the NWs grew. In other words, the changes were dependent on the thickness of the gold layer. Further, by increasing the annealing time some nano islands were created on the film. As the Figure 3.4 (c) shows, nanowires were grown on metallic areas. Finally, when the conductivity of the surface was altered by brief etching of the metallic layer in HCl acid, ZnO NWs were grown with smaller diameters and high curvatures of the apexes.

In the case of semiconductor substrates used as the working electrodes, the electrons on the semiconductive surface have varying energies due to the presence of the charge space region and because of the energy band bending at an applied voltage inside electrochemical cell. Hypothetically, we can anticipate:

- that uniform distribution of electrons with varying energies on the surface of the semiconductive electrode causes nonuniform distribution of zinc and hydroxide ions and leads to formation of the nanowires with angle less than 90° with respect to the surface;

- that the increased amount of electrons on the surface of the semiconductive electrode causes generation of high quantity of Zn ions at the vicinity of the substrate surface and makes them less available on the NWs crystalline surfaces. This leads to grow nanowires with large base diameters, and sharp curvature at the tips of NWs.

The electrochemical growth of ZnO NWs was performed on semiconductive working electrode with various conductivities. The applied voltages were -1.5 V in the case of n-type and p-type Si, and -1.0 V when phosphorous doped n^+-type Si was used as working electrode. The SEM observations of the grown ZnO NWs on silicon substrates illustrate that as the conductivity of the n-type Si increases well-defined and uniform nanoprotrusions on the NWs pinnacles with very sharp tips are grown on the substrate as illustrated in Figure 3.5.

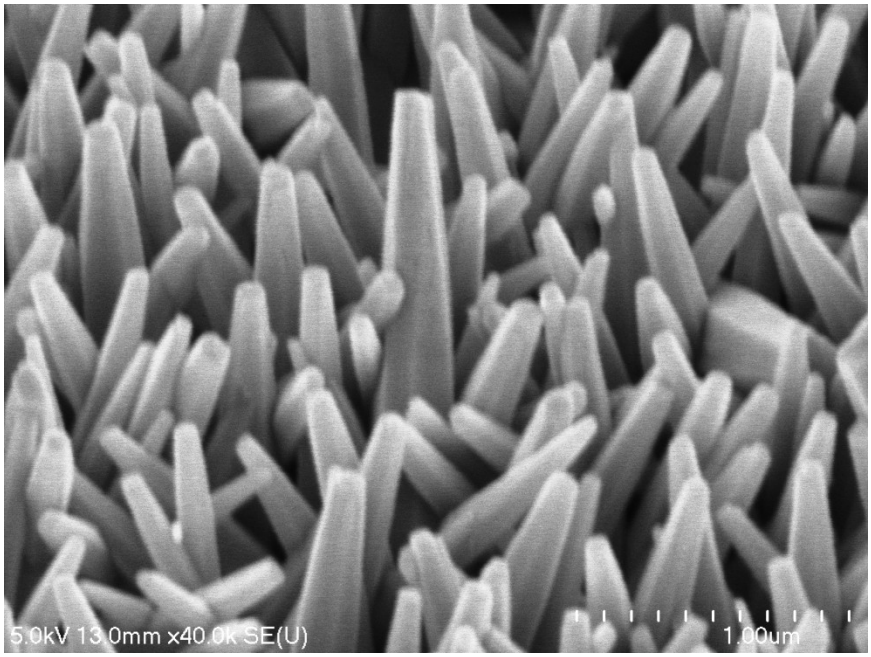

a)

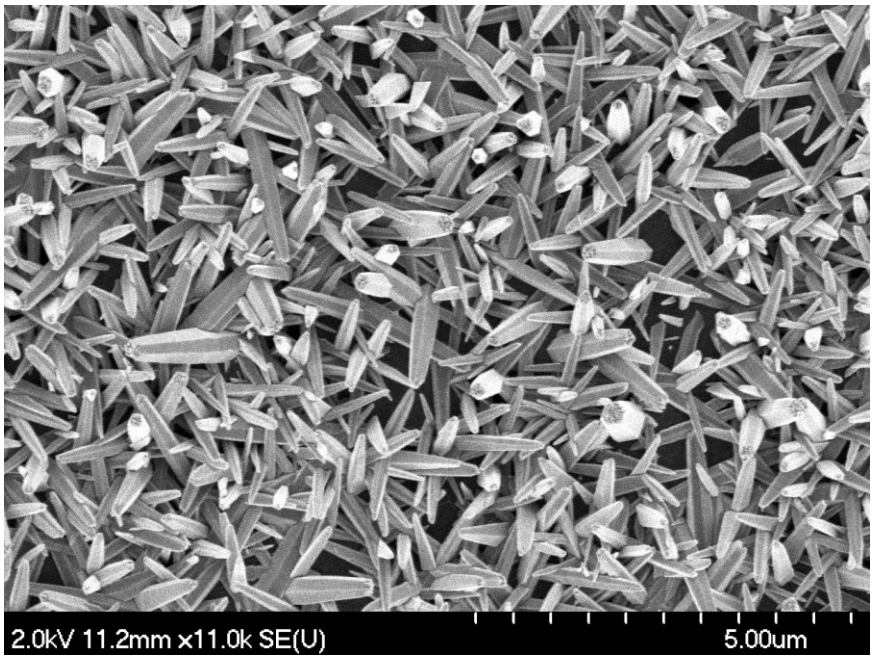

b)

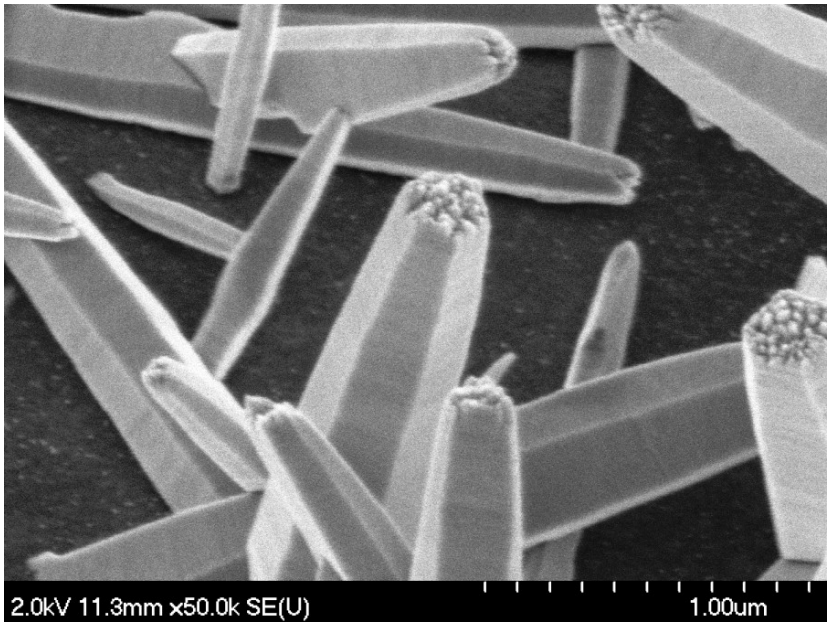

c)

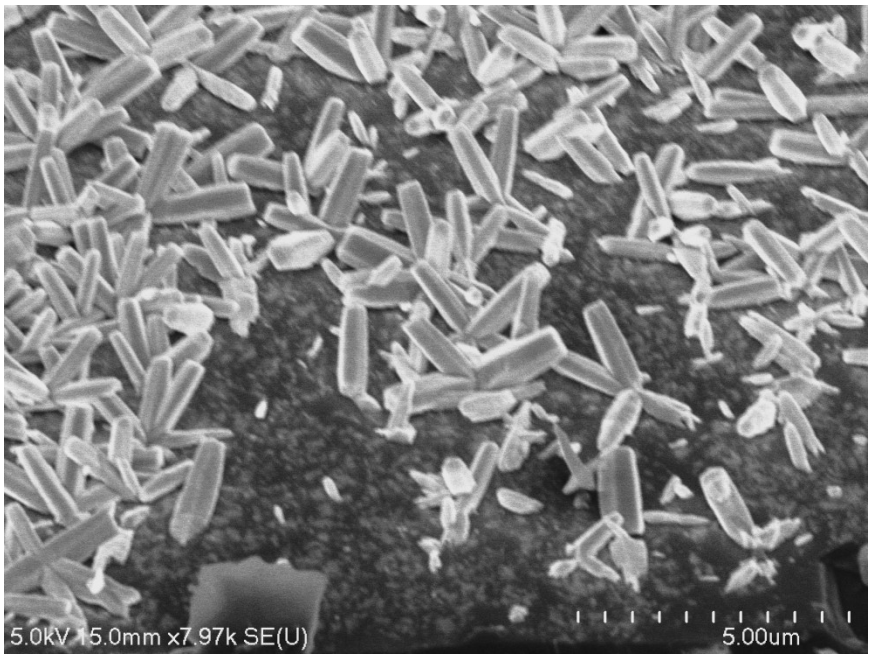

d)

Figure 3.5. SEM images of ZnO NWs electrochemically grown on a) n-type Si, b) doped n-type Si, c) doped n-type Si showing 2D nucleation and growth on the (0001) face, and d) on p-type Si.

ZnO NWs in all cases were grown at some angle to the substrate as illustrated in Figure 3.5. Low conductivity n-type Si resulted in formation of the nanostructures with almost flat tips. In the case of low resistivity n-type Si, nanoprotrusions were observed on the NWs pinnacles. P-type Si resulted in creation of the nanostructures with flat tips; the crystalline nanowires had very uniform structures with a diameter of about 300 nm.

The above investigations reveal that the morphology and distribution of ZnO NWs are strongly dependent on the conductivity of the substrate, which could be due to the concentrations and distribution of the electrons available on the surface of the substrates.

3.3. The Effect of Temperature of the Electrolyte on ZnO NWs: Morphology and Distribution

Temperature of the electrolyte plays an important role in the formation of the ionic current inside the electrochemical cell (please see Equation (2.6)). In these studies we have investigated the effect of electrolyte temperature on the structures of the grown nanowires. While we have taken all other parameters constant, we have studied this effect on the working electrodes of n-type Si, n^+-type Si, and Au layer. Image analyses of the grown ZnO NWs on semiconductive surfaces at electrolyte temperatures of 80° C and 85° C are shown in Figure 3.6.

a)

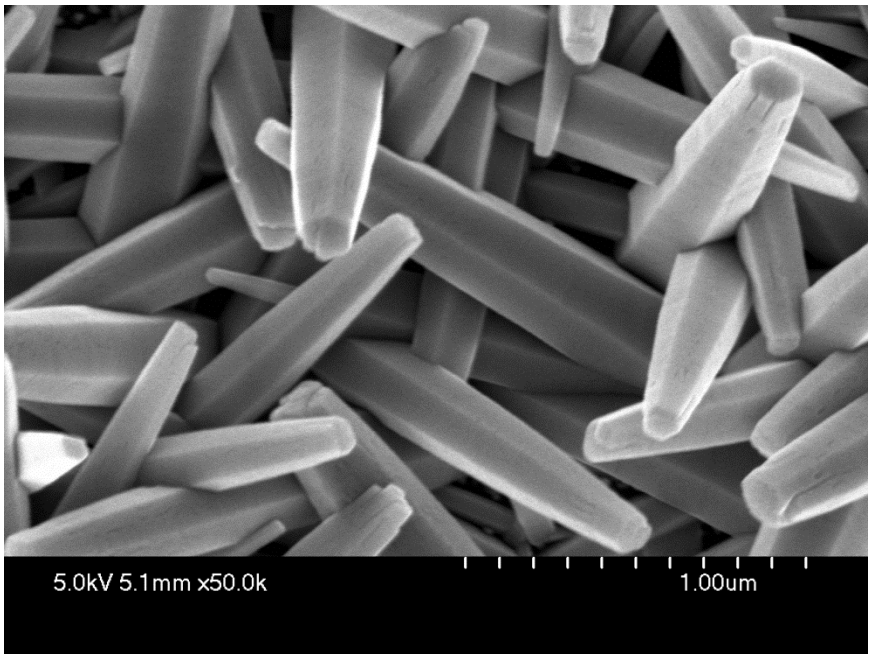

b)

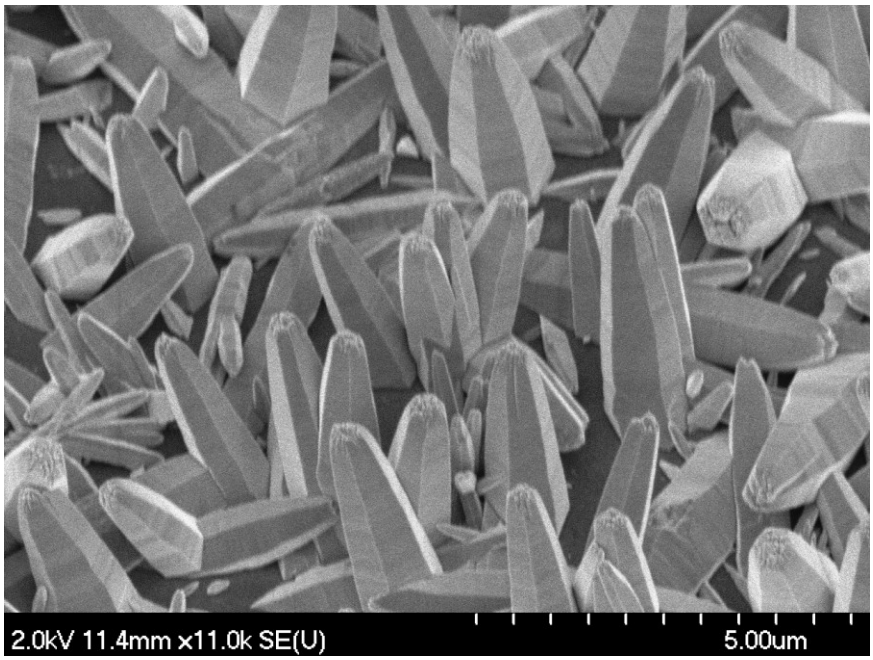

c)

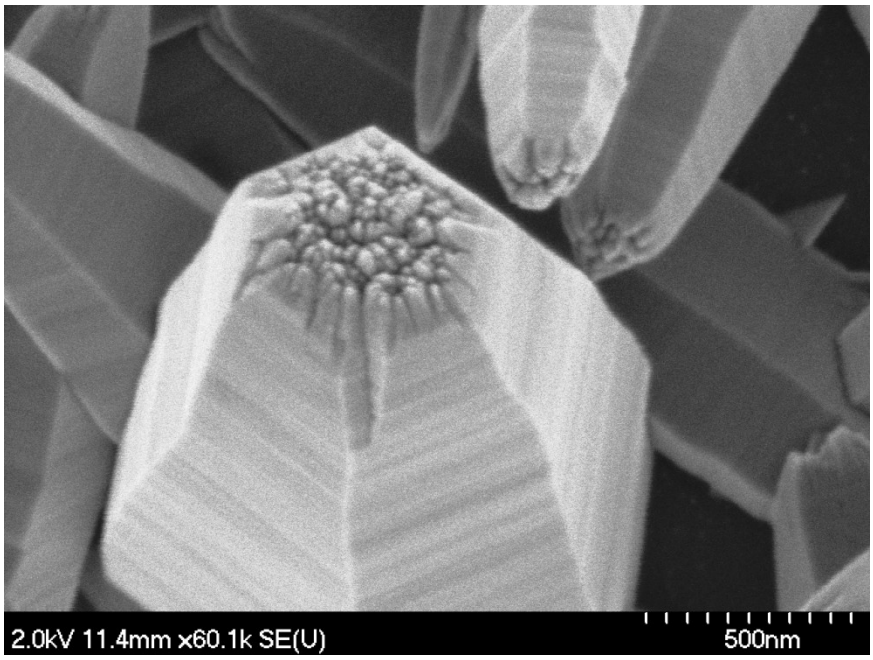

d)

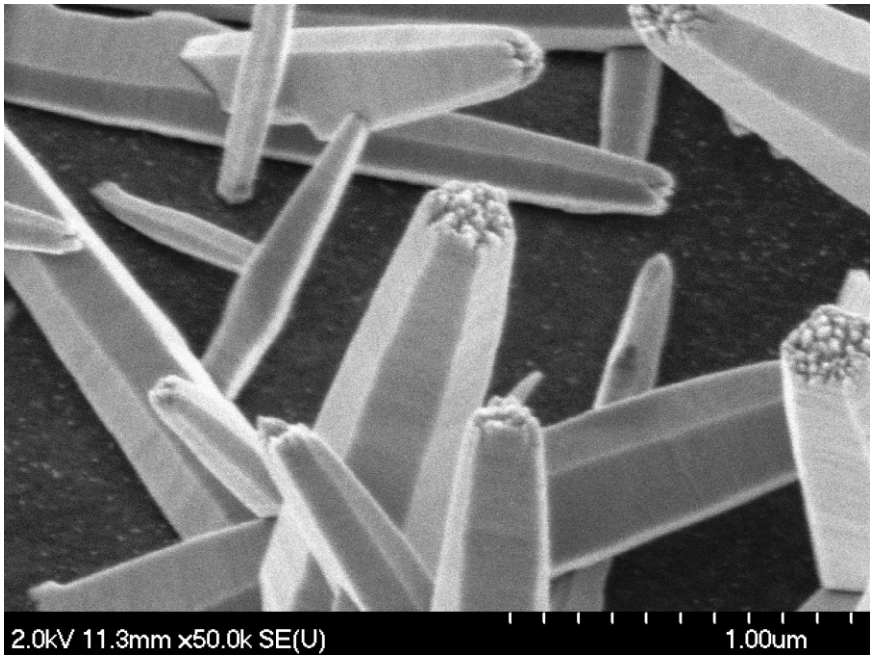

e)

Figure 3.6. SEM images of ZnO NWs grown at electrolyte temperature of a) 85° C on n-type Si, b) 80° C on n-type Si, c) 85° C on doped n-type Si, and (d - e) 80° C on doped n-type Si.

The morphology of ZnO NWs grown on n-type Si at temperature 85°C has shown well defined crystalline surfaces of hexagonal nanostructures. As the growth temperature

decreased by 5° C the diameter of the NWs apexes was decreased with respect to the previous case. Also, an uneven surface on the NWs pinnacles was observed which could be due to the smaller amount of zinc ions at the vicinity of the NWs tips as demonstrated in Figure 3.6 (b). Increasing conductivity of the substrate did not have any significant effects on the grown nanostructures.

Figure 3.7 shows the results of growing nanowires on Au layer.

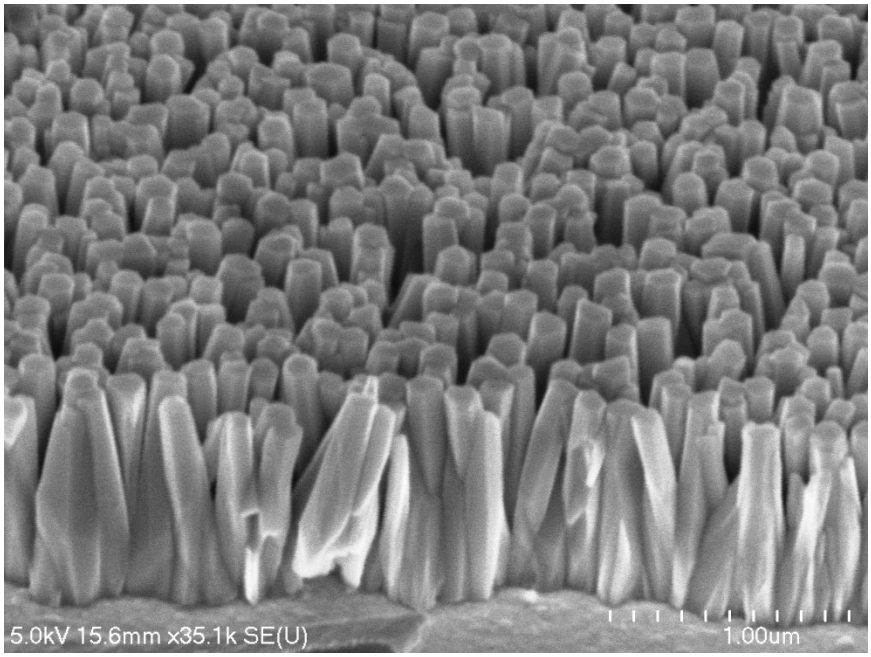

a)

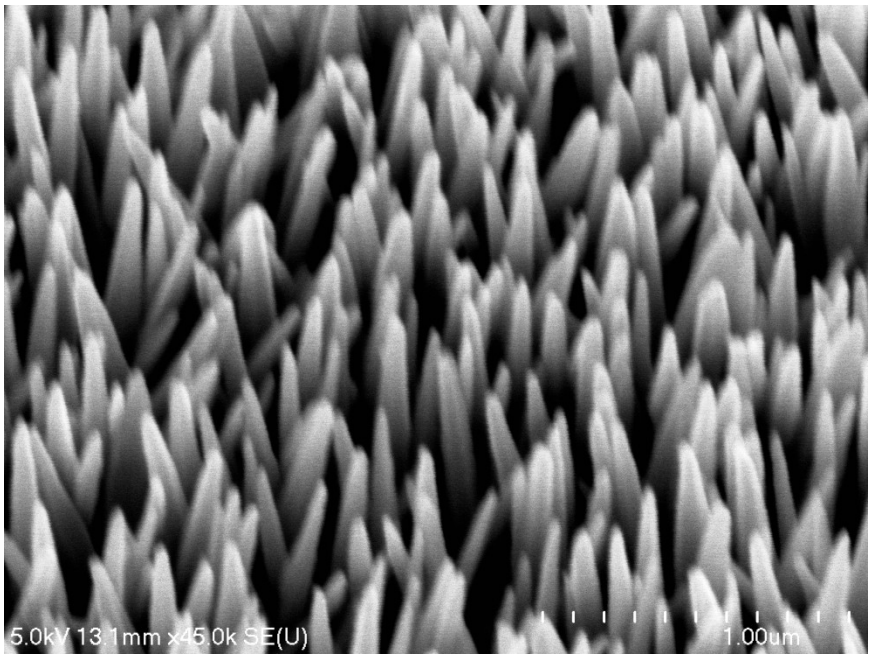

b)

Figure 3.7. SEM images of ZnO NWs grown on Au layer in the electrolyte at growth temperature of a) 85° C and b) 80° C.

Highly oriented and uniformly distributed arrays of ZnO NWs were obtained under both conditions. As the temperature changed the geometry and the diameter of the nanowires changed. At higher temperature the NWs diameters were increased and the tips were flatter. As temperature decreased low concentration of NWs with smaller diameters were generated.

Investigations on the effect of temperature on the morphology of ZnO NWs and their distribution showed that increased temperature resulted in improved crystallinity of the nanowires, increased diameters of NWs and uniform distribution. Indeed, temperature plays an important role in the formation of the ionic current inside electrochemical cell (Equation (2.6)). As temperature increased the flux of ZnO ions was increased what resulted in the increased diameters and uniform distribution of nanowires. Also, with the

temperature increase amount of the hydrogen impurities resided inside nanostructures reduced and caused in the improved crystalline structure of the nanowires.

4. Doping of ZnO Nanowires

ZnO NWs have found their ways in many applications: sensors, photonics and optoelectronic devices. Controlling the doping level and the conductivity of the nanowires plays an important role in many applications.

It is shown that ZnO NWs can be doped with impurities to produce p-type or n-type conductivity. P-type ZnO nanowires exhibit a band gap reduction and strong acceptor related photoluminescence, while n-type nanowires have band gap broadening with a strong donor-bound exciton emission. Although, the doping of ZnO NWs has been explored by several researchers [14-17, 76-80], but the technique to control the doping in the ZnO nanowires has been not reported in the past.

In this Chapter, we report studies on changes in the conductivity and doping concentrations of ZnO NWs during their growth. To achieve doped ZnO NWs, cationic doping in one step during electrochemical growth was used. In this process, Ag ions (group I) were used to produce p-type and Al ions (group III) to fabricate highly doped n-type ZnO NWs. Field Emission Scanning Electron Microscopy (FE-SEM), Energy-Dispersive X-ray Spectroscopy (EDXS), and photoelectrochemical cell (PEC cell) measurements were used to characterize the geometry, distribution, chemical constituents and conductivity type of our samples.

4.1. Doping of ZnO NWs with Ag and Al Impurities

Doping of ZnO NWs alters electrical, magnetic, and optical properties of the nanostructures. ZnO NWs are usually n-type semiconductor because of the intrinsic

defects such as hydrogen impurities. Cationic doping of ZnO NWs (impurities substitute Zn atoms in crystal) with low impurity concentration in the electrolyte is a diffusion-limited process, indicating that formation of nanowires starts at temperatures 70° C and above without applying an electric field. At limited diffusion process the reaction rate (which is the rate of NWs production) equals to the kinetic rate of the species in the electrolyte. The appropriate reduction voltage generates fluxes of the ions (zinc and impurities) moving toward the charged working electrode, where impurity ions reduce on the charged surface and partially replace zinc ions in the crystalline structures of the growing nanowires. Cationic doping is governed by diffusion mass transfer mode of ionic flux (ionic current mostly generated by diffusion). Thus, effective doping is achieved on the semiconductive or metallic substrates, when limited amount of the electrons provide necessary reduction energies (the produced ionic flux mostly generated by the diffusion mass transfer mode). High applied voltages or highly conductive working electrodes lead to drastic decrease of the effective doping, because the generated ionic current governed by migration transfer mode (where ionic flux is mostly generated by applied electric field).

Here we have investigated the effect of impurities (Ag or Al) introduced into the electrolyte on the nanowires conductivities. We have used again various substrates to grow the crystals, so the effects of conductivity of the substrates on the final products are also considered. The growth temperature in all cases was considered 80° C in electrochemical cell. Silver nitrate and aluminum nitrate nanohydrate were used to dope the nanowires. Table 4.1 shows the percentage mass of impurities that were added to the electrolyte to replace Zn ions.

Table 4.1. Concentrations of the chemicals used in the electrochemical cell for p-type and n-type doping of ZnO NWs.

Mass of Zn^{2+} replaced by mass of impurities [%]		Concentration is 5.4 mM		
		$AgNO_3$ [mg/L]	$Al(NO_3)_3 \cdot 9H_2O$ [mg/L]	$ZnO(NO_3)_2 \cdot 6H_2O$ [g/L]
Ag^+	0.3	1.669		1.602
	0.5	2.8		1.598
	0.6	3.3		1.5967
	0.8	4.45		1.5935
	1.0	5.562		1.59
	1.2	6.672		1.587
	1.5	8.316		1.582
Al^{3+}	1.5		42	1.582
	2.0		56	1.574
	2.5		70	1.566

In the case of Ag dopant, we have used an applied voltage of -0.8V. As the reduction voltage (when working electrode provides electrons with the energy comparable to the ionic valence electron orbital's energy, the ions accept electrons and solidify) for silver is +0.8 V and for zinc is -0.76 V, the applied voltage was large for the silver reduction but just enough for zinc reduction. The working electrode with more negative potential than required thermodynamics of the reaction generates increased ionic flux, which depends on the amount of the overpotential (η) (difference between the applied voltage and ionic reduction potential), and increases concentration of the ions on the charged surface. The generated ionic current density described by the Buttler-Volmer Equation (please see Equation (2.9)) at low overpotential is simplified to $j = j_0 \frac{nF\eta}{RT}$ (in the case of Zn

reduction) and at high overpotential, is expressed by the Tafel equation (in the case of Ag reduction) [57, 60]. The Tafel equation is given as $\eta=a+b\cdot\log(j)$, where $a=\frac{RT}{\alpha F}\ln j_0$ and $b=\frac{-a}{\ln(j_0)}$, R is ideal gas constant, T is the absolute temperature, α is the charge transfer coefficient with value between 0 and 1, F is Faraday constant, j is the current density, and j_0 is the exchange current density at equal reaction rates on anode and cathode at the condition that reversed reaction rate is negligible compared to the forward reaction [57, 60].

Electrochemically grown Ag-doped ZnO NWs on an n-type Si wafer are shown in Figure 4.1.

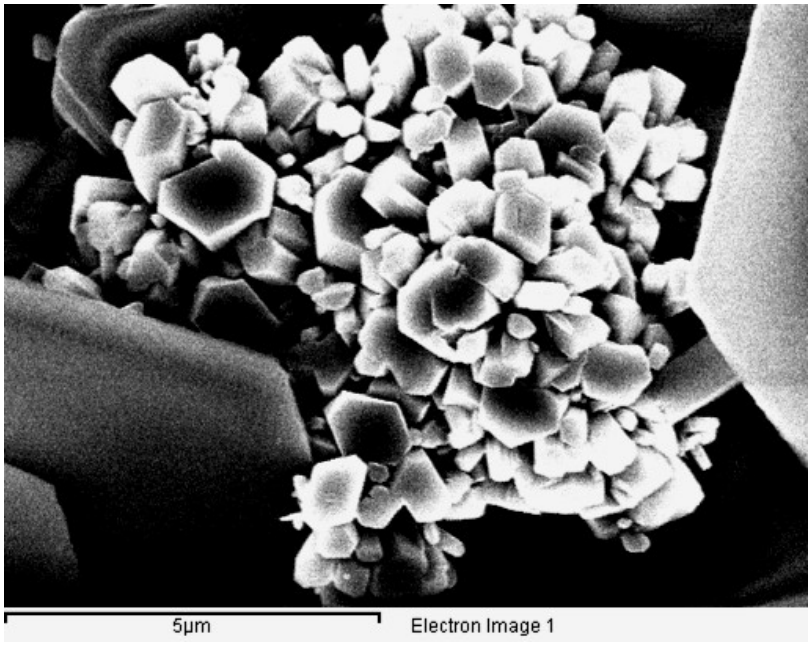

a)

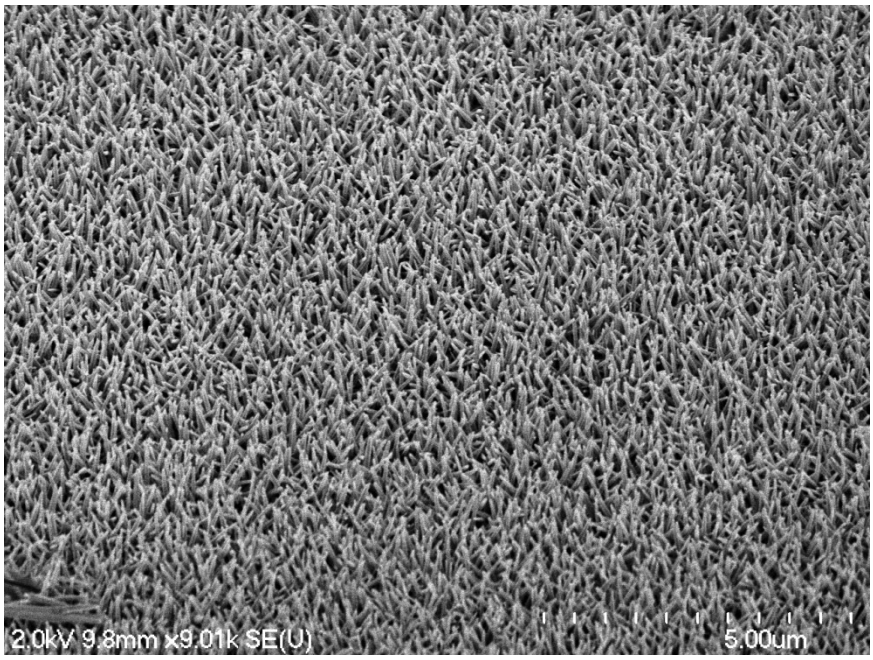

b)

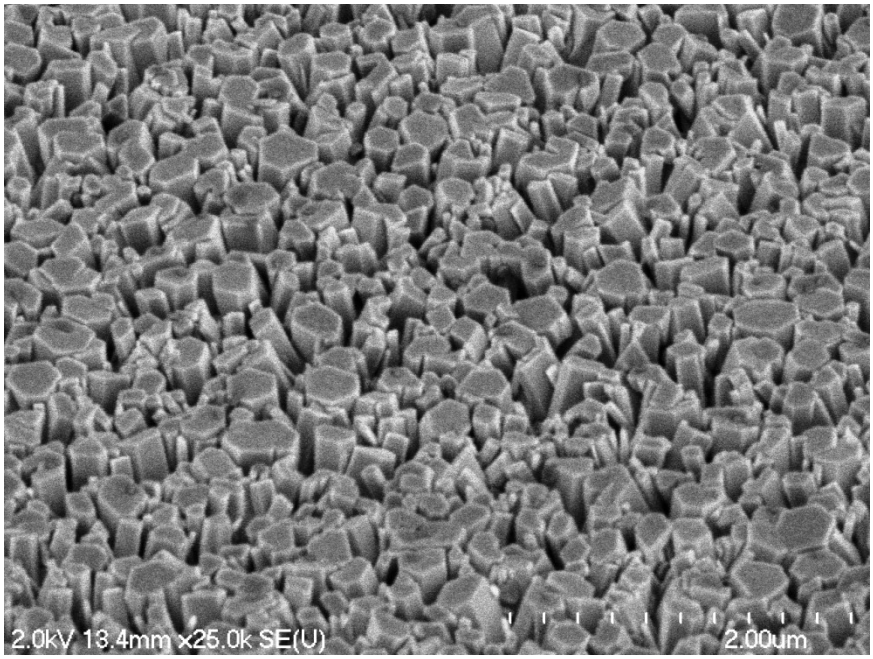

c)

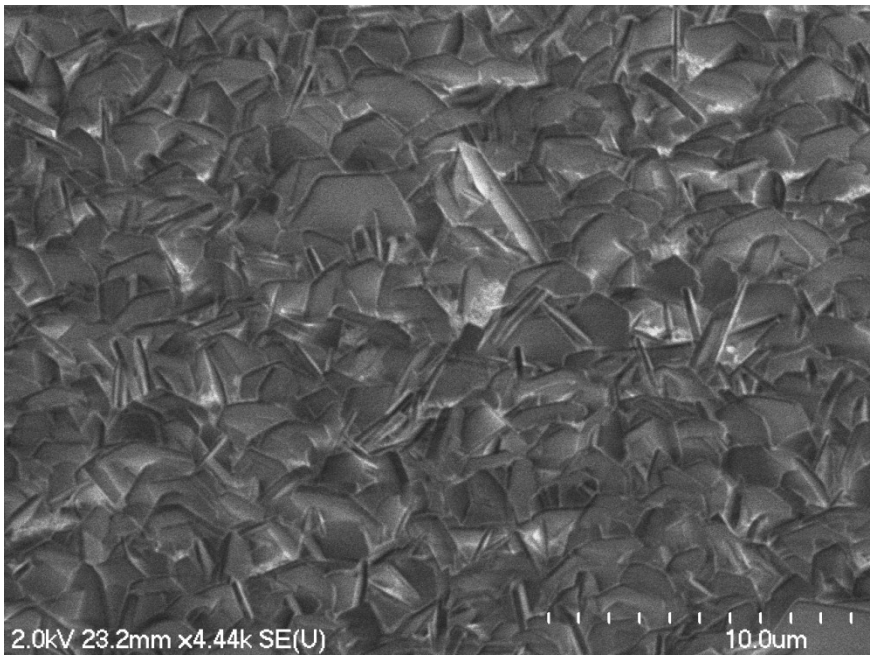

d)

Figure 4.1. SEM images of Ag-doped ZnO NWs grown on n-type Si in different concentrations of Ag: a) 0.5% of Zn mass replaced by Ag, b) 0.8% of Zn mass replaced by Ag, c) 1.2% of Zn mass replaced by Ag, d) 1.5% of Zn mass replaced by Ag.

When a small amount of silver is added to the electrolyte, hexagonal discs are formed on the substrate, causing growth of deformed nanowires on the substrates. An image of ZnO NWs on the n-type Si, where 0.8% of zinc ions were replaced by silver ions, illustrates long and very thin structures grown with uniform concentration. Further increase of the Ag amount inside the electrolyte has resulted in a closely packed distribution of ZnO NWs with various diameters. When the amount of silver was increased further, the nonuniform metallic layer was observed. As it can be seen the different amount of impurities inside electrolyte changes the morphology and distribution of nanowires. In addition, we observed that high concentration of Ag (more than 1%) disturbs the formation of the wurtzite hexagonal structure of the nanowires; possibly, because it is the Ag-O structure grown on the substrate which has a different crystal structure (it has cubic crystal structure). Based on SEM observations Ag-doped ZnO NWs with well-defined

morphology and uniform distribution are grown on n-type silicon when we had 0.8% of Zn mass replaced by Ag. Thereafter, we decided to use this proportion to check the doping of the nanowires with silver on n^+-type Si as well as on a layer of gold film. The results of these studies are shown in Figure 4.2.

a)

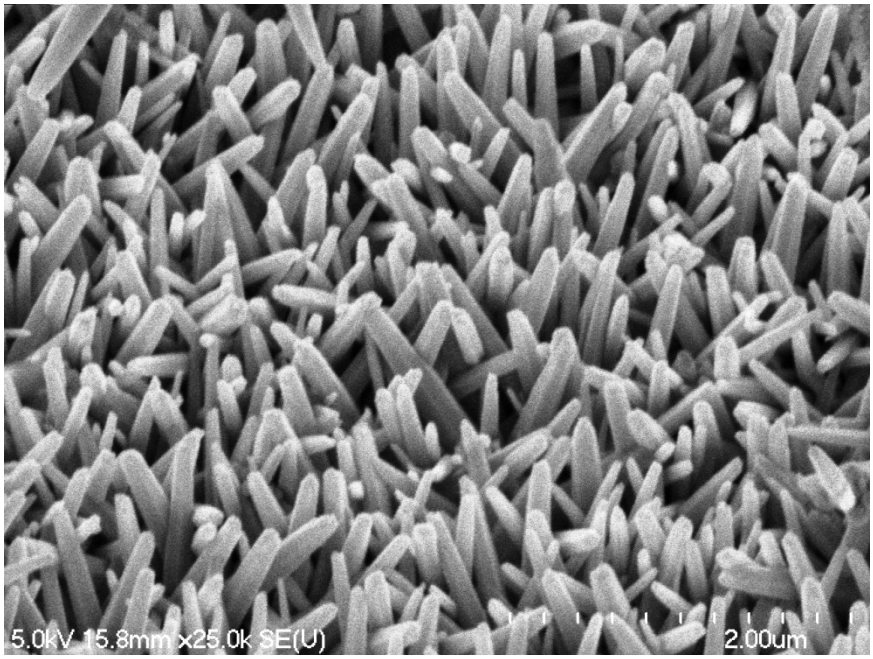

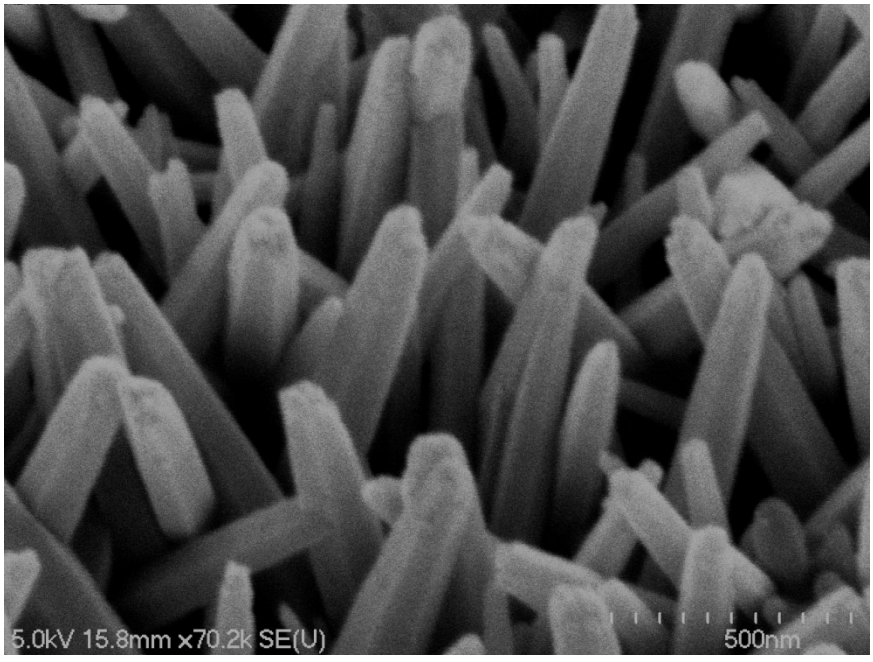

b)

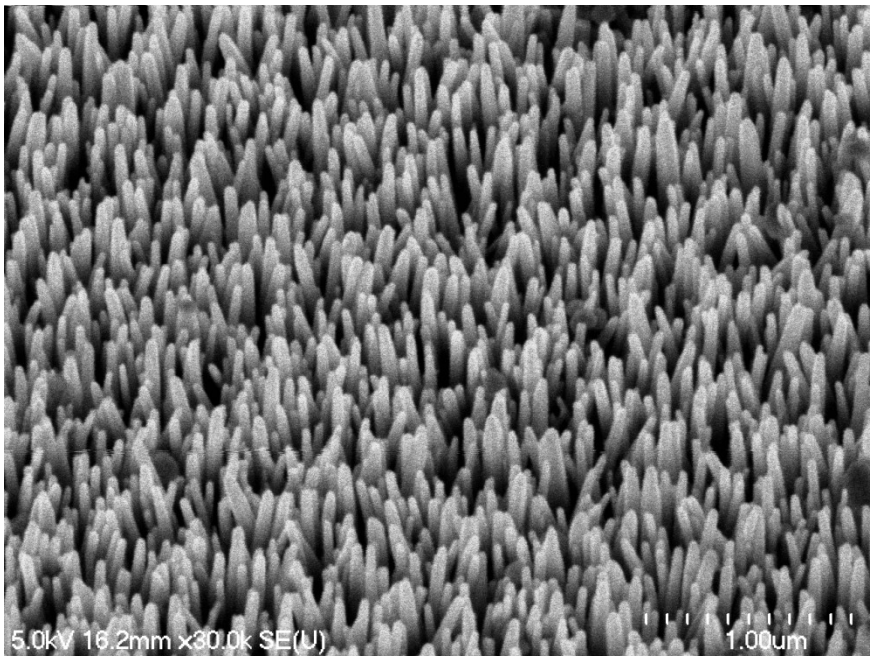

c)

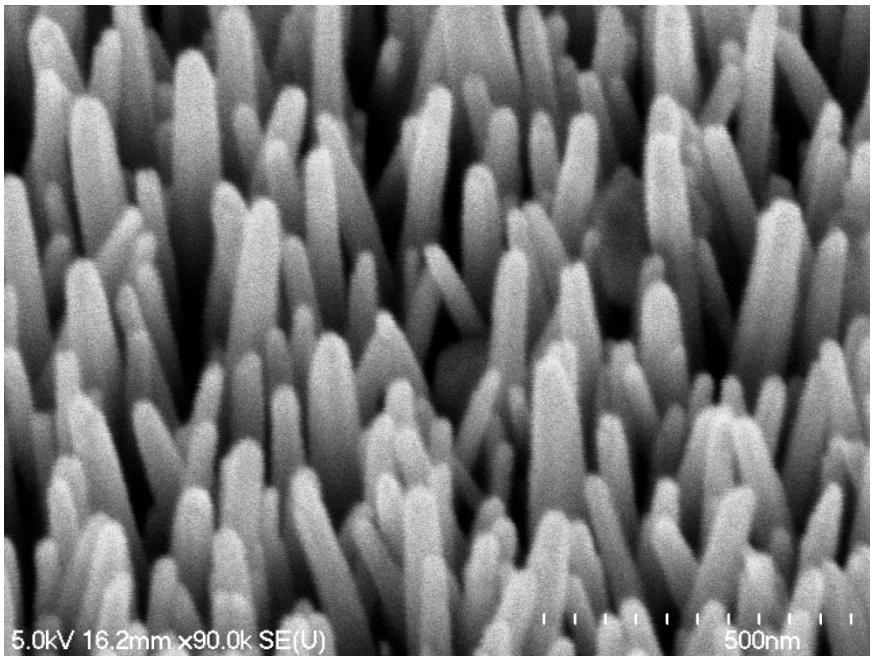

d)

Figure 4.2. SEM images of Ag-doped ZnO NWs grown in electrolyte with concentration of Ag 0.8% of Zn mass replaced by Ag on (a - b) n^+-type Si and on (c - d) Au layer.

SEM results showed that a uniform doped ZnO NWs with sharp tips were grown on these substrates. In the case of Ag-doped ZnO NWs grown on the Au layer the majority of nanowires were grown perpendicular to the surface of the substrate.

In the case of Al-doped ZnO NWs we have set the voltage at -1.8 V. Since the standard potential for aluminum is -1.66 V, the applied voltage was large compared to zinc reduction potential but just enough for aluminum reduction (this was to make sure that we were growing ZnO nanowires and not Al_2O_3).

Image analyses of Al-doped ZnO NWs grown on n-type Si are illustrated in Figure 4.3.

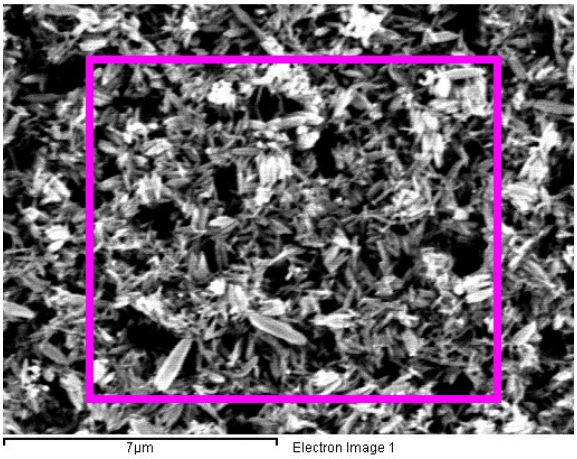

a)

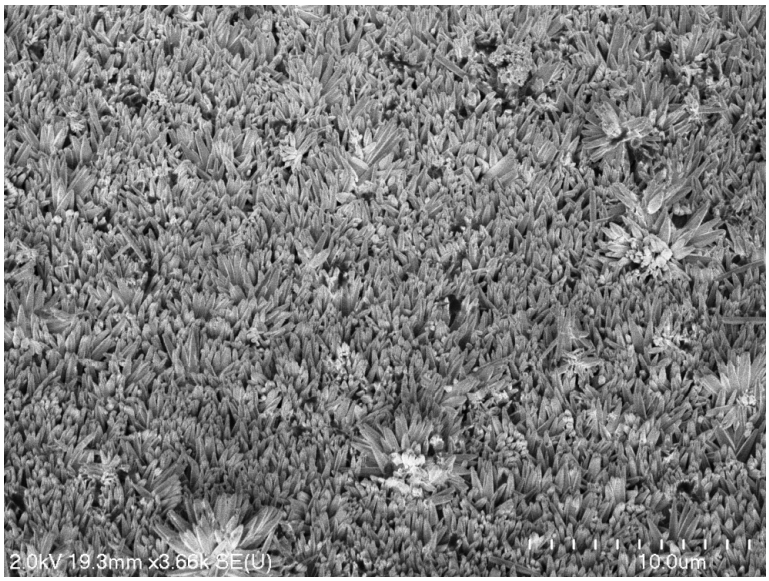

b)

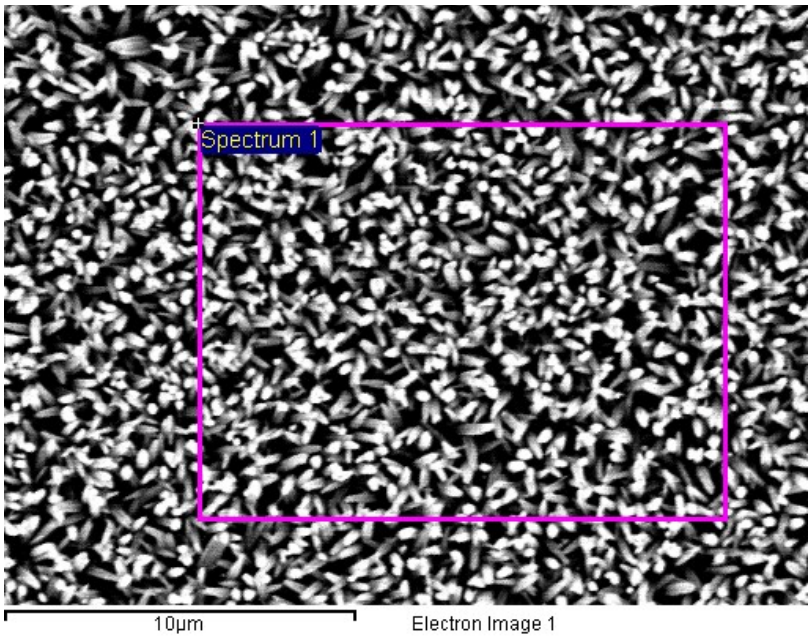

c)

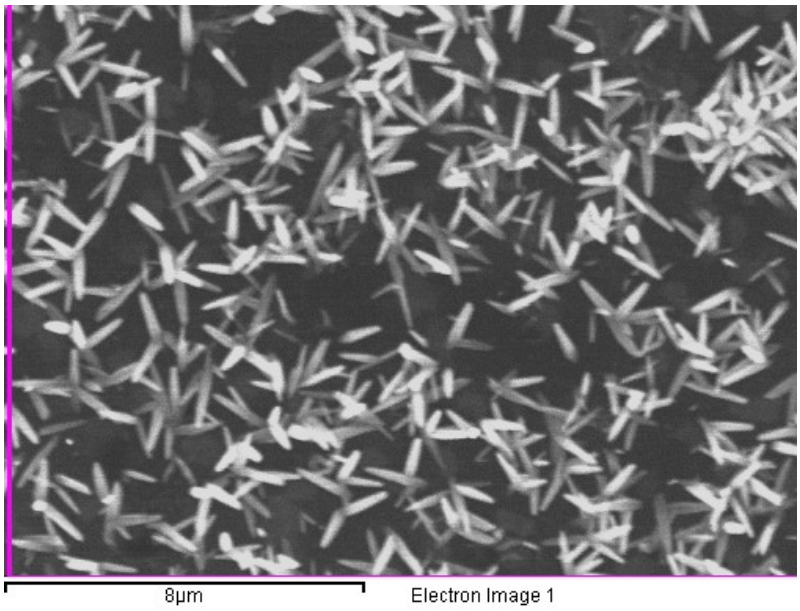

d)

Figure 4.3. SEM images of the Al-doped ZnO NWs grown on n-type Si in electrolyte with concentration of Al: a) 1.5% of Zn mass replaced by Al, b) 2.0% of Zn mass replaced by Al, c) 2.5% of Zn mass replaced by Al, and d) 3.0% of Zn mass replaced by Al.

SEM images of Al-doped ZnO NWs on n-type Si illustrated that 2.0% and 2.5% of Zn mass replaced by Al resulted in uniformly distributed nanostructures on the substrate. In

the case of 1.5 % and 3 % of Zn mass replaced by Al, the uniform distribution in the Al-doped ZnO NWs was not achieved. Similar studies are done using various substrates, analogous results were observed.

To obtain the information on the constituents of the nanowires and their distributions the elemental analysis was carried out employing Energy Dispersive X-ray Spectroscopy (EDXS).

4.2. Characterization of Doped ZnO NWs Using EDX Spectroscopy

Energy Dispersive X-ray Spectroscopy is used to identify the chemical composition of the material. EDXS in conjunction with scanning electron microscopy (SEM) employs SEM stream of electrons with high speed, which bombard the test material. Then electrons will slow down as they propagate through the matter and result in the Bremsstrahlung radiation. Bremsstrahlung radiation is defined by the electromagnetic radiation, X-rays [81]. In detail, the bombarding electrons remove the electrons from lower atomic energy levels of the material creating the vacancies. When electrons are removed from 1^{st} atomic energy levels (n = 1, K-shell of the atom) the electrons from higher atomic energy levels fall into created vacancies. If electrons from 2^{nd} atomic energy levels make transitions into 1^{st} levels, then K-alpha X-rays are emitted. If electrons from 3^{rd} or higher levels drop into 1^{st} levels, then K-beta X-rays are emitted. Furthermore, if the beam of electrons has removed electrons from the 2^{nd} atomic energy levels, L-shell of the atom, then electrons dropped from 3^{rd} levels result in the emitting of L-alpha X-rays, and the electrons fallen from 4^{th} levels into the 2^{nd} levels generate the emission of L-beta X-rays [82]. The frequencies of the emitting X-rays depend on the

difference between the atomic energy levels of atoms in the material. As it is known, the difference between energy levels of atoms is characteristic for each chemical element, and the number of X-ray emissions reflects the amount of the elements inside the material. Thus, information on chemical constituents of the material and their amounts can be obtained by detection of X-rays and their amount.

Results of the element analysis for Ag-doped ZnO NWs (0.8 % of Zn mass replaced by Ag) are illustrated in Figure 4.4.

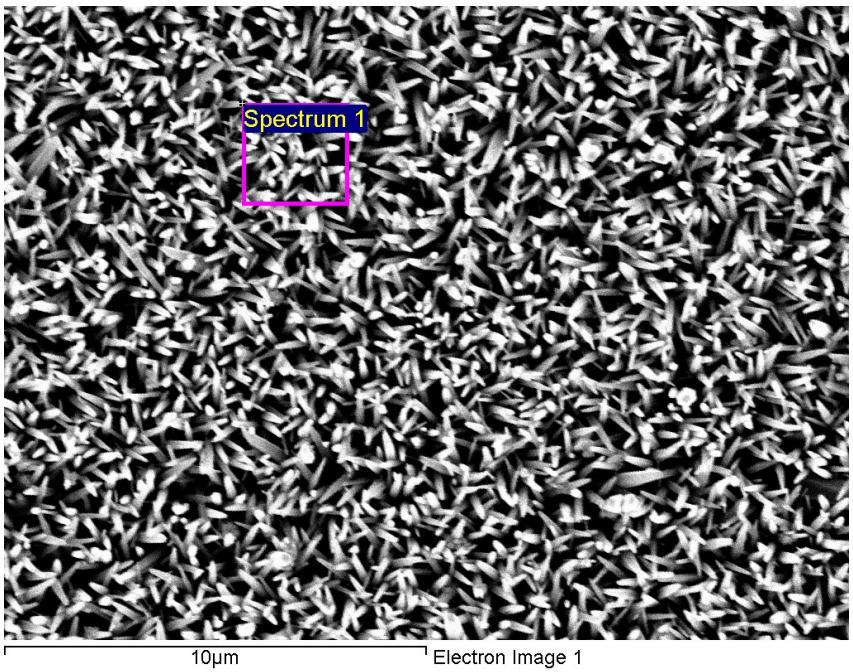

a)

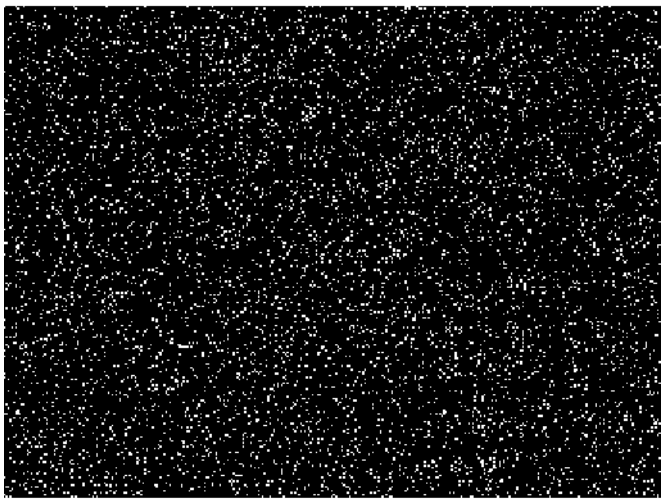

O Ka1

b)

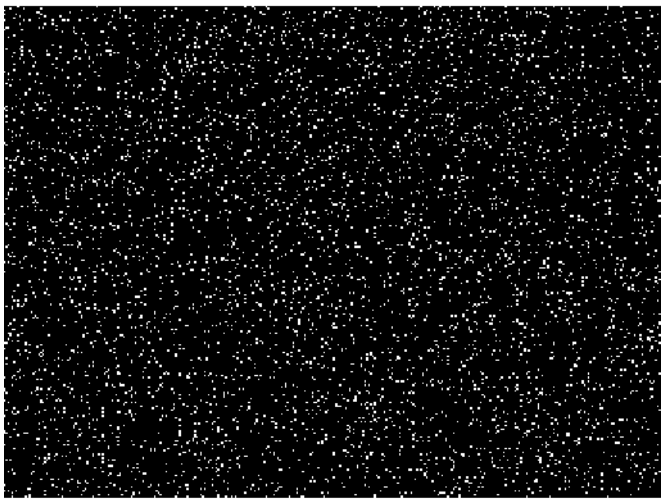

Zn La1_2

c)

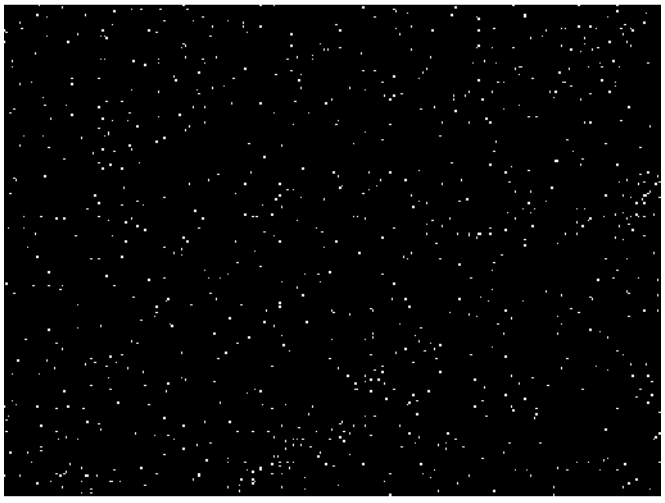

Ag La1

d)

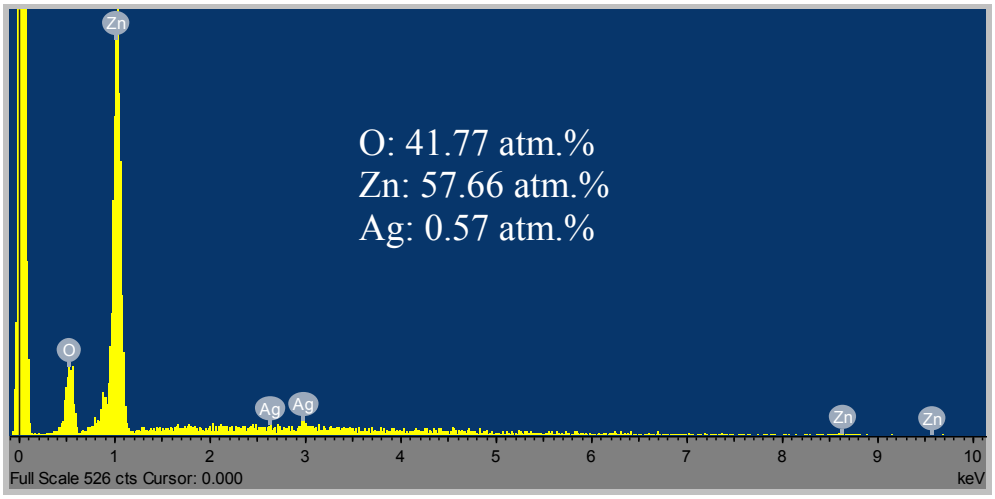

e)

Figure 4.4. EDXS analysis of the Ag-doped ZnO NWs: a) SEM image of the Ag-doped ZnO NWs electrochemically grown on n^+-type Si with the specific area used for analysis; Mapping analysis: distribution of b) oxygen, c) zinc, d) silver in Ag-doped ZnO NWs; and e) Spectrum analysis of Ag-doped ZnO NWs.

Highlighted area on the SEM image as shown in Figure 4.4 (a) illustrates the studied site, where ZnO NWs were analyzed by EDXS. First, mapping analyses are demonstrated. The results illustrate uniform distribution of oxygen, zinc, and silver inside the grown ZnO NWs. Next, Spectrum analysis of ZnO NWs has been executed. Outputs indicated high amount of Zn and O compared to the silver.

Following is the chemical element analysis of the electrochemically grown Al-doped ZnO NWs. EDXS analysis was performed for each doping concentrations, but the attained data was similar in all samples. Therefore, the results of the EDXS analysis of the sample with 2.5% of Zn mass replaced by Al shown in SEM image were reported in Figure 4.5.

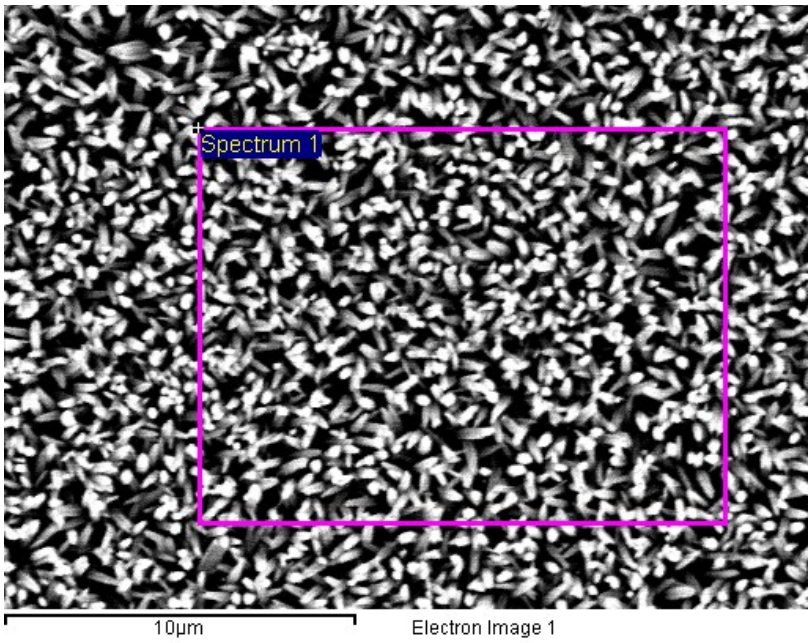

a)

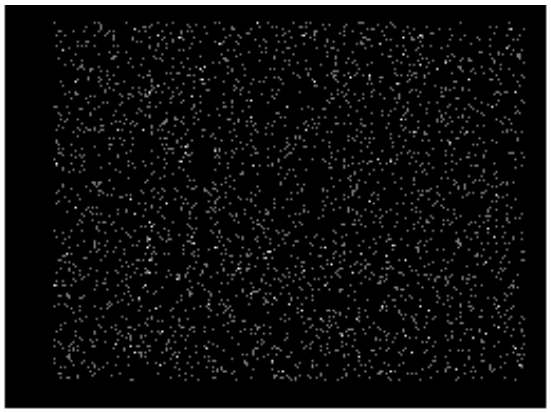

b)

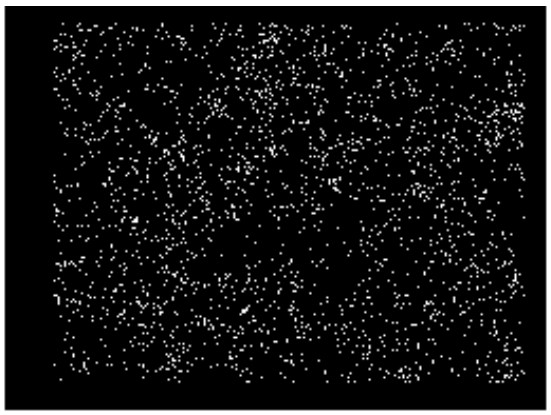

c)

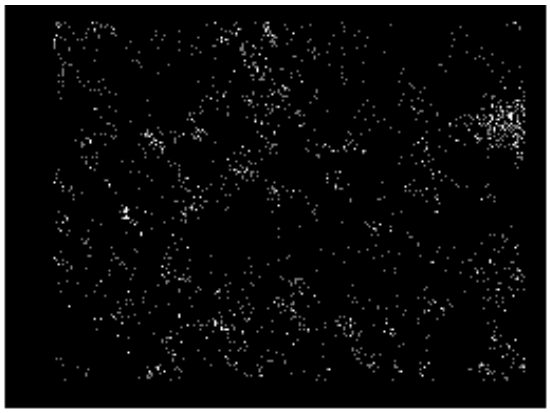

Zn La1_2

d)

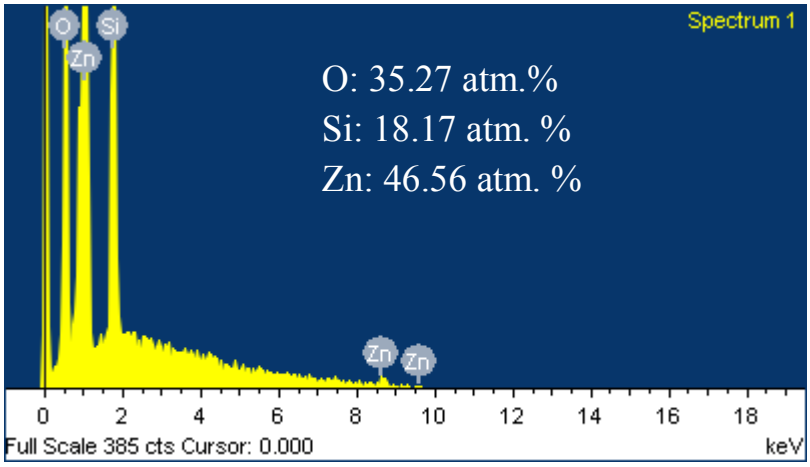

e)

Figure 4.5. EDXS analysis of the Al-doped ZnO NWs: a) SEM image of Al-doped ZnO NWs electrochemically grown on n-type Si with the specified area used for analysis; Mapping analysis: distribution of b) oxygen, c) zinc, d) aluminum in Al-doped ZnO NWs; and e) Spectrum analysis of Al-doped ZnO NWs.

SEM image of Al-doped ZnO NWs with highlighted area under investigation by EDXS is illustrated in Figure 4.5 (a). The illustration of the Mapping element analyses are shown in Figure 4.5 (b-d). Distributions of all detected chemical elements including zinc, oxygen, and aluminum were uniform inside Al-doped ZnO NWs, as demonstrated in Figure 4.5 (b - d). Spectrum analysis confirmed the existence of Zn, O, and Si inside ZnO NWs.

In summary, EDX Spectroscopy confirmed the presence and uniform distribution of silver impurities inside Ag-doped ZnO NWs as well as aluminum impurities inside Al-doped ZnO NWs. The conductivity type of the nanostructures was investigated using Photoelectrochemical (PEC) cell measurements.

4.3. Characterization of Doped ZnO NWs Conductivity Type Using PEC Cell Measurements

PEC cell is the suitable application used to detect conductive type of the nanostructures. Photoelectrochemical cell takes advantage of the fact that photons falling on the semiconductive surface can create electron-hole pairs and this effect can set up an electric potential difference across the interface in electrochemical cell.

The basic concept lying behind PEC cell measurements used in our investigation is monitoring the polarity of the open-circuit voltage shift between the dark and illuminated conditions inside PEC cell [83]. "Dark" open-circuit potential (V_{dark}) is the potential at equilibrium after explicit charge-transfer process, which result in matching the redox potential of the electrolyte and the Fermi level of the tested sample surface. Under illumination (V_{light}) by the white light source, new charge carriers were excited in the doped ZnO NWs and resulted in an open-circuit potential shift, ΔV_{oc}. A negative shift in open-circuit potential (ΔV_{oc}) is an indicative of the n-type material, and the positive shift in voltage is the confirmation that tested ZnO NWs are p-type nanomaterials [84].

In the present work, the electrolyte was 5 mM KCl diluted in DI water. The electrochemical cell was operated in galvanostatic mode: current of 0 A was applied and potential was measured. PEC cell was covered by aluminum foil to protect the tested

sample inside the solution from light. The substrate with doped ZnO NWs was applied as working electrode, and doped ZnO NWs were arranged to be facing toward the small open window in a sheet of aluminum foil. This window was made for the incident light from the white light source (Model 21AC fiber optic illuminator, CO Edmund, Industrial optics). The PEC system was standardized using known samples of n- and p-type silicon: n-type Si sample had shift of -120 mV and p-type Si sample had potential shift of +85 mV, respectively.

The characteristic PEC cell measurement for p-type material (Ag-doped ZnO NWs grown on n-type Si) is illustrated in Figure 4.6.

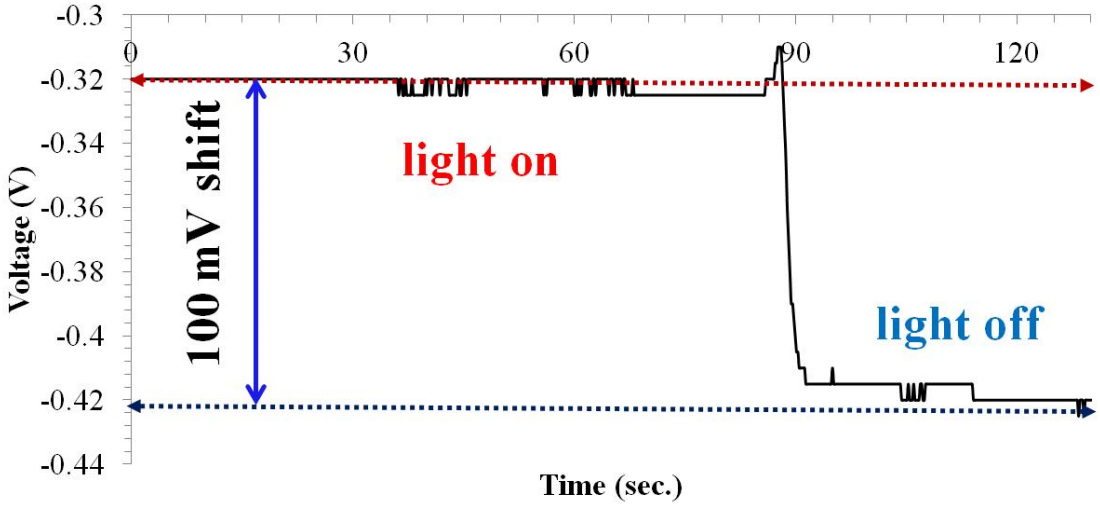

Figure 4.6. PEC cell measurement using Ag-doped ZnO NWs.

The light was applied on Ag-doped ZnO NWs and had excited electrons inside NWs to a higher energy level. Then it was turned off after 85 seconds. PEC cell measurement illustrates characteristic positive voltage shift in open circuit, when Ag-doped ZnO NWs were illuminated.

Next, Al-doped ZnO NWs were tested in PEC cell. The negative shift in the open circuit voltage was detected due to the applied light for all tested nanostructures. The experimental PEC cell measurements using Al-doped ZnO NWs is illustrated in Figure 4.7.

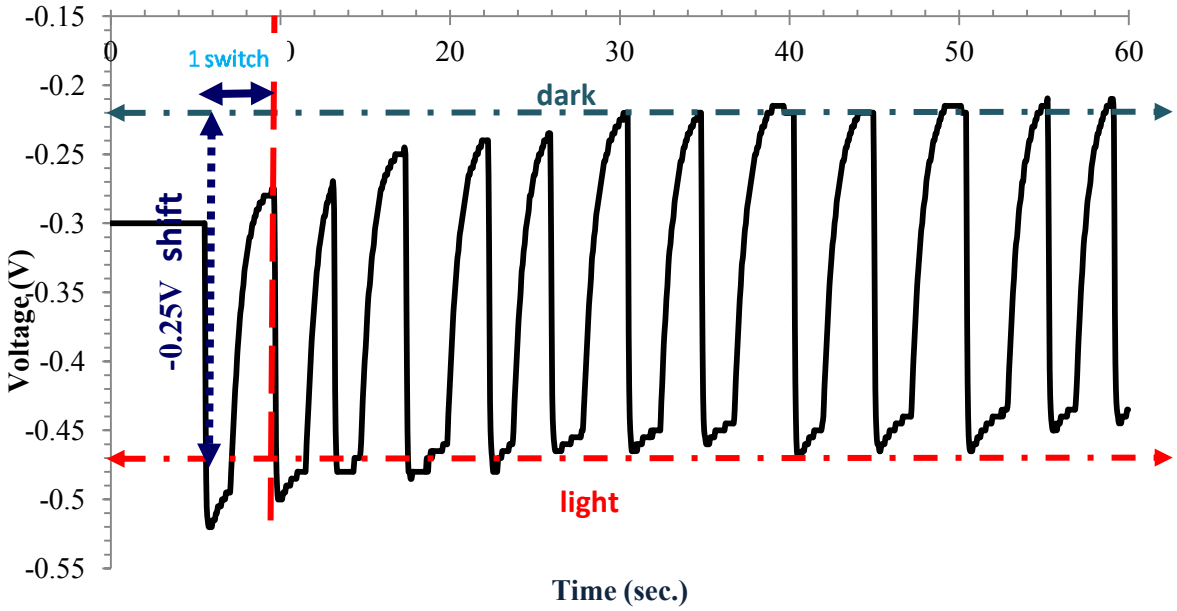

Figure 4.7. PEC cell measurement using Al-doped ZnO NWs.

As it can be seen in Figure 4.7 the voltage was measured in dark following by the applied light condition which resulted in the shift of the cathodic voltage. The test was repeated for every 4 seconds. In this experiment, excited electrons went into higher energy level inside Al-doped ZnO NWs and leading to the increased amount of conductive electrons. As a result, the value of the potential inside electrochemical cell was increased. As it was recorded in Figure 4.7, voltage shift was -0.25 V.

In the case of Al-doped ZnO NWs, we performed PEC cell measurements of the n-type substrates before growth of Al-doped ZnO NWs and after. Then the shift of open circuit voltage detected on Al-doped ZnO NWs was decreased on the value of the open

circuit voltage detected in the substrates before electrochemical deposition. Normalized shift in potential, obtained from PEC cell measurements, was recorded versus the amount of the aluminum introduced into the electrolyte as shown in Figure 4.8.

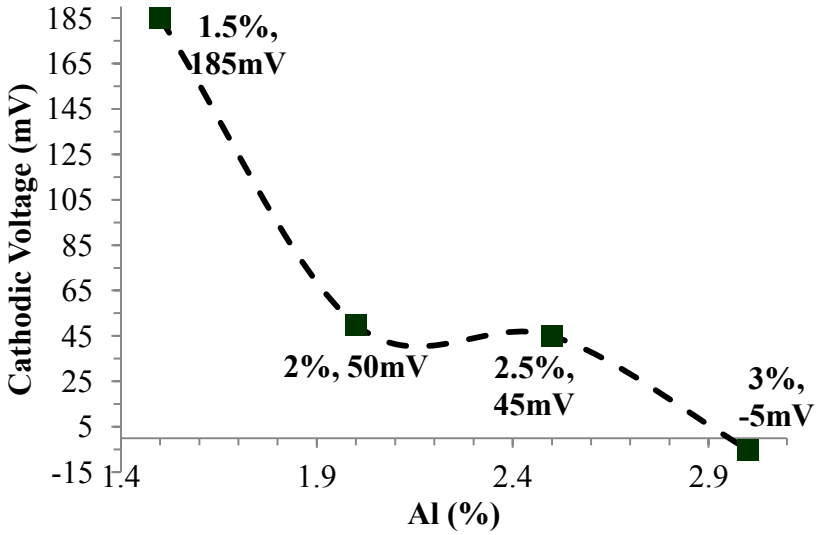

Figure 4.8. The open-circuit voltage shift in Al-doped ZnO NWs grown on n-type Si with respect to the open-circuit shift in n-type Si substrates versus amount of the Al introduced in an electrolyte.

Highest shift in the voltage, which is reflecting higher amount of the n-type doping in ZnO NWs, was for the lowest concentration of Al added into the electrolyte.

The results of the conductivity type measurements are summarized in Table 4.2. The studies on the conductivity type of the electrochemically grown Ag-doped ZnO NWs on n-type Si, on n^+-type Si, and on Au layer have confirmed p-type conductivity in these nanostructures. However, higher value of V_{oc} was detected for Ag-doped ZnO NWs grown on n-type Si. The analysis conducted on the conductivity type of Al-doped ZnO NWs illustrates negative voltage shift in all Al-doped ZnO NWs. As in the case of p-type doping, n-type doping illustrated higher open circuit shifts in Al-doped ZnO NWs grown on low conductivity n-type Si.

Table 4.2. PEC cell measurements results.

Material		V_D [mV]	V_L [mV]	ΔV_{oc} [mV]	Conductivity type
n-type Si	0.3% (Ag)	-225	-215	10	p
	0.5% (Ag)	-240	-235	5	p
	0.6% (Ag)	-225	-210	15	p
	0.8% (Ag)	-140	-100	40	p
	1.0% (Ag)	-265	-250	15	p
	1.5% (Ag)	-420	-320	100	p
	1.5% (Al)	-225	-445	-220	n
	2.0% (Al)	-270	-405	-135	n
	2.5% (Al)	-220	-465	-245	n
	3.0% (Al)	-400	-450	-50	n
Au layer	0.8% (Ag)	-300	-280	20	p
n^+-type Si	0.8% (Ag)	-160	-145	15	p

This is the first time p-type ZnO NWs and n^+-type ZnO NWs were obtained in a one-step procedure, using electrochemical deposition, to the best of our knowledge. In fact not only doping of ZnO NWs, but also the parameters, which can be engaged to fabricate NWs with controlled doping, are established in the present work. Experimental results of the PEC cell tests have shown that the doping level of the nanowires depends on the conductivity of the substrates as working electrodes. As the conductivity of the substrates was increased, the concentration of the dopant inside the nanowires was

decreased. This proved that dopant flux inside the electrolyte is due the diffusion mass transfer. Thus, we can draw the conclusion that control over the doping concentration can be achieved by employing working electrode with appropriate conductivity.

5. Gas Ionization Sensor: Application of n-type and p-type ZnO Crystalline NWs

5.1. Theoretical Background on Gas Ionization, on Field Ionization in Gases from Metallic and Semiconductor Surfaces, and on Field Emission from Metallic and Semiconductor Surfaces

Field ionization and field emission in gases lead to breakdown of gas and creation of the conduction path in gas ionization sensor (GIS). Therefore, to understand the performance of this gas detector, some theoretical background on gas ionization, field ionization and field emission in gases from metal and semiconductor surfaces is discussed in detail here. The impact of nanowires integrated into the GIS and used in Field Ionization and Field Emission modes is addressed as well.

5.1.1. Gas Ionization

In field emission, where the gas ionization process is at a pressure lower than atmospheric pressure, the breakdown follows the Townsend mechanism which is based on the phenomena of primary and secondary ionization. The primary ionization is attributed to the collisions of the electrons with gas molecules, where electrons with energy equal or higher than the gas ionization energy hit gas molecules and remove electrons from the outer shells of gas atoms, creating gas ions. Secondary ionization is caused by the bombardment of the cathode with the positively charged gas ions obtained during primary ionization, Figure 5.1.

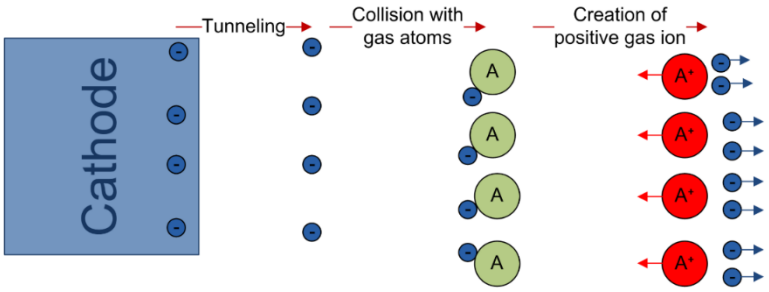

a)

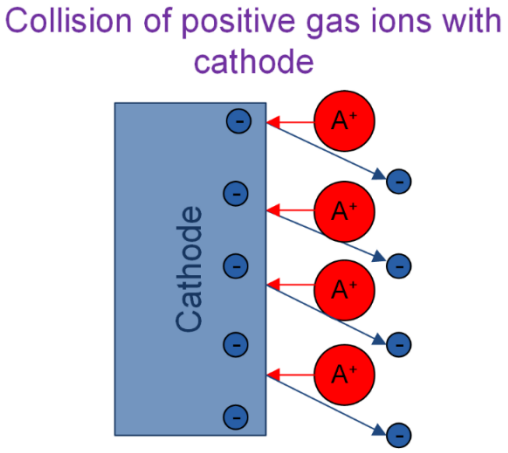

b)

Figure 5.1. a) Collision of the electrons, which were emitted from the cathode (e^-) with energy equal to or higher than the gas ionization energy, with the gas molecules (A) produces positive gas ions (A^+) and double the number of the electrons: $A+e^- \rightarrow A^+ + 2e^-$; b) collision of the positive gas ions with a cathode.

It is found that at low gas pressure the discharge is uniform. The behavior of the electric current due to increasing applied voltage comprises three distinct regions: nonlinear, saturation and Townsend discharge, as shown in Figure 5.2.

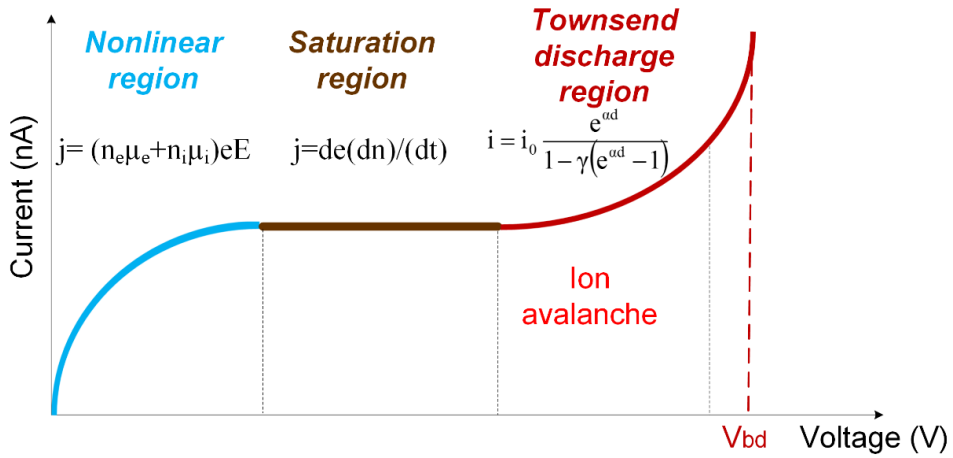

Figure 5.2. Graph of electric current vs. applied voltage, showing the three regions including discharge in the Townsend region [85].

At low electric field, the curve is nonlinear (nonlinear region). In this region the effective recombination coefficient (which is the rate of recombination of positive ions with electrons or with negative ions in a gas between oppositely charged capacitive plates of GIS) is large and as a result the density of the charged particles, as well as a current rate decreases [86]. The current density (j) in this region includes n_e and n_i, the number of the electrons per unit of volume and the number of ions per unit of volume, respectively, μ_e and μ_i are the mobilities of electrons and ions, respectively, e is an electronic charge, and E is the applied electric field.

In the next region, where the rate of ion and electron production is constant, the limiting condition is reached when all ions and electrons reach the electrodes before they have time to recombine. The total number of charges arriving at the electrodes is equal to the total number being produced [86] as it is illustrated and expressed in Figure 5.2, where d is a distance between the electrodes, $\partial n/\partial t$ is the total rate of production of charged particles per unit of volume, assuming all charged particles to be singly charged.

As the intensity of the electric field is further increasing, the Townsend discharge region is reached, where glow discharge (plasma) becomes visible. The electric current starts to rise due to the secondary ionization mechanisms (most probable is electron emission by positive-ion bombardment of the cathode since this process needs less energy). With further increasing of the applied voltage, plasma is created over the entire cathode, and an arc discharge or an electrical breakdown of the gas begins. The pre-breakdown Townsend discharge current is given in Figure 5.2, where i_0 is the current leaving the cathode, α is the first Townsend ionization coefficient (which indicates the number of ionizing collisions made on average by an electron as it travels one centimeter in the direction of the electric field), and γ is the second Townsend coefficient (which stands for the number of electrons released from the cathode caused by the secondary emission mechanisms such as liberation of electrons in the gas by collision of positive ions with the cathode or by bombardment of the negatively charged electrode by positive or metastable atoms, or by photon impact) [86]. The positive denominator results in a non-self-sustaining discharge. When the denominator is going to zero the Townsend breakdown criterion is reached, corresponding to the self-sustaining discharge and indicating that $\alpha d=\ln(1+1/\gamma)$.

Behavior of the breakdown voltage in gases was predicted by Paschen. Paschen's law states that the breakdown voltage is a function of the pressure (p) and electrode separation (d) only in the combination pd. Ideally, the Paschen's law applies in atmospheric pressures at uniform separations between electrodes (such as a pair of parallel plates) for 1 cm and more and the unvarying applied electric field inside the gas sensor [87, 88]. The Paschen's curve of the breakdown voltage versus gas pressure has

nonlinear behavior. A general formula for breakdown voltage versus gas pressure is given by

$$V_{breakdown} = \frac{E_I \cdot d}{e \cdot \lambda \left(\ln\left(\frac{d}{\lambda}\right) - \ln\left(\ln\left(1+\frac{1}{\gamma}\right)\right)\right)} \tag{5.24a}$$

$$V_{breakdown} = \frac{E_I \cdot d}{e \cdot \lambda \ln\left(\frac{d}{\lambda}\right)} \tag{5.24b}$$

where $\alpha d=\ln(1+1/\gamma)$, and formula with assumption of the Townsend discharge, where $\alpha d = 1$ or $\gamma \approx 0.582$, e is the electron charge, E_I is the ionization energy of gas, d is the distance between capacitive plates, and λ is the mean free path of charged particle [89]. $\lambda = (k_B T)/(p\pi r_I^2)$, where k_B is Boltzmann constant, T is the temperature in Kelvin, p is the pressure, r_I is the ion radius [88]. Breakdown of gas depends on the second Townsend coefficient (γ), which varies due to the physical characteristics of the gas between 0.001 and 0.1. At lower values of γ the Paschen's curve shifts to the higher pressure region as in the case of electronegative gases such as SF_6, Freon, O_2, CO_2 (these gases reattach electrons very fast). At higher values of γ the Paschen's curve shifts to the lower gas pressures region. Increasing of the second Townsend coefficient occurs when the first Townsend coefficient rises ($\alpha = (1/\lambda)\cdot\exp(-(d\cdot E_I)/(e\cdot V))$where e is an electron charge, d is the separation between charged plates, λ is the mean free path, E_I is the ionization energy of gas, and V is the applied voltage). Table 5.1 illustrates ionic radius and ionization energy of O_2, N_2, He, and Ar.

Table 5.1. Ionic radius and ionization energy of O_2, N_2, He, and Ar.

Gas	Radius [pm] from ref. [90]	Ionic energy [eV] from ref. [91]
O_2	124	13.6181
N_2	60	14.5341
He	46	24.5874
Ar	154	15.7596

The breakdown voltages versus varying gas pressures for a given separation (60μm) are obtained by implementing data from Table 5.1 as illustrated in Figure 5.3.

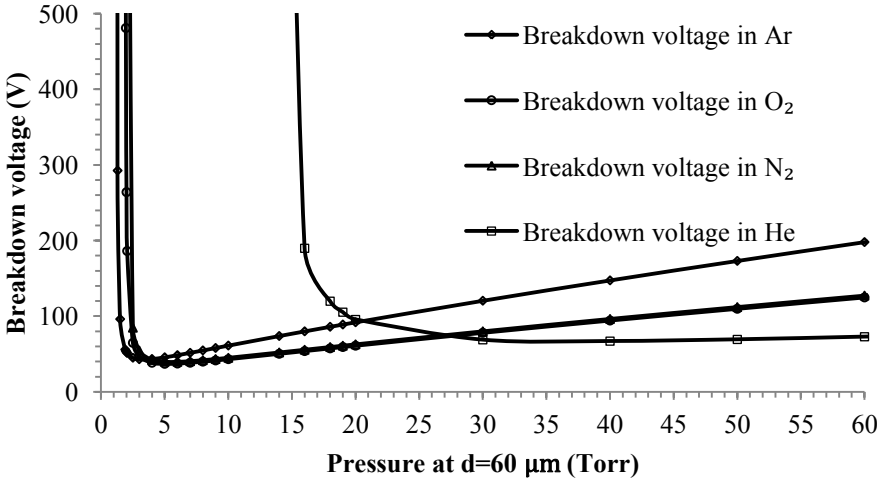

Figure 5.3. Paschen's curves in Ar, O_2, N_2, and He.

Breakdown voltage decreases with increasing gas pressure, and when the minimum value of the breakdown voltage has been reached, it starts to increase again up to the point where the breakdown voltage remains constant at greater gas pressures. The minimum value of the breakdown voltage corresponds to the highest ionizing efficiency [86]. Since

different gases have different ionization energy and ionic radius their breakdown voltages values are not the same as illustrated in Figure 5.3. The observed breakdown voltages values in oxygen and nitrogen gases are very similar compared to the breakdown in He and Ar. Gas pressures higher than 30 Torr could be used for a micrometer scaled gap between oppositely charged capacitive plates of the gas detector. In this region, the highest breakdown in Ar, following by breakdowns in N_2 and O_2 (similar value of breakdown voltages), and the lowest breakdown in He are obtained. Thus, the application of Paschen's law is limited and cannot be employed for detection of low concentrations of gases by gas ionization sensors with micro-sized gaps.

5.1.2. Field Ionization in Gases from Metal and Semiconductor Surfaces

Field ionization (FI) happens when covalent electrons of the gas molecules have enough energy to leave the gas atom and tunnel through a potential barrier into a vacant energy state of the energy levels of metal or semiconductor. In field ionization, the gas molecules become dipoles in an inhomogeneous field, where at a critical distance from the positively charged surface the dipole attraction is larger than or equal to the centrifugal force of a tangentially approaching molecule with polarizability α_p [92]:

$$-\alpha_p F \frac{\partial F}{\partial x} = \frac{mv^2}{x_c} \tag{5.3}$$

where F is electric field, x is a distance from the charged surface. The critical distance is the point where the dipole attraction is given as $mv^2/2=kT=(1/2)\alpha_p F^2$, where m is the atomic weight of the gas particle, v is the velocity ($v=(\alpha/M)^{1/2}F$ where M is the mass of the atom), k is the Boltzmann constant, and T is the temperature in Kelvin. The gas molecules attracted to the emitter surface by a polarization force, hop around the surface

and then are field-ionized when they pass through the ionization zone or at a critical distance from the emitter [93] as shown in Figure 5.4.

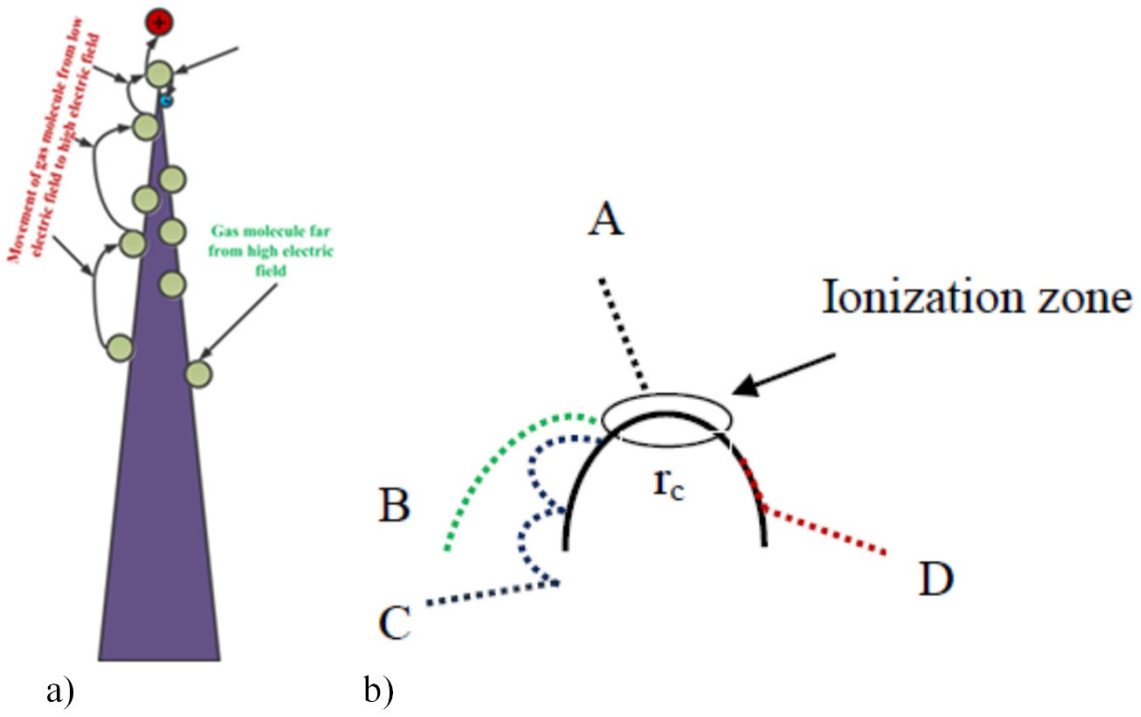

Figure 5.4. a) Ionization of a gas in the vicinity of a NW's tip, b) four ways for a gas atom to be ionized in an ionization zone: A-direct incidence, B-orbital capture, C-bouncing capture, D –adsorbed diffusion.

However, other ways for the gas atom to be ionized exist, such as orbital capture, adsorbed diffusion, and direct incidence. The last one (direct incidence) is the mode of ionization for gas molecules in the supply-limited regime as illustrated in Figure 5.4 (b, mode A). The ionization in metals occurs only when gas atom is at a critical distance from metal. In metals the critical distance is the closest distance between the atom and the conductive surface, where ground state of the atom is above the Fermi level of the metal. If the distance between the atom and the metal is shorter than the critical distance, the ground state of the atom is lower than the Fermi level of the metal, and the gas electron

has no available states to move into [94]. In the case of p-type semiconductors, the ionization can be achieved at smaller critical distance because of the defined amount of the empty states in the valence band of the semiconductor. The smaller tunneling critical distance results in an increased current, since more electrons can tunnel through a shorter distance into the semiconductor. Moreover, the ionization potential of the gas electrons is different for each gas; consequently, the electric field intensity value which would cause ejection of the electron from the gas molecule is also different for each gas.

The tunneling ionization mode, where the gas electron tunnels from gas atom to the surface of the metal or semiconductor, is taking place in the vicinity of the high local electric field at a critical distance (x_c). In this case, the electric field values are high enough to reduce the width of the potential barrier to a width comparable to the de Broglie wavelength of the electron inside the gas atom. In the proximity of the conductive metallic surface, the potential energy of a gas electron in an electric field is given as [94]

$$V(x) = -\frac{e^2}{|x_i - x|} + eFx - \frac{e^2}{4x} + \frac{e^2}{x_i + x} \tag{5.4}$$

where V(x) is the potential energy of the gas electron, $-e^2/|x_i-x|$ is the Coulomb potential attributable to a positive ion charge e located at distance x_i from the plane surface of the conductor, eFx is the potential energy of the electron due to the applied field (F), $-e^2/4x$ is the potential energy due to the electron's positive image, and $e^2/(x_i+x)$ is the potential energy due to the negative image of the ion behind the conductor surface. On the conductor's surface, the electron meets the bottom of the conduction band [94]. The schematics of the electron in a gas atom, the electron in a gas atom at applied electric field, and the electron in a gas atom near the metallic surface are illustrated in Figure 5.5.

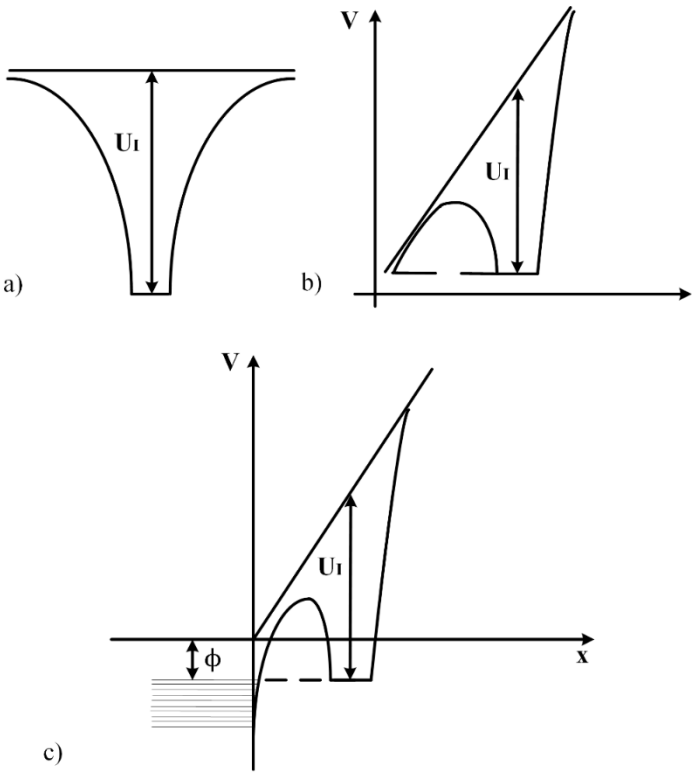

Figure 5.5. a) Potential energy of the gas electron, b) potential energy of the gas electron in an electric field, and c) potential energy of the gas electron near the metal surface [94].

To ionize the gas molecule the applied energy should be equal to or larger than the ionization energy of the gas (U_I) as illustrated in Figure 5.5 (a). With an applied electric field, the potential barrier is reduced and the electron can tunnel through when the width of the barrier is comparable to the de Broglie wavelength of the electron inside the atom as illustrated in Figure 5.5 (b). When the gas atom is near the conductive surface, the potential of the electron at the surface meets the bottom of the conduction band as illustrated in Figure 5.5 (c). The critical distance of the metallic emitter is obtained as [94]

$$\begin{aligned} eFx_c &= U_I - \phi - \frac{e^2}{4x_c} + \frac{1}{2}F^2(\alpha_a - \alpha_i) \approx U_I - \phi \\ x_c &= (U_I - \phi)/eF \end{aligned} \tag{5.5}$$

where ϕ is the work function of the metal, α_a is the polarizability of the gas atom, α_i is a polarizability of the ensuing ion. The last term in the equation represents the difference in the polarization energy before and after the ionization.

In the case of semiconductors the created electric fields are reduced compared to the electric fields in the metals because of the effect of the field penetration and the dielectric property of semiconductors. The potential energy of a gas electron near the semiconductor surface in an electric field involves field penetration and the dielectric property of the material, and it is given as

$$V(x) = -\frac{e^2}{|x_i - x|} + eFx - \frac{e^2}{4(x+\lambda)}\left(\frac{\varepsilon'-1}{\varepsilon'+1}\right) + \frac{e^2}{x_i + 2\lambda + x}\left(\frac{\varepsilon'-1}{\varepsilon'+1}\right) \tag{5.6}$$

where λ and ε' are the field penetration depth and the relative dielectric constant [95]. The work function of a semiconductor is increased due to the energy band bending ($eF\lambda$) because of the field penetration and is decreased by $4e\pi\alpha_s nF$ attributable to the field-induced polarization of the surface atoms, where α_s and n are the polarizability of a surface atom and the number of atoms per unit area of the surface, respectively [95]. The effective work function of the semiconductor ($\varphi_{effective}$) is given as

$$\phi_{effective} = eF(\lambda - 4\pi\alpha_s n) + \phi_{semicond} = \phi_s + \phi_{semicond} \tag{5.7}$$

where $\phi_{semicond}$ is the semiconductor work function. The schematic potential diagram for the ionization of gas near the p-type semiconductor surface illustrates the effective work function due to the field penetration and the field-induced polarization as shown in Figure 5.6.

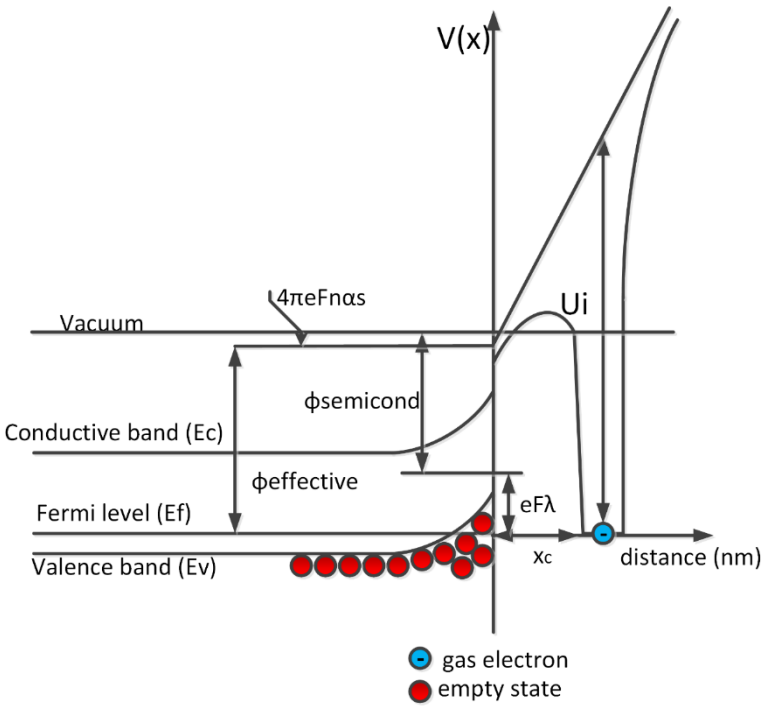

Figure 5.6. Schematics of the potential diagram for the field ionization of a gas atom in vicinity of the positively charged p-type semiconductor surface, where the effective work function is increased due to the field penetration into the surface and is decreased because of the field-induced dipole moments of the surface atoms.

In the case of a semiconductor, the critical path is decreased by the amount of the band bending and is increased by the amount of the field-induced polarization of the surface atoms (ϕ_s) [95], and it is given as

$$x_c = \frac{1}{eF}\left[U_I - \phi_{effective} - \frac{e^2}{4(x_c+\lambda)}\left(\frac{\varepsilon'-1}{\varepsilon'+1}\right) + \frac{1}{2}(\alpha_a - \alpha_i)F^2\right] = \frac{U_I - \phi_{effective}}{eF} \tag{5.8}$$

where α_a and α_i are the polarizabilities of gas and ensuing ion, respectively. In a degenerate p-type semiconductor, the critical path decreases due to the increased effective work function. This assumes that the tunneling barrier has an equilateral trapezoid geometry of the upper base x_a, of the lower base x_c and of the altitude (U_I-ΔV), where U_I is the ionization potential and ΔV is the Schottky reduction given as

$\Delta V = 2\left(e^3 F\right)^{1/2}$. The tunneling probability, assuming the Wentzel-Kramers-Brillouin (WKB) approximation, is given as

$$D(x_c) = \exp\left[-\frac{4}{3}\left(\frac{2m}{\hbar^2}\right)^{1/2}\left\{U_I - 2(e^3F)^{1/2}\right\}^{1/2}\left(x_c + \frac{1}{2}x_a\right)\right] \tag{5.9a}$$

$$D(x) = \exp\left[-\left(\frac{8m}{\hbar^2}\right)^{1/2}\int_0^x \{V(x') - E\}^{1/2}\,dx'\right] \tag{5.9b}$$

If x_a equals zero in Equation (5.9a) the potential barrier changes the geometry from equilateral trapezoid into equilateral triangle and the tunneling probability will be expressed as in Equation (5.9b) [95]. The ion current is proportional to the tunneling probability of the gas electrons in the vicinity of the metallic or semiconductor surfaces.

5.1.2.a. Formation of the Ion Current

The ion current at low electric field and at high electric field is not the same. At relatively low field (field-limited regime) the total rate of ionization is small compared to the rate of gas molecules' arrival [96]. The ion current in the field-limited regime (I_{FL}) is given as

$$I_{FL} = 2\pi r_t^2 e x_c c_t \tau^{-1} \tag{5.10}$$

where r_t is the metal tip curvature, e is the electron charge, x_c is the critical distance, τ is the characteristic time ionization ($\tau=(v_e D(x_c))^{-1}$, where v_e is the orbital frequency of the tunneling electron in the gas molecule and $D(x_c)$ is the tunneling probability $D(x_c) = \exp(-4/3(2m/\hbar^2)^{1/2}(U_I-(e^3F)^{1/2})^{1/2}x_c)$ from Equation (5.9a), and c_t is the equilibrium gas concentration near the tip. The equilibrium gas concentration is given as

$$c_t = c_g\sqrt{T_g / T_t}\,\exp\left(\left|U_p\right| / kT_g\right) \tag{5.11}$$

where c_g is the concentration far from the ionization zone, T_g and T_t are the gas and tip temperature in Kelvin, respectively, and U_p is the polarization energy ($U_p=(1/2)\alpha_p F^2$ in

eV) [96]. Since the current is proportional to the exponential of the squared electric field, the field-limited current increases with electric field intensity. Figure 5.7 shows an example of the ion current generated in the vicinity of the nanowire's apex having tip curvature 20 nm in Ar gas, where the ionization energy of the Ar molecule is 15.76 eV, $\alpha_p = 11.08 \cdot 1.64877 \cdot 10^{-41} C^2 m^2/J$ [97], the critical distance at which the electron will tunnel to the semiconductor is close to the electron's de Broglie wavelength (which is about 0.309 nm or 0.031 Å), the pressure (P) is 0.12 Torr, and the temperature (T) is 300K.

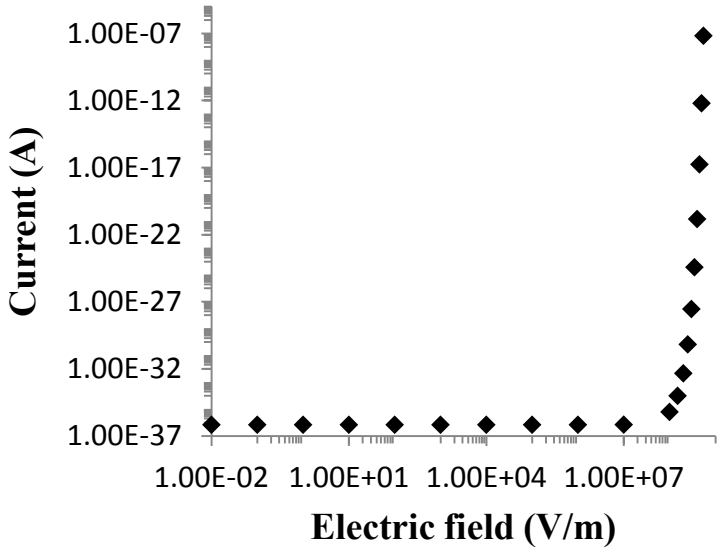

Figure 5.7. Ionization current in the field-limited regime versus the electric field in Ar gas at a pressure of 0.12 Torr, where NW's tip curvature 20 nm, the ionization energy of the Ar molecule is 15.76 eV, $\alpha_p = 11.08 \cdot 1.64877 \cdot 10^{-41} C^2 m^2/J$ [97], the critical distance 0.309 nm, and the temperature (T) is 300K.

The plot in Figure 5.7 shows two distinct regions. In the region of lower electric field, the slope is very small. In this region ion current is caused mostly by residual gases. At the higher electric fields, the slope is high and satisfies a linear relation. Here at high fields

the current depends on the ionization probability of the gas (Equation (5.9)) and proportional to the exponential of polarization energy (Equation (5.11)). Field-limited current illustrates the gas ionization in first two stages. All four ways for a gas atom to ionize in an ionization zone (A-direct incidence, B-orbital capture, C- bouncing capture, D –adsorbed diffusion) can be observed. In the intermediate currents the ionization of gas molecules depends on the way in which gas arrives into ionization zone as shown in Figure 5.4 (b) (the kinetics of the ionization). Finally, at high electric fields in supply-limited region gas atoms arrive following direct incidence into ionization zone.

In supply-limited regime, all particles approaching the charged surface become ionized. The ion current is limited by the gas supply in the ionization zone, and it is called a supply-limited ionization current (I_{SL}) [98]:

$$I_{SL} \approx 4\pi r_t^2 eY \tag{5.12}$$

where Y is the number of particles impinging on a unit surface per unit time [98], and it is given by

$$Y = \frac{P_g}{\left(2\pi mkT_g\right)^{1/2}}\left(\frac{\pi |U_p|}{kT_g}\right)^{1/2} \tag{5.13}$$

where P_g is the gas pressure. In the supply-limited regime at given constant pressure, applied voltage, and temperature of the gas, the ion current depends on the polarizability divided by the weight of the gas particle. The example of supply-limited current in Ar produced in vicinity of the NW's apex with 20 nm curvature is illustrated below. In Figure 5.8 the employed parameters were T = 300K, P = 10^{-6} Torr, α_p = $11.08 \cdot 1.64877 \cdot 10^{-41}$ C^2m^2/J [114], U_I(Ar) = 15.76 eV.

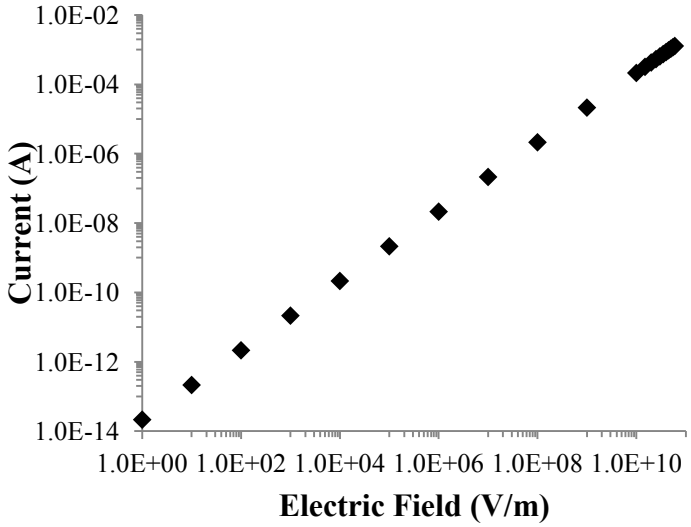

Figure 5.8. Ion current in the supply-limited regime versus the electric field in argon gas pressure of 10^{-6} Torr, where curvature of the NW tip 20 nm, the ionization energy of the Ar molecule is 15.76 eV, $\alpha_p = 11.08 \cdot 1.64877 \cdot 10^{-41} C^2m^2/J$ [97], the critical distance 0.309 nm, and the temperature (T) is 300K.

Ion current in supply-limited case illustrates linear dependence. This current can be observed after field-limited regime in high electric fields during gas ionization process.

5.1.3. Field Emission in Gases from Metal and Semiconductor Surfaces

High applied electric fields in a direction perpendicular to the metal or semiconductor surfaces lead to the emission of electrons by quantum mechanical tunneling through the surface energy barrier from electron states at the Fermi level, as it was described by Fowler-Nordheim theory, which assumes smooth and clean emitter's surface and includes Fermi-Dirac statistics for electrons. Also, the electron tunnelling is described in terms of the Wentzel-Kramers-Brillouin approximation, where the potential barrier has triangular shape [99]. The Fowler-Nordheim tunneling equation is given as in ref. [100, 101]

$$J = \lambda_z P_F a\beta^2 V^2 \phi^{-1} \exp(-v(f) b\phi^{3/2} / \beta V) \quad (5.14)$$

where λ_z is the correlation factor which includes the temperature correction factor (λ_T), the electronic-band-structure correlation factor (λ_B), and the decay-width correlation factor (λ_d) ($\lambda_z = \lambda_T\lambda_B\lambda_d^2 \approx (1.07)^{-2}$), P_F is the tunnelling prefactor (≈1), a and b are Fowler-Nordheim coefficients ($a \approx 1.541434 \cdot 10^{-6}$ AeVV^{-2} and $b = (8\pi/3)\cdot(2m)^{1/2}/eh \approx 6.830890$ eV$^{-3/2}$ nm^{-1}), β is the voltage-to-barrier-field conversion factor ($\beta = \gamma/W = F_{loc}/V_{app}$, where W is a gap between anode and cathode), v(f) is the correction function ($v(f) \approx 1\text{-}f+(1/6)f\cdot\ln(f)...$), where f is the scaled barrier field ($f = F/F_\varphi = (e^3/4\pi\varepsilon_0)(F_{loc}/\varphi^2) = (1.439964\ eV^2V^{-1}nm)\ (F/\varphi^2)$), where F_φ is the field needed to reduce to zero a Schottky-Nordheim barrier of the unreduced height (omitted reduction due to mirror effect), and it equals to the work function (φ)), and V is the applied voltage. The function v(y), that was used in some articles, corresponds to $v(f^{1/2})$. The given approximation of v(f) is valid with accuracy of better 0.0025 [102]. The electron field emission (FE) energy diagrams for metal and n-type semiconductor surfaces are illustrated in Figure 5.9.

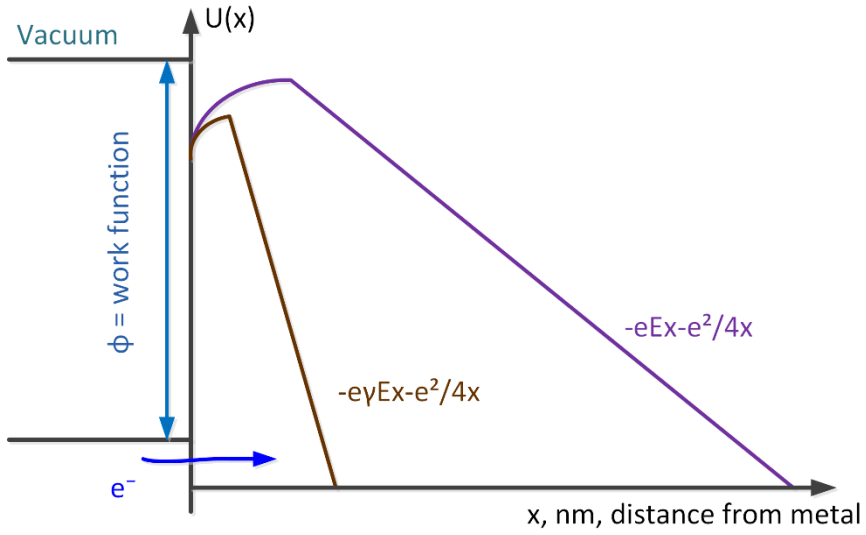

a)

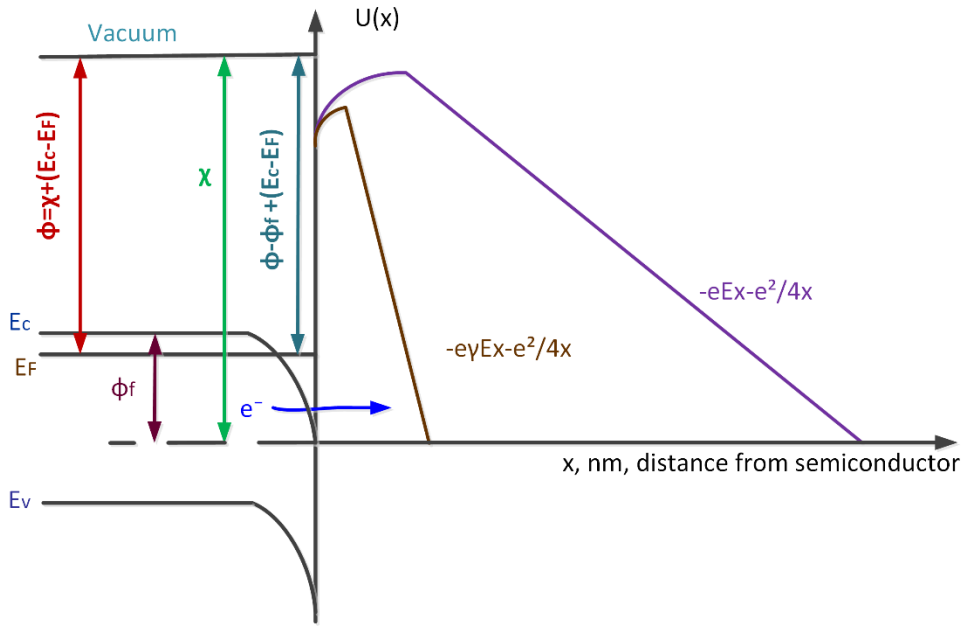

b)

Figure 5.9. Energy-band diagrams a) for the electron field emission from metal, and b) for the electron field emission from n-type semiconductor surfaces.

The length of the tunnelling path depends on the applied voltage and the field enhancement factor, as well as on the height of the barrier.

The work function of the semiconductor is given as the energy between the vacuum and the Fermi energy level, and it has higher values compared to the metal work functions. Therefore, the emission of the electrons from semiconductor will be at higher applied electric fields compared to the values of the applied electric field in metals. To improve field emission in semiconductors, doping can be used to move the Fermi level closer to the conduction band (in n-type semiconductor), or the conductor emitters' morphology and geometry can be designed to achieve a high field enhancement factor.

From experimental I-V characteristics of the field emission device, the work function or the enhancement factor of the field emitters can be calculated using the relationship

$$\ln\left[\frac{I}{V^2}\right] = -\frac{v(f)\cdot b\cdot \phi^{3/2}}{\beta\cdot V} + \ln\left(\frac{A\cdot a\cdot \beta^2}{(1.07)^2\cdot \phi}\right) \tag{5.15}$$

where β is the enhancement factor per meter and A is the emitter's surface. By drawing the graph ln(I/V²) versus 1/V from experimental data, the negative slope ($-\frac{v(f)\cdot b\cdot \phi^{3/2}}{\beta}$) and intersection with ln(I/V²) axis ($\ln\left(\frac{A\cdot a\cdot \beta^2}{(1.07)^2\cdot \phi}\right)$) will provide the necessary information for calculation of the work function of the semiconductor or calculation of the enhancement factor (γ=β·W). Illustrations of the current density and calculations of enhancement factor from the slope are illustrated in Figure 5.10.

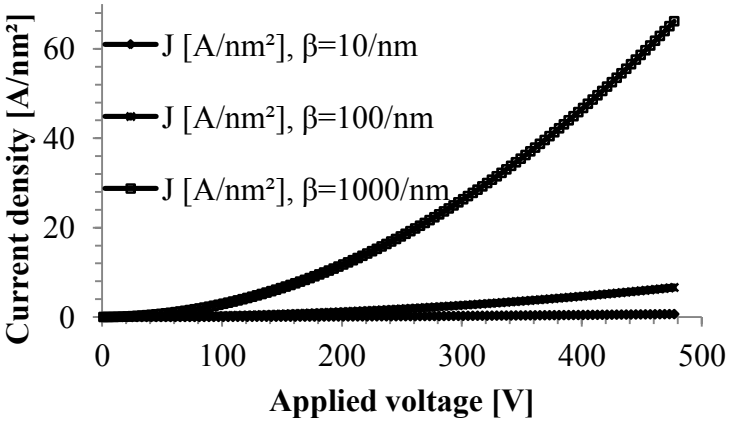

a)

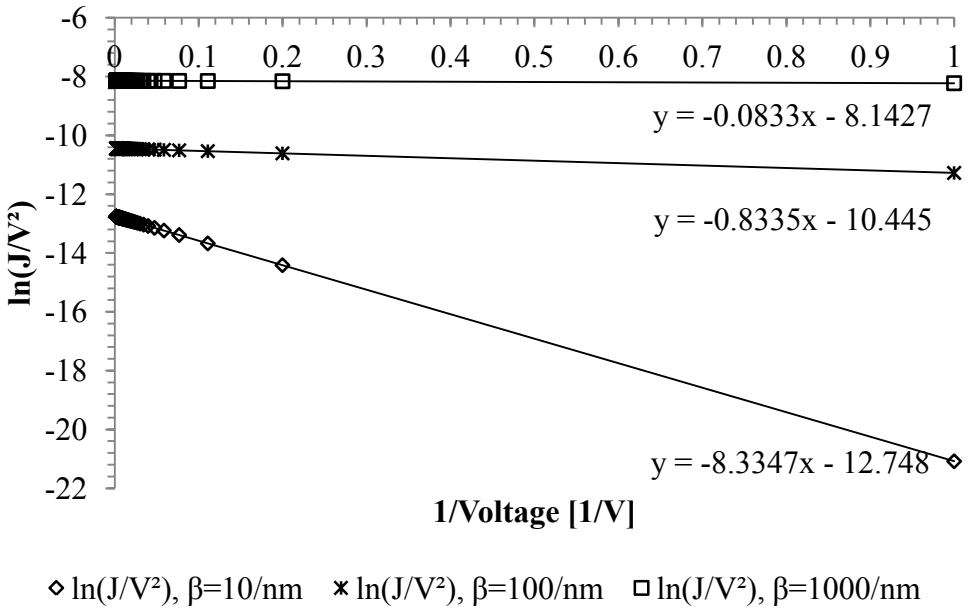

b)

Figure 5.10. a) Current density in a gap of 60 μm with β = γ/nm of 10/nm, 100/nm, or 1000/nm and work function = 5.3 eV, b) ln(J/V²) versus 1/V from the current density curves.

Using the slopes of the curves we can calculate the enhancement factors for a given current densities. The slope in this case is given as $-\frac{v(f)\cdot b\cdot \phi^{3/2}}{\beta}$. β_1 = 10/nm, $\beta_2 \approx$ 100/nm, and $\beta_3 \approx$ 1000/nm are extracted from the slope if v(f) ≈ 1, as it was assumed in Figure 5.10 (a).

5.1.4. Geometrical Field Enhancement

To improve the efficiency of the field ionization and field emission

- ✓ the critical distance should be decreased (more charged particles could tunnel through)
- ✓ the area of the high local electric field should be increased

- ✓ the emitted electrons from the surface should possess high energy to move the electron from the gas atom.

Decreasing the critical distance in the case of the field ionization and creation of the emitted electrons with high energy in the case of FE can be achieved by increasing the local electric field near the NWs apexes. This can be achieved by employing the novel morphologies of the electrochemically grown ZnO NWs as conical shape of NWs' apexes and small protrusions with large curvatures on them. Other geometrical parameters, which cause increase of the electric field, are aspect ratio and spacing between the NWs. The enhancement factor (γ) includes geometrical parameters of the nanowires and their distribution in an array. Also, enhancement factor of the array of electric field emitters represents the relation between applied and local electric field intensities, and it is given as

$$\begin{aligned} \gamma_0 &= b\left(L/r+h\right)^{0.9} \\ \gamma &= \gamma_0\left[1-\exp\left(-a\frac{s}{L}\right)\right] \end{aligned} \tag{5.16}$$

where γ_0 is the enhancement factor of one electric field emitter, h, a and b are the adjustment values, L/r is an aspect ratio of NWs (L is the length of the NW and r is the radius), and s is the spacing between NWs. If $s \ll L$ then the field enhancement factor is given as

$$\gamma = \gamma_0 \times a \times \frac{s}{L} = a \times b \times \left[L/r+h\right]^{0.9} \times \frac{s}{L} = C \times \left[L/r+h\right]^{0.9} \times \frac{s}{L} \tag{5.17}$$

where C is the alterable parameter and h is chosen - 26 in ref. [103]. Multiple protrusions on the nanotips generate a high enhancement factor because of high curvatures of the

nanoprotrusions, and increase the available surface having high local electric field. The enhancement factor for one nanowire with nanoprotrusions of similar geometries is given as

$$\gamma_0 = \gamma_{nanoprotrusion} \times \text{number of nanoprotrusions} \tag{5.18}$$

where it is assumed that all nanoprotrusions have about the same enhancement factor values.

5.2. Simulations of GIS with ZnO NWs as Anode/Cathode (COMSOL)

ZnO NWs have been proven experimentally to be well suited for field ionization and field emission applications. An optimized capacitive device (GIS) with ZnO NWs field ionization array is developed using the COMSOL software. The effects of the NWs geometry and their between-wire spacing on the enhanced electric field and total energy stored were investigated using Multiphysics Partial Differential Equation (PDE) and Electrostatics modules.

5.2.1. Theoretical Background on Electrostatics

The general governing equations for the electrostatic model were (1) $\nabla \times \mathbf{F} = \mathbf{0}$, where F is the vector electric field, (2) the Poisson's equation ($\nabla^2 V = -\rho/\varepsilon$, where ε is the permittivity of the material, V is the applied potential, and ρ is the volume charge density), and (3) the Laplace's equation ($\nabla^2 V=0$). In our model, the material was nonpolarizable and nonmagnetizable, and the volume charge density (ρ_v) was expressed as $\rho_v = \nabla \cdot \mathbf{D} = \varepsilon \nabla \cdot \mathbf{F}$ where **D** is the electric displacement field vector. The boundary conditions used in the electrostatics simulations are described in Appendix A.

The applied electric field is given as

$$F_{applied} = \frac{V}{d} \tag{5.19}$$

where d is the space between two oppositely charged electrodes in the GIS model. The field enhancement factor (γ) defines the amplification in an applied electric field intensity caused by the geometry of the NW, and it is given as

$$\mathbf{F}_{\text{loc}} = \gamma \mathbf{F}_{\text{applied}} \tag{5.20}$$

where E_{loc} is the augmented electric field near the NW pinnacle. The energy density or energy per unit volume of the electrostatic field (w_e) is defined by

$$w_e = \frac{1}{2} \varepsilon F^2 \tag{5.21}$$

and the total energy stored in the field or the work to assemble a static charge distribution (W) is given as

$$W = \int_V w_e dV \tag{5.22}$$

where V is the volume between the two electrodes in the GIS model.

5.2.2. Simulation Results Using Models of GIS with ZnO NWs

The equation-based modeling (PDE, partial differential equation in coefficient form) and AC/DC module (electrostatics) were used for 2D and 3D GIS models, respectively.

To study the field intensity in the vicinity of the NW apexes, the electrostatic model of the GIS with an incorporated NW on one of the plates in the middle was considered. The geometries of the models are recorded in Table 5.2.

Table 5.2. Geometries of the GIS models used in simulations.

3D model of GIS with 1 nanowire		2D model of GIS with 5 nanowires	3D model of GIS with 9 nanowires
Diameter of conductive plates (Au) = 2 μm Separation between the plates = 60 μm Thickness of plate = 100 nm			
Conical shape of NW	d_{base} = 100 nm	d_{base} = 100 nm d_{tip} = 20 nm $r_{curvature}$ = 3 nm	d_{base} = 200 nm d_{tip} = 40 nm $r_{curvature}$ = 10 nm
Hexagonal NW	d =100 nm		
Hexagonal NW with decreased tip	d_{base} =100 nm d_{tip} = 20 nm		

The voltage applied on the plate with NW was 400 V, and the opposite plate was grounded, 0 V. The volume between the conductive plates was filled with air at $1.333 \cdot 10^{-5}$ Pa, close to a vacuum. Outside the region containing air, the volume boundary condition was 0 V. The described electrostatic model with the Dirichlet boundary conditions and the investigated NW geometries are illustrated in Figure 5.11.

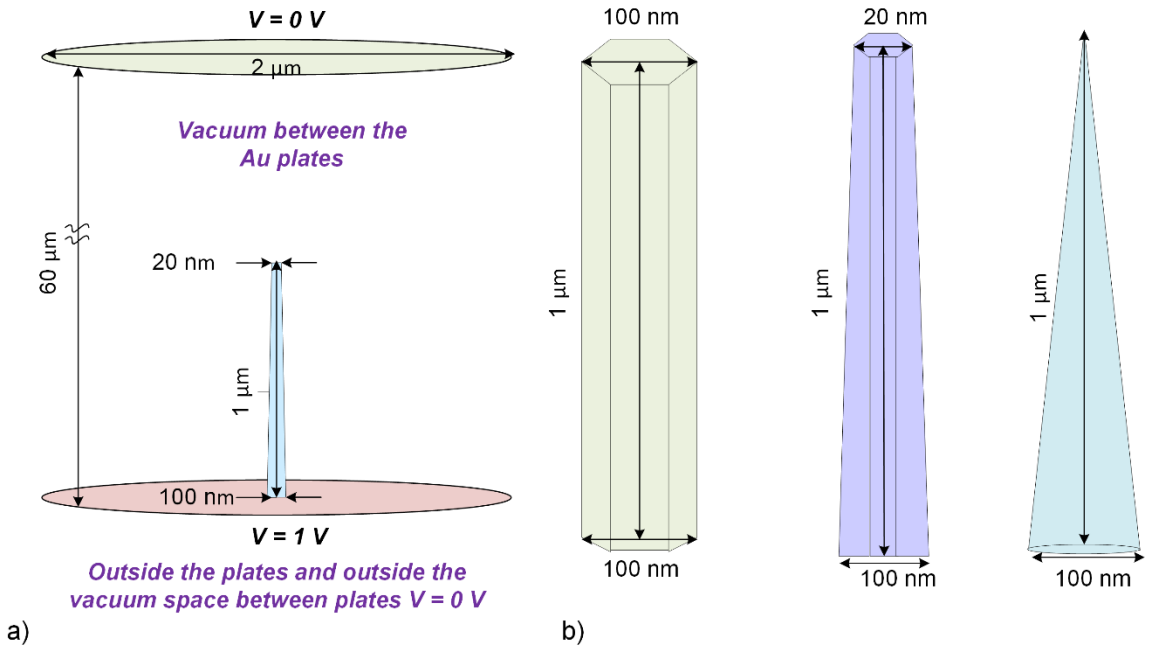

Figure 5.11. Schematics of a) a GIS model and b) the three modeled geometries of NW as described in Table 5.1.

Three shapes of ZnO NWs were considered, as illustrated in Figure 5.11 (b). Investigations of the effect of the variations in the applied voltage and of the space between ZnO NWs on electric field intensity were performed using 2D and 3D models using the same boundary conditions. Meshed models where the geometry of the NW, distribution of nanowires in 2D and 3D models investigated are shown in Figure 5.12.

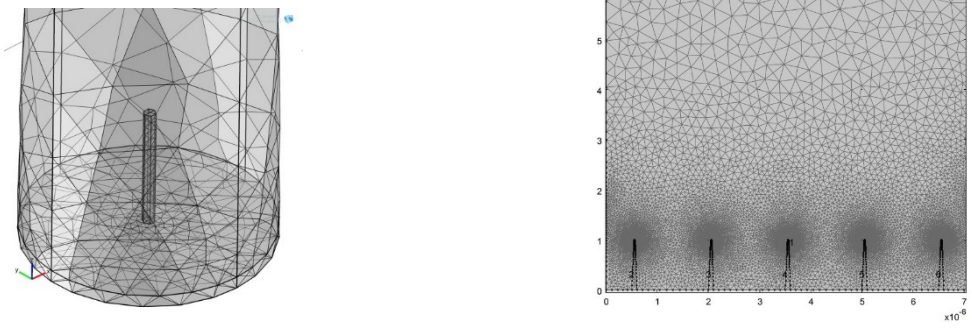

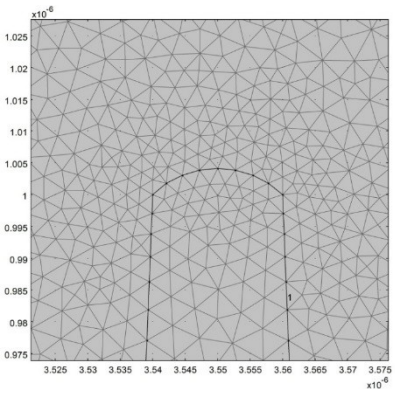

c)

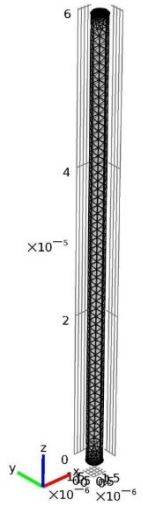

d)

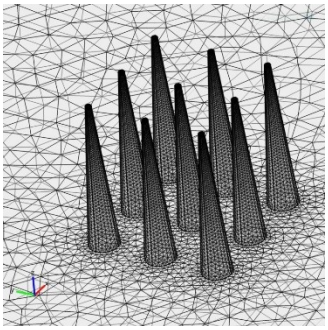

e)

Figure 5.12. a) Meshed 3D GIS model with 1 ZnO NW in Electrostatics application, (b-c) meshed 2D GIS model in PDE module, and (d-e) meshed 3D GIS model in Electrostatics.

In all of the GIS models simulated in this work, ZnO material was used for the nanowires, surrounded by air. The meshing element was free tetrahedral as illustrated in Figure 5.12. The mesh was user-defined, where the number of tetrahedral elements was increased in the region of the nanowires. The particulars of the mesh parameters are disclosed in Appendix A. Dirichlet boundary conditions were used with V = 0 V on all boundaries except plate with ZnO NWs where constant voltage was applied.

Next the distribution of the electric field in the vicinity of the nanowires, total energy stored between capacitive plates of GIS, as well as the screening effects were considered in GIS models as illustrated in Table 5.3.

Table 5.3. Parameters considered in simulations of GIS models.

Model	Electric field	Total energy stored between capacitive plates of GIS	Screening effect
3D GIS model with 1 NW 2D GIS model with 5 NWs 3D GIS model with 9 NWs	Figure 5.13 and Figure 5.14	Figure 5.15	Figure 5.16

Coefficient based model was used because the important parameters under consideration were represented as coefficients in PDE module. These parameters are the charge density represented as source term (f) and the dielectric constant of the medium represented as diffusion coefficient (c). In following simulations the electrostatic analysis was considered, where the dielectric constant was 9.16 for nanowires. In 3D model, 9 ZnO NWs were situated in the middle of the positively charged plate. First, the direction of the electric field and its distribution in ZnO NWs incorporated into GIS model were studied, Figure 5.13.

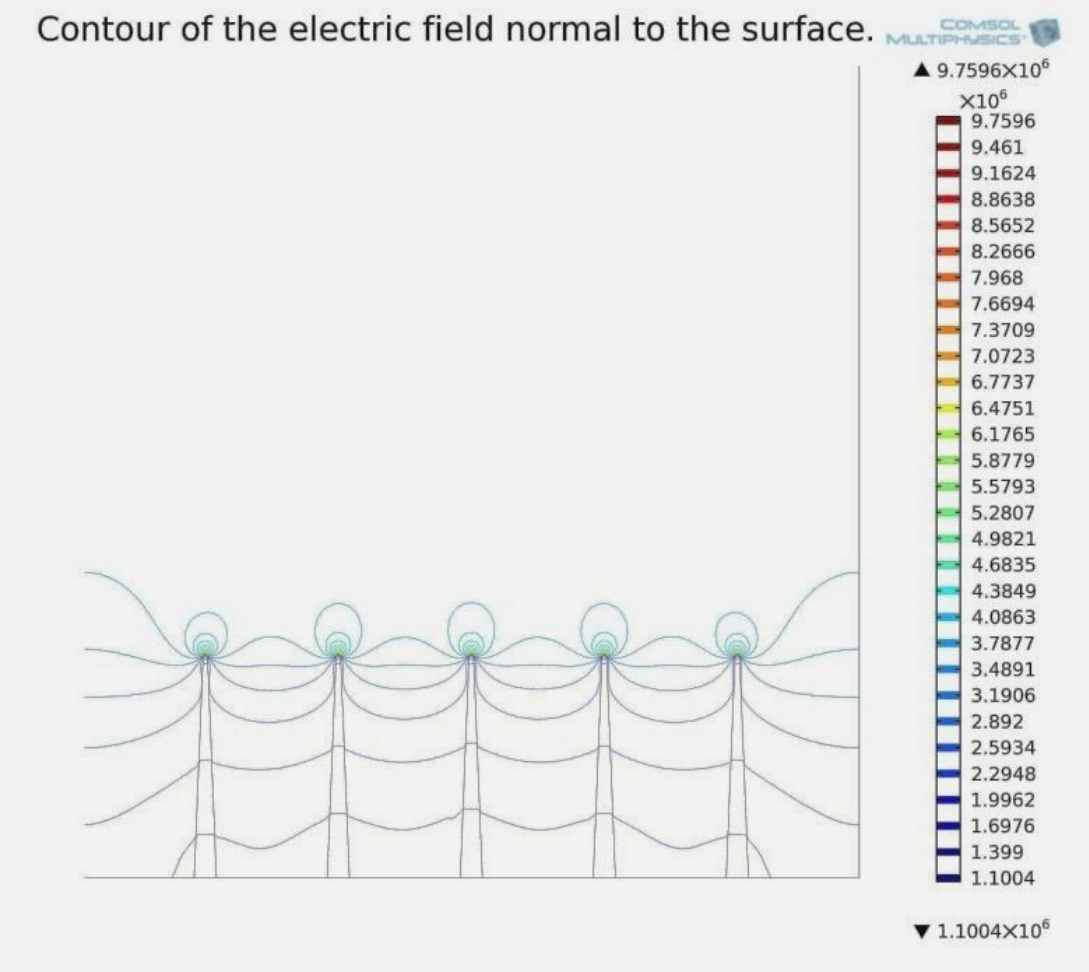
Contour of the electric field normal to the surface.
COMSOL MULTIPHYSICS
▲ 9.7596×10^6
×10^6
9.7596
9.461
9.1624
8.8638
8.5652
8.2666
7.968
7.6694
7.3709
7.0723
6.7737
6.4751
6.1765
5.8779
5.5793
5.2807
4.9821
4.6835
4.3849
4.0863
3.7877
3.4891
3.1906
2.892
2.5934
2.2948
1.9962
1.6976
1.399
1.1004
▼ 1.1004×10^6

a)

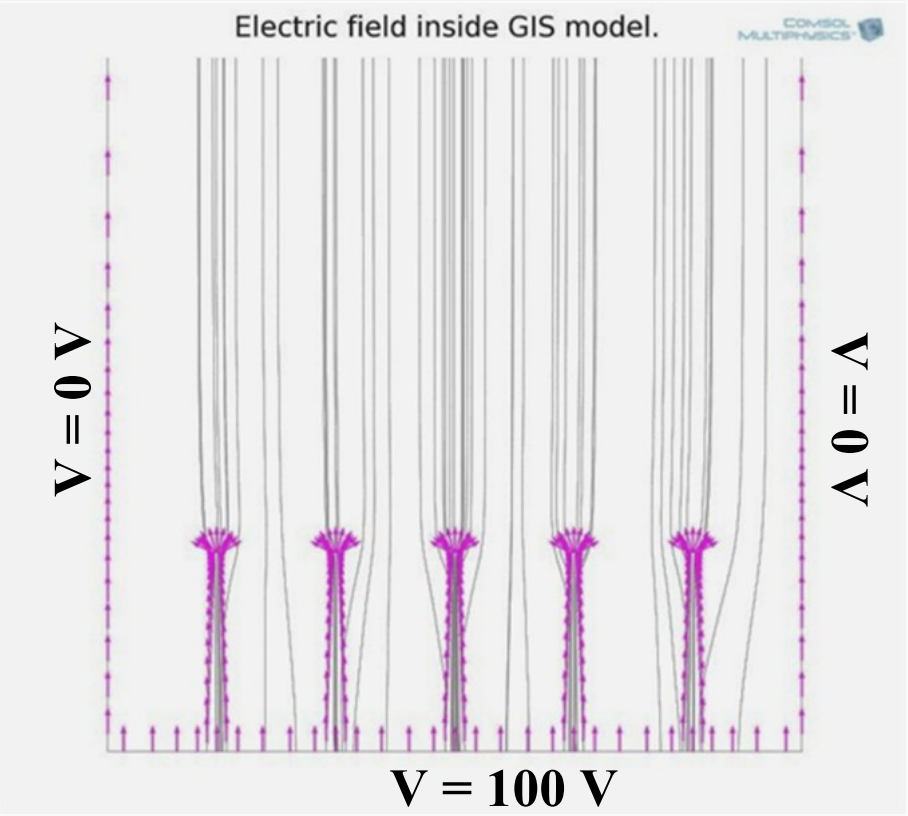
Electric field inside GIS model.
COMSOL MULTIPHYSICS
V = 0 V
V = 0 V
V = 100 V

b)

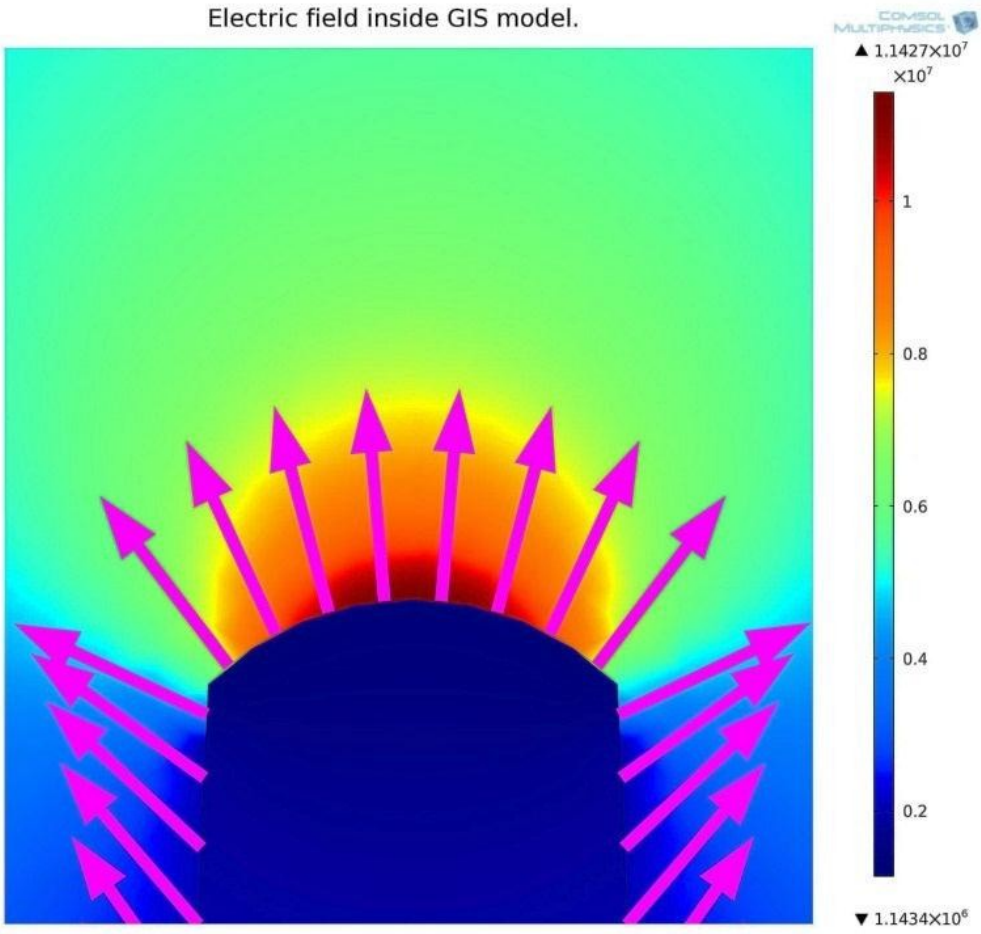
Electric field inside GIS model.
▲ 1.1427×10^7
×10^7
1
0.8
0.6
0.4
0.2
▼ 1.1434×10^6

c)

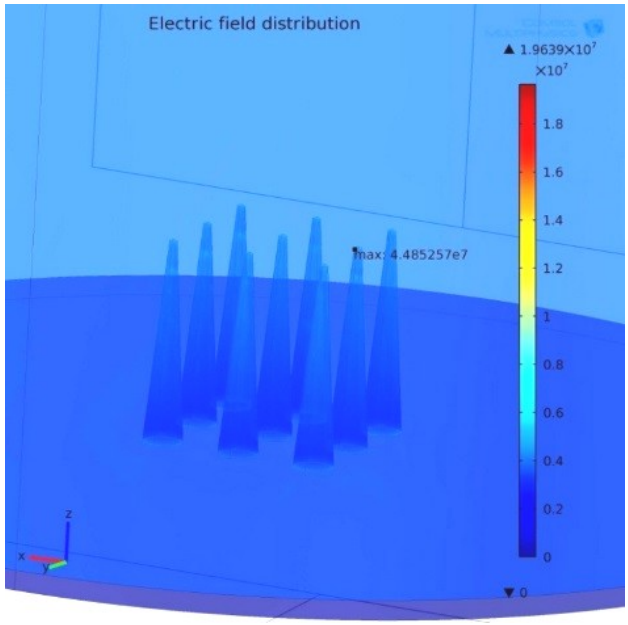
Electric field distribution
▲ 1.9639×10^7
×10^7
1.8
1.6
1.4
1.2
1
0.8
0.6
0.4
0.2
0
▼ 0
max: 4.485257e7

d)

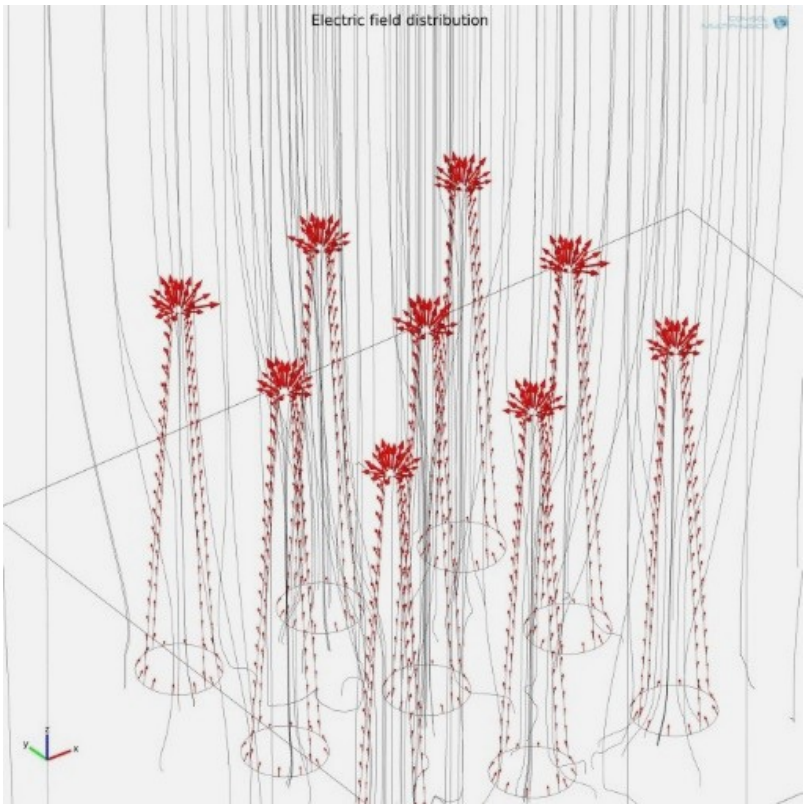

e)

Figure 5.13. Equipotential lines of electric field in 2D GIS model in vicinity of the ZnO NWs (a), direction and density of the electric field intensity (b), electric field in the vicinity of the NW's tip (c), distribution and density of the electric field intensity in 3D GIS model (d), and distribution of the electric field in NWs of 3D GIS model (e).

The electric field intensity in FI mode was considered, where applied voltage on ZnO NWs was 80V in 2D GIS model. The equipotential lines represent the amount of the electric field in different colors as demonstrated in Figure 5.13 (a). These lines are always directed perpendicular to the electric field vector direction. It can be seen that there is a low electric field intensity generated between the nanowires (equipotential lines have dark blue color), Figure 5.13 (a) and Appendix A. The highest electric field is observed in the vicinity of NWs pinnacles (dark red color) or densely distributed arrows. Surface of the NWs apexes provides the highest values of the electric field intensity. Reducing intensity of the electric field can be observed as the electric field moving further from the

tip. To attain better understanding on the behavior of the electric field between NWs and in vicinity of the NWs tips we looked at the direction of the electric field and its intensity. The highest intensity of the electric field was obtained in NWs as shown in Figure 5.13 (b). Multiple lines representing the electric field vectors with included x and y directions components originate from positively charged surface and go through NWs, Appendix A. On the tip's surface lines have small curvatures, since apex of NW has curvature, and electric field is always perpendicular to the surface. Direction of the electric field is almost in the y-direction, perpendicular to the electrodes. Following simulation results from 3D GIS model illustrate uniform distribution of the electric field in vicinity of the NWs pinnacles and directed perpendicular to the curved surface of NWs apexes.

Next, the readings of the maximum electric field intensity in the normal direction to the capacitive plate along 1 NW in 3D model with single nanowire as shown in Figure 5.11 were obtained. The maximum local electric field in a vicinity of the conical NW's apex was observed, Table 5.4.

Table 5.4. Geometry of the NW versus local electric field.

Geometry of the NW's tip	Conical	Hexagonal flat tip (diameter of the tip = 20 nm)	Hexagonal flat tip (diameter = 100 nm)
F [V/m]	$7.2 \cdot 10^8$	$3.2 \cdot 10^7$	$2.0 \cdot 10^7$

Large accumulation of the charged particles in curved tip resulted in maximum local electric field directed perpendicular to the apex surface. The maximum electric field intensity was detected in conical shape of ZnO NW. Thus, maximum field enhancement factor was detected in the conical NW geometry, 108, and minimum was obtained in the

hexagonal NW, 3. As for the hexagonal NW with decreased diameter of the tip, the field enhancement factor was 4.8. Numerical results illustrate rapid increase in the value of the electric field intensity, when the shape of the tip became sharp (conical NW's geometry).

To investigate the behavior of the electric field intensity at the vicinity of the NWs tips all three models were used. The electric field was studied on the path which goes through the NW situated in the middle of the array (2D) or in the middle of the capacitive plate (3D) at varying applied voltages. The created paths in models are shown in Appendix A. The electric field intensities along specified paths at varying applied voltages for all models are shown in Figure 5.14.

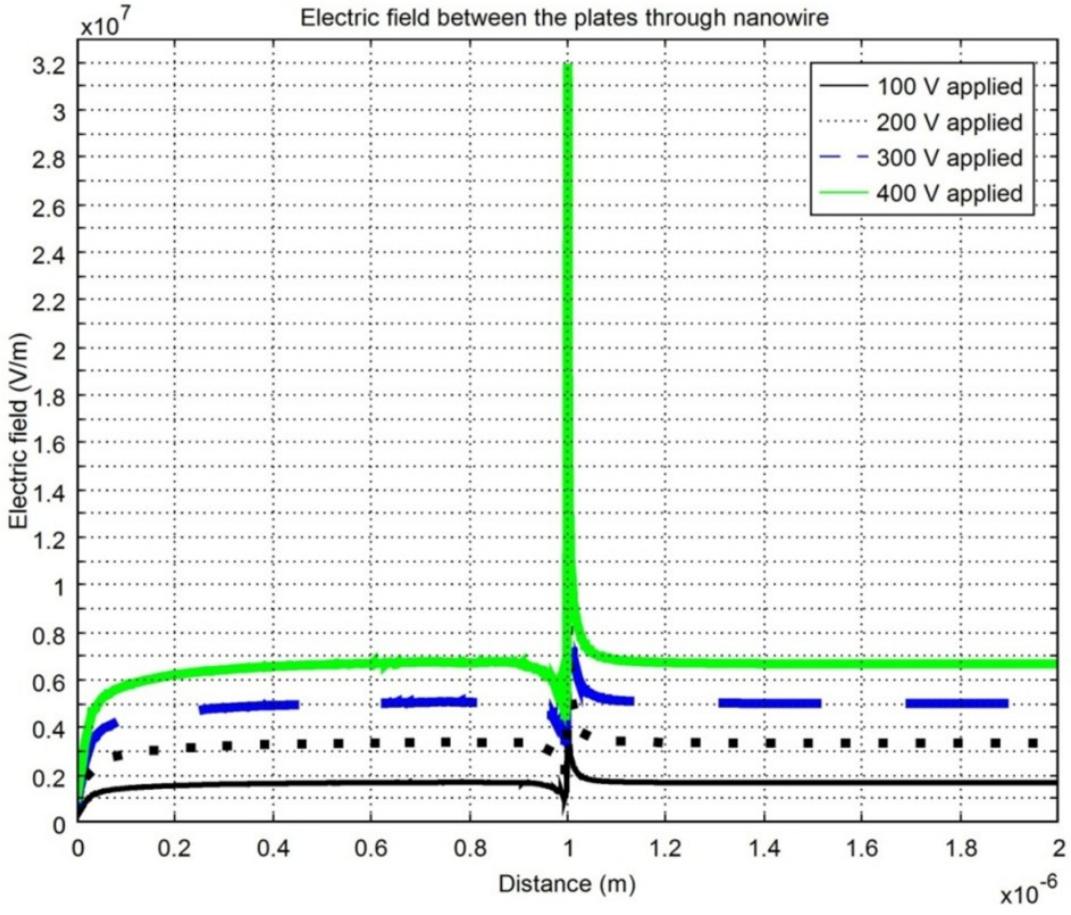

a)

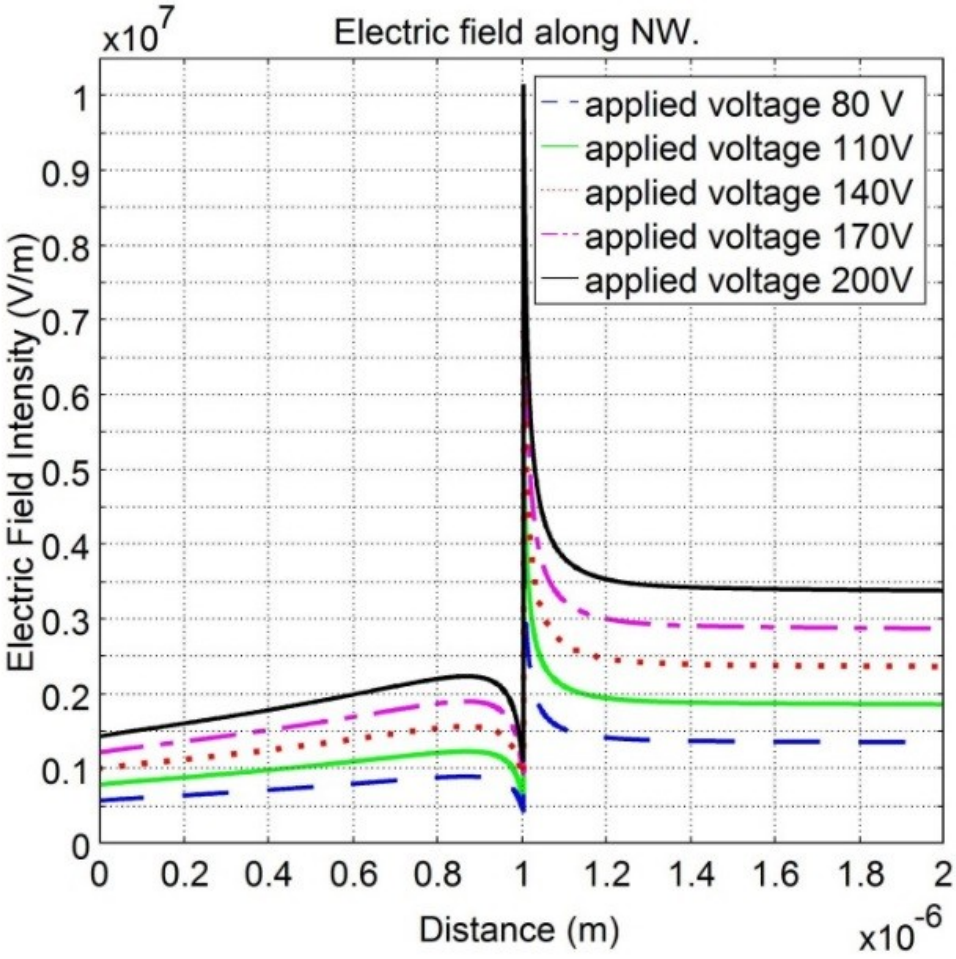
Electric field along NW.
x10^7
Electric Field Intensity (V/m)
Distance (m)
x10^-6
applied voltage 80 V
applied voltage 110V
applied voltage 140V
applied voltage 170V
applied voltage 200V
0
0.1
0.2
0.3
0.4
0.5
0.6
0.7
0.8
0.9
1
0
0.2
0.4
0.6
0.8
1
1.2
1.4
1.6
1.8
2

b)

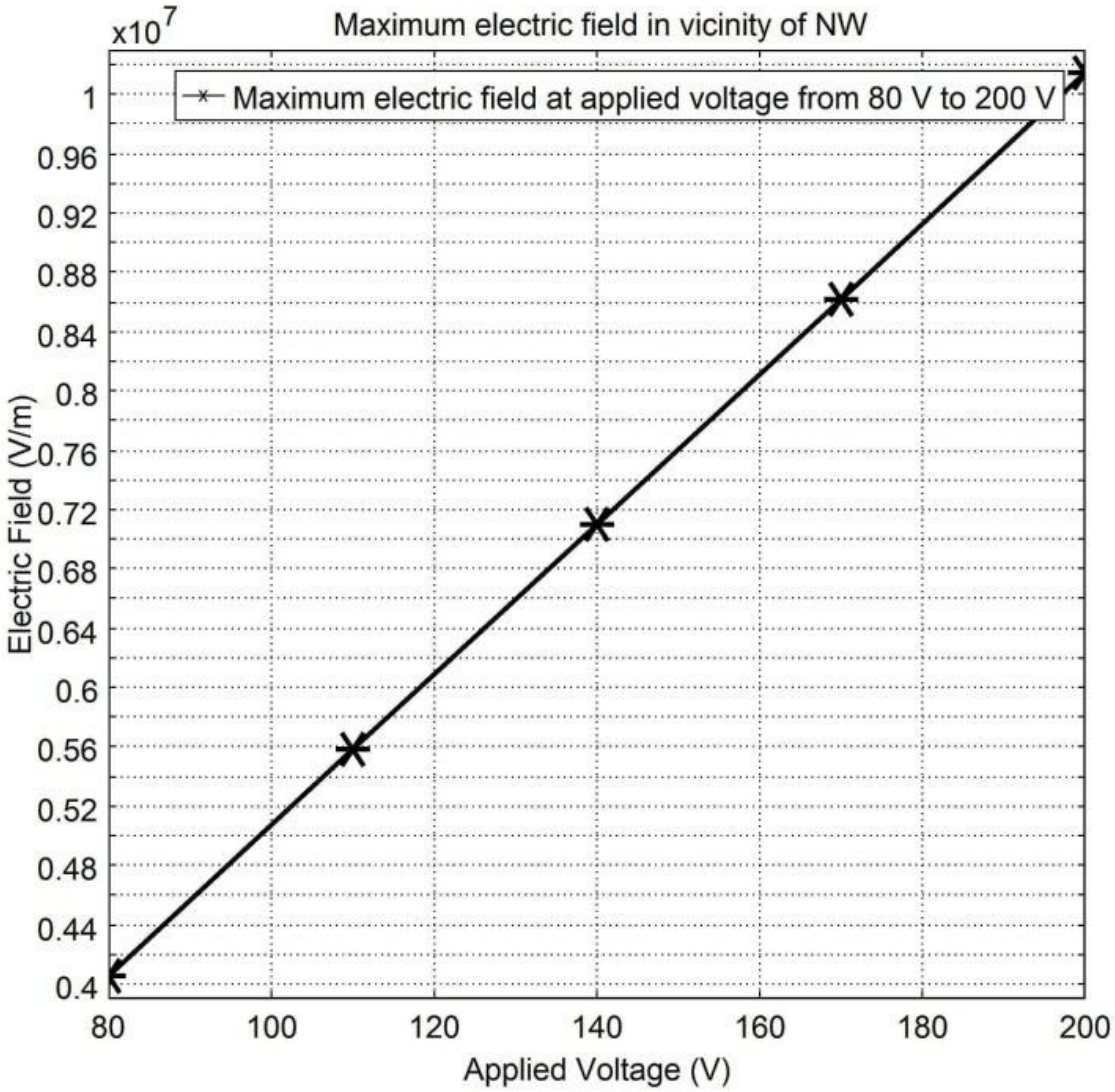
x10^7
Maximum electric field in vicinity of NW
Maximum electric field at applied voltage from 80 V to 200 V
Electric Field (V/m)
Applied Voltage (V)
1
0.96
0.92
0.88
0.84
0.8
0.76
0.72
0.68
0.64
0.6
0.56
0.52
0.48
0.44
0.4
80
100
120
140
160
180
200

c)

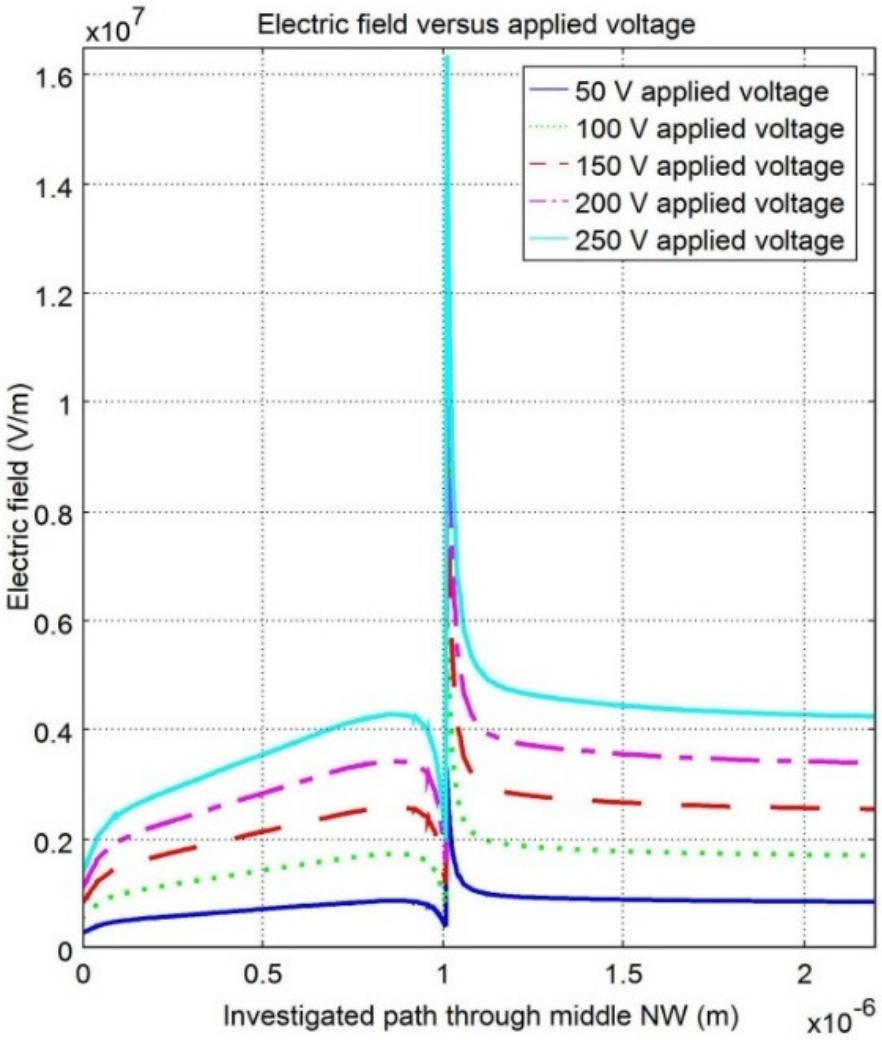
Electric field versus applied voltage
x10^7
1.6
1.4
1.2
1
0.8
0.6
0.4
0.2
0
Electric field (V/m)
50 V applied voltage
100 V applied voltage
150 V applied voltage
200 V applied voltage
250 V applied voltage
0
0.5
1
1.5
2
Investigated path through middle NW (m)
x10^-6

d)

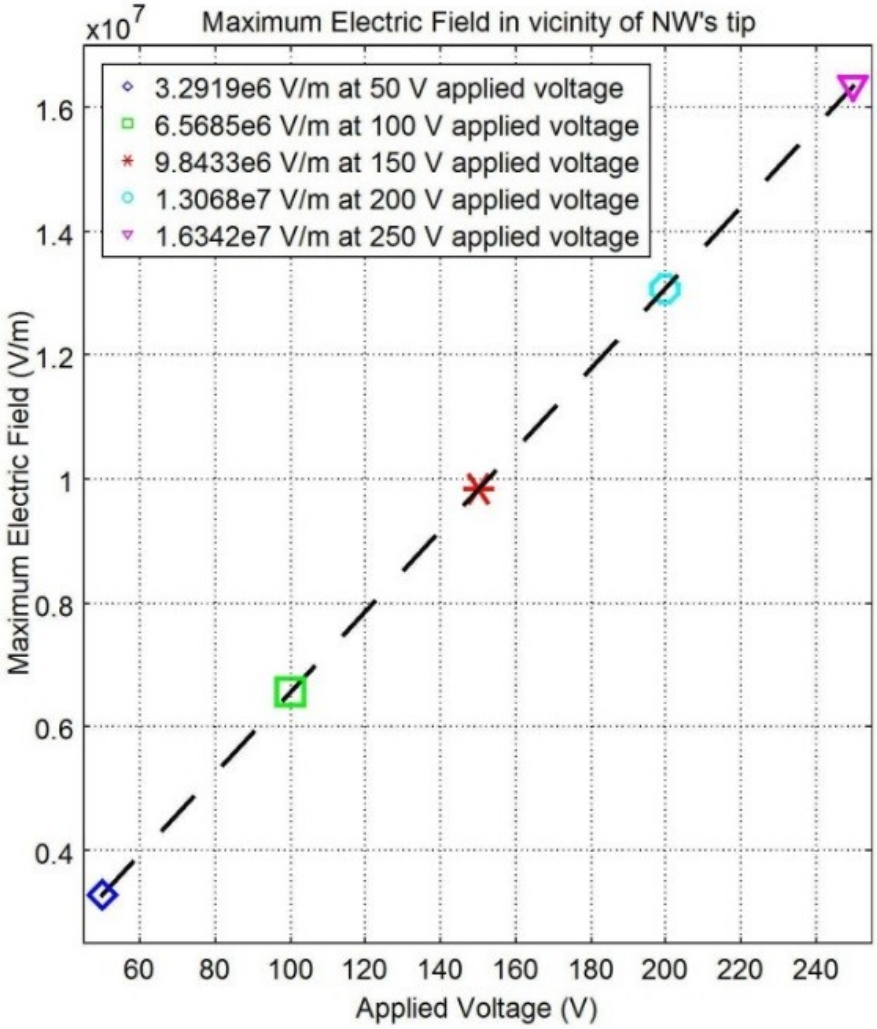

e)

Figure 5.14. a) Electric field on the path between parallel capacitive plates along the hexagonal NW with decreased diameter of the tip (20 nm), b) electric field intensity through ZnO NW in direction perpendicular to the charged plates in 2D model, c) the maximum values of the electric field versus the applied voltages in 2D GIS model, d) electric field detected on the studied path through NW at the different applied voltages in 3D GIS model, e) maximum electric field values versus the applied voltages in 3D GIS model.

Intensity of the electric field between parallel gold plates on the path along the NW axis rapidly increased and reached its maximum value in the vicinity of the NW's pinnacle. Then the value of the electric field intensity was decreased quickly down to the value of the applied electric field created between the plates due to the applied voltage. For the

applied voltage of 400 V $F_{applied}$ was equal to 400 V/60 μm = $6.667 \cdot 10^6$ V/m. The value of the electric field intensity increased from $6.667 \cdot 10^6$ V/m to $3.2 \cdot 10^7$ V/m in the vicinity of the NW apex at 1 μm from the plate on the path along NW. The simulations illustrated linear increase in the local electric field due to the applied voltage. Maximum value of the electric field intensity was observed in vicinity of the NW apex in all models as illustrated in Figure 5.14. The field enhancement factor at applied voltage of 200 V is 1.95 in 3D model with 1 hexagonal NW, 3.06 in 2D GIS model, and 3.1 in 3D GIS model. The results on detection of the electric field demonstrate that the curvature of the tip and decreasing of the tip's radius increase the value of the electric field. Also, the value of the ratio between local and applied fields versus applied voltage increases with applied voltage. For instance, at applied voltage of 250 V in 3D GIS model the enhancement factor is increased from 3.1 at applied 200 V to 3.92. In 3D model with 1 NW factor increased from 1.95 at 200 V to 4.8 at 400 V. Also, in 2D GIS model the increase from 3 at 80 V to 3.06 at 200 V was observed.

The energy density has the highest value near the NWs pinnacles; therefore, gas molecules will tend to ionize in the vicinity of the NWs tips. Total energy stored between oppositely charged capacitive plates at a range of the applied voltages illustrated nonlinear dependence on the applied voltage as shown in Figure 5.15.

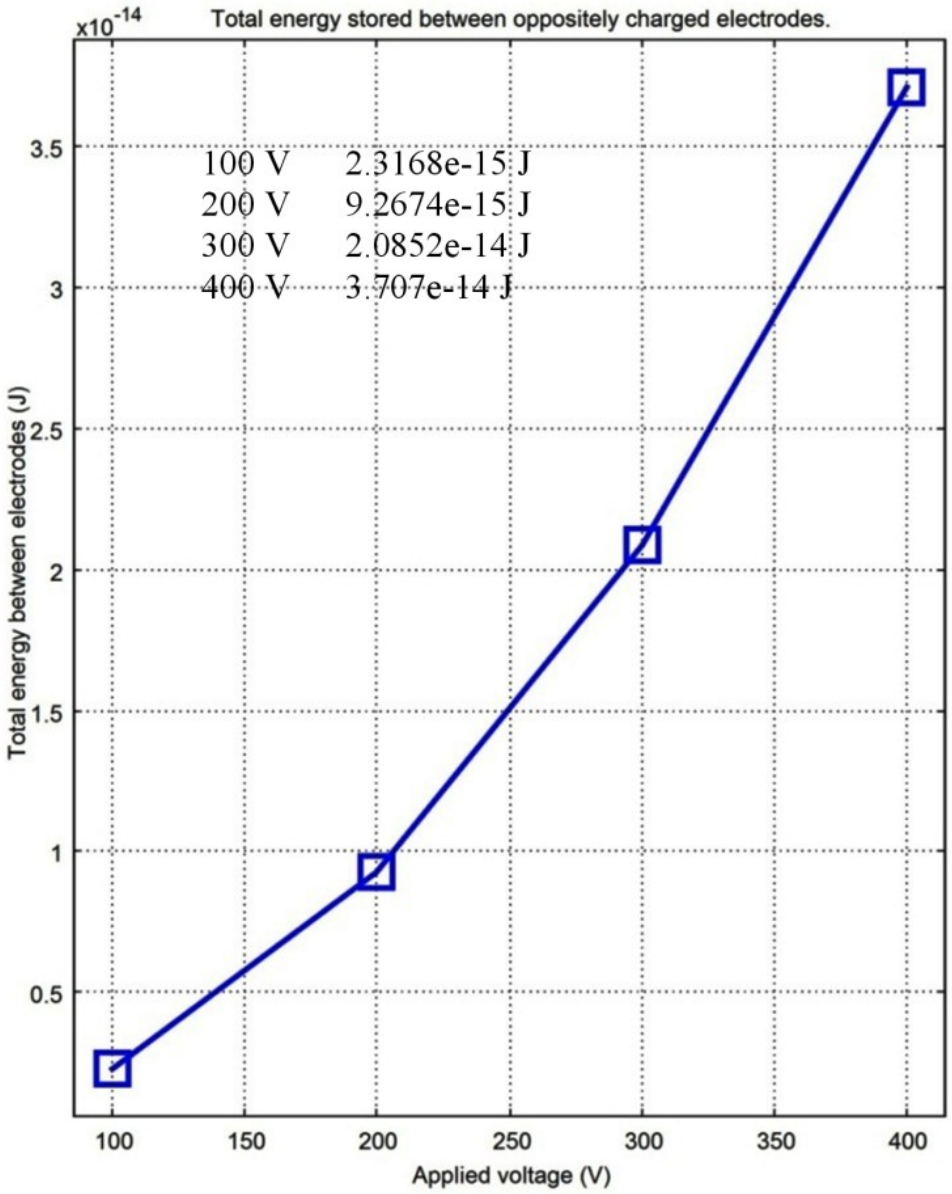
Total energy stored between oppositely charged electrodes.
x10^-14
100 V 2.3168e-15 J
200 V 9.2674e-15 J
300 V 2.0852e-14 J
400 V 3.707e-14 J
Total energy between electrodes (J)
Applied voltage (V)
0.5
1
1.5
2
2.5
3
3.5
100
150
200
250
300
350
400

a)

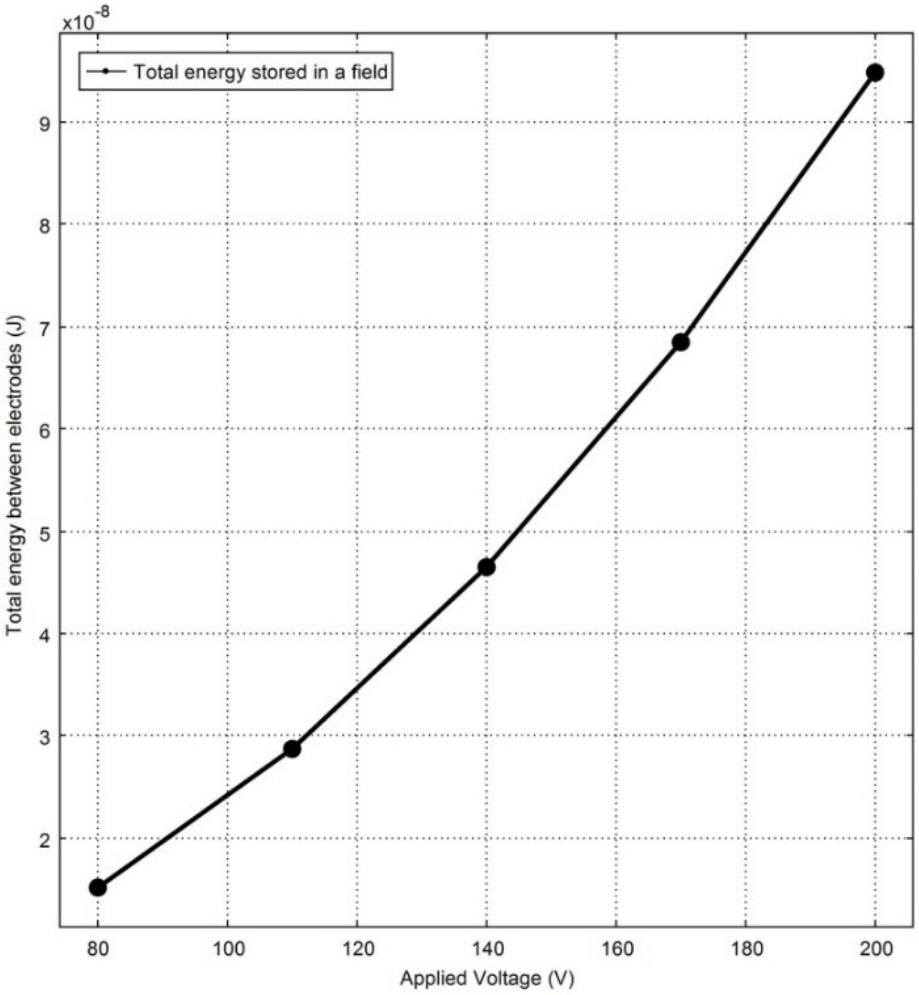
x10^-8
Total energy stored in a field
Total energy between electrodes (J)
Applied Voltage (V)
2
3
4
5
6
7
8
9
80
100
120
140
160
180
200

b)

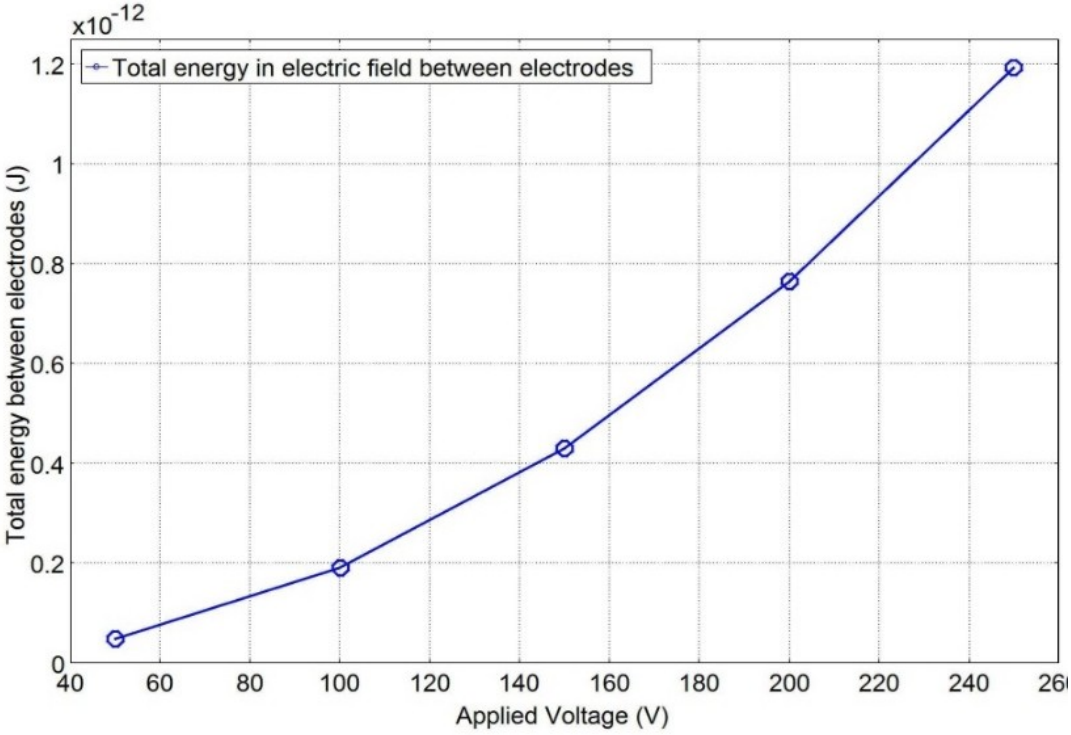

c)

Figure 5.15. a) Total energy stored in the field between oppositely charged plates of 3D GIS model with 1NW, b) total energy stored in a field between oppositely charged capacitive plates at different applied voltage in 2D GIS model, c) total energy stored in a field between oppositely charged plates versus the applied voltage in 3D GIS model with 9 NWs.

In fact, increase in the value of the applied voltage 4 times generated 16 times augmentation in the total energy in a gap between the oppositely charged capacitive plates in 3D model with one NW, as shown in Figure 5.15 (a). The obtained results illustrate a low amount of the work used to assemble a static charge distribution between the oppositely charged plates of the 2D GIS model (surface integral of the area between capacitive plates, 0.5*uy*uy*8.85e-12*9.16): $1.5166 \cdot 10^{-8}$ J at 80 V, 2.867210^{-8} J at 110 V, 4.644510^{-8} J at 140 V, 6.848210^{-8} J at 170 V, 9.478510^{-8} J at 200 V from Figure 5.15 (b).

However, the obtained values of total energy are much higher compared to the 3D model with 1 NW and 3D GIS model with 9 NWs. In the case of 3D GIS model with 9 NWs total energy stored between oppositely charged capacitive plates at a range of the applied voltages showed decreased values compared to 2D GIS model but higher values compared to 3D GIS model with 1 ZnO NW as illustrated in Figure 5.15 (c).

Finally, the dependence of the electric field on the space between nanowires was studied in 2D and 3D GIS models, and the results of the investigations are summarized in Figure 5.16.

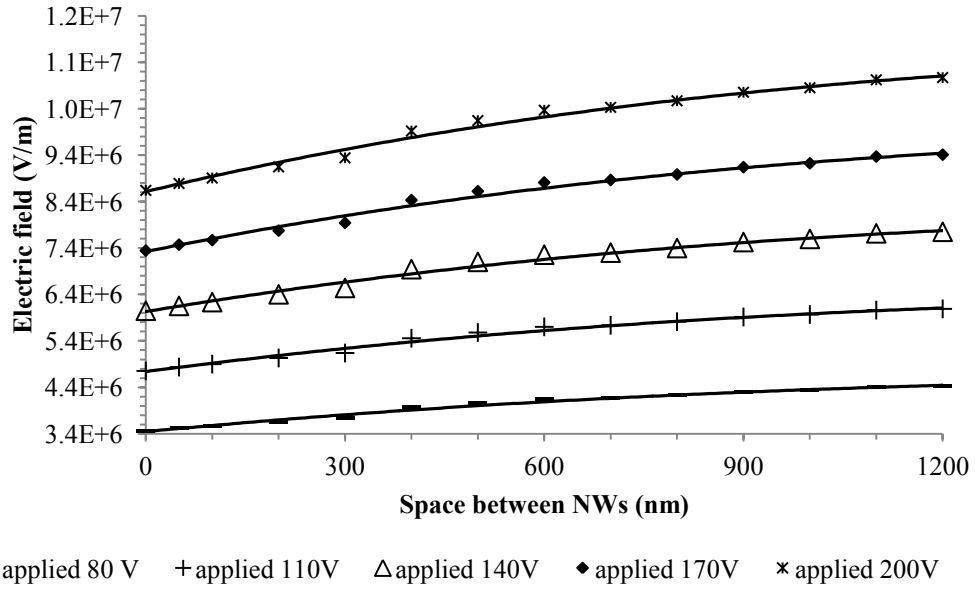

a)

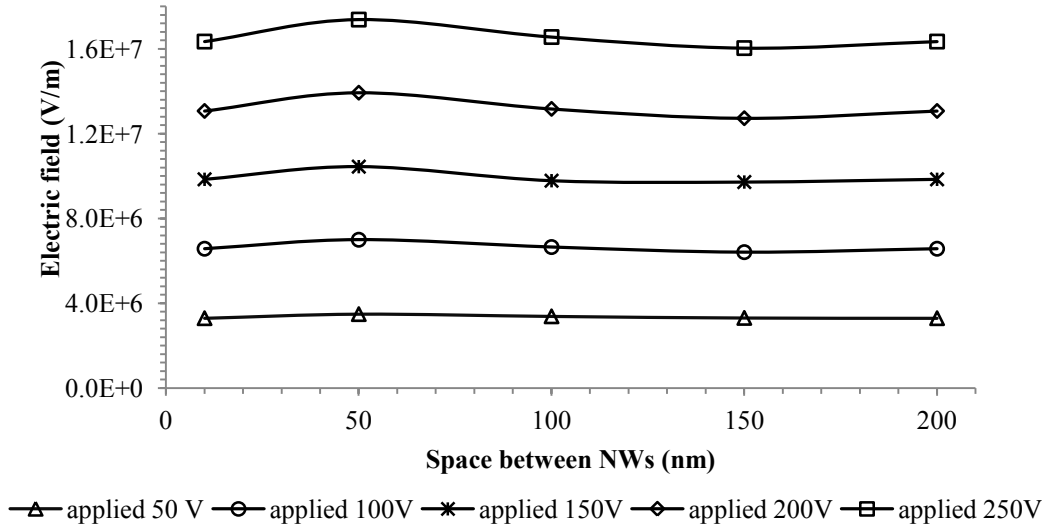

b)

Figure 5.16. a) Electric field versus the space between NWs at applied voltage from 80 V to 200V with step of 30 V in 2D model, b) electric field versus the space between NWs at applied voltage from 50 V to 250 V with step of 50 V in 3D model.

The obtained results of simulations illustrated the presence of the screening effect in 2D GIS model illustrated in Figure 5.16 (a). When ZnO NWs were situated close to each other, the maximum electric field was $8.64 \cdot 10^6$ V/m, but when space between nanowires increased to 9 NW lengths the value of the electric field was increased to $1.08 \cdot 10^7$ V/m at the applied voltage of 200V. Following investigation of the screening effect in 3D GIS model with 9 NWs demonstrated negligible differences in local electric field values, Figure 5.16 (b). Insignificant screening effect was observed because of the geometry of the NWs, the double increase in the values of the top and base NWs diameters compared to 2D GIS model.

COMSOL multiphysics has been used to optimize the physical dimensions of ZnO NWs and their distribution in an array for future incorporation into GIS. The simulations showed that not only screening effect is the dominant factor in decrease of the electric

field in the device but also the geometry of the nanowire plays a dominant role. It is illustrated that ZnO NWs with a large tips curvatures are advantageous, since they provide the highest electric fields in a vicinity of the NWs pinnacles. Another observation is that in contrast to NWs with the small diameters and insignificant tip curvatures the insignificant screening effect has been observed in 3D GIS model with NWs which have doubled diameters and increased apex curvatures. Total energy stored between capacitive plates of 3D GIS model with 9 NWs had higher values compared to 3D GIS model with 1 NW because of the increased amount of the field emitters, NWs. Optimized ZnO NWs have been achieved by the electrochemical synthesis, and gas ionization sensor has been fabricated with the optimized ZnO NWs integrated as anode/cathode.

5.3. Fabrication and Test Results of the GISs made with ZnO NWs

A gas ionization sensor (GIS) is a physical sensor based on the creation of the breakdown in the gaseous atmosphere between two oppositely charged capacitive plates. The applied electric fields in a GIS should be high enough to ionize the gas molecules which thus become the ionic current. However, high applied electric voltages in a range of kV units are required to create electric fields sufficient for gas ionization. Therefore, the performance of a gas detector operating this way is very low. With advances in the nanotechnology field, the possibility of placing nanostructured field emitters (nanowires) between two plates causes advances in a new generation of GIS devices [1, 47 - 56]. The field emitting nanowires create very high local electric field between the capacitive plates causing the enhancement of the total electric field and consequently lowering the breakdown voltages of the gases by several orders of magnitude. At micro/nano device

laboratories in ECE Department at Concordia University, as part of ongoing research to develop a sensitive odor sensor, several types of GIS-based metallic and semiconductor nanowires were designed, fabricated, and characterized. By using this technique it is managed to decrease the breakdown voltages of gases [1, 47 - 56] from several thousand to few hundred volts. However, it is the goal of this project to not only bring the breakdown voltage even lower but enhance other GIS properties in particular their durability. For this reason, we are using ZnO nanowires to replace the metallic nanowires in the GIS. As the ZnO has a very good chemical stability and withstands much higher electric field without damaging the apexes of the nanowires tips. Superior properties of ZnO nanowires make it possible to design and fabricate GIS devices with much lower breakdown voltages and enhanced durability of the devices. As discussed in previous chapters we can manipulate the morphology and conductivity of ZnO nanowires to achieve high electric fields, responsible for breakdown of gases. The design, fabrication and characterization of the GIS based on ZnO nanowires are discussed in this section.

5.3.1. Fabrication of GIS with Incorporated ZnO NWs

Structure of the GIS involves two capacitive electrodes. ZnO NWs are grown on one of the electrodes and placed between the plates, as shown in Figure 5.17.

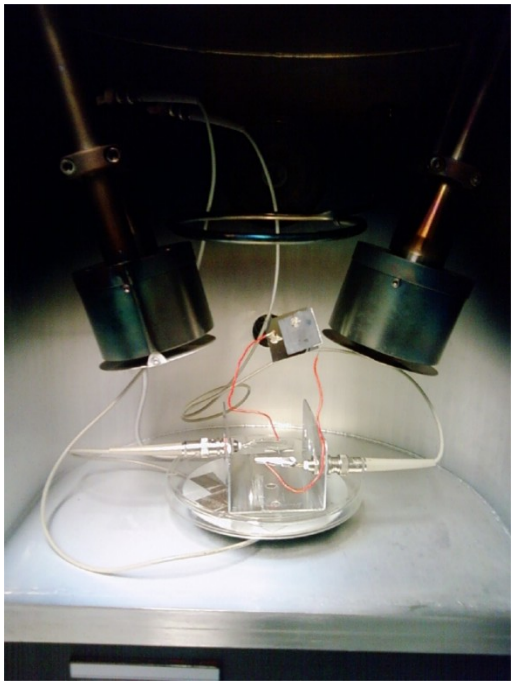

a)

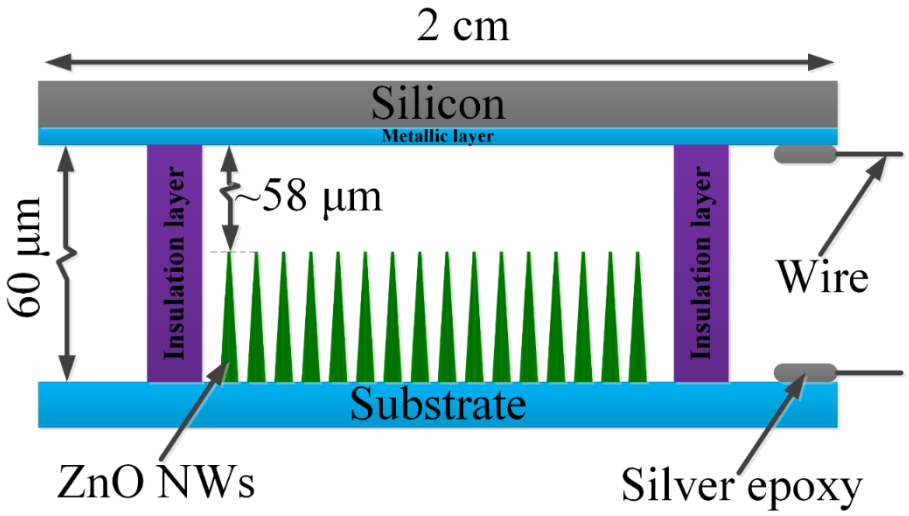
2 cm
Silicon
Metallic layer
60 µm
Insulation layer
~58 µm
Insulation layer
Wire
Substrate
ZnO NWs
Silver epoxy

b)

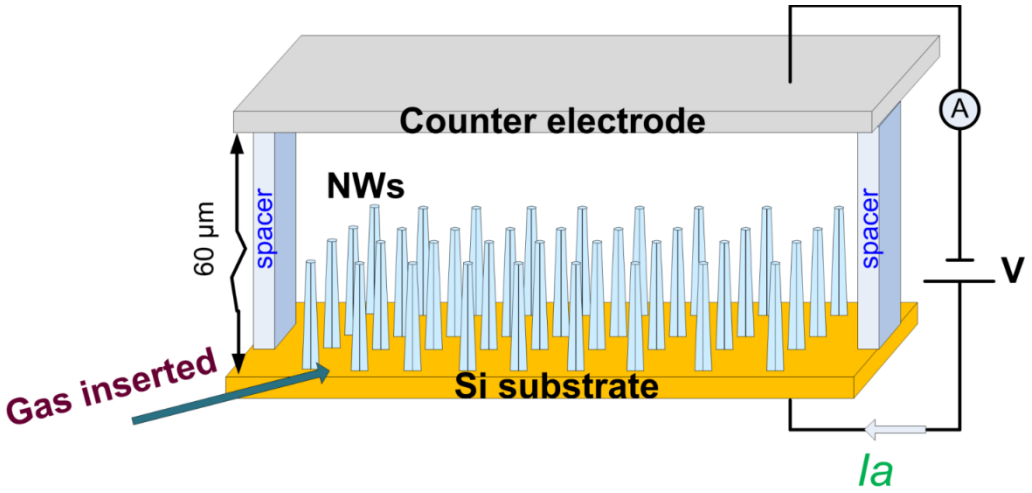

c)

Figure 5.17. a) GIS inside the chamber connected to the cables, b) 2D schematics of the GIS with the incorporated ZnO NWs, c) 3D schematics of the GIS with ZnO NWs as anode.

An insulating spacer, polypropylene ring with resistivity of 10^{16} -10^{18} Ω·cm and with thickness of 60 µm, is separating the two plates. Three openings in spacer were created each of them at angular distance 60° with the aim to let gas flow between the oppositely charged capacitive plates. Substrate with ZnO NWs, the insulation layer and its size, the opposite electrode, and the conductive wires connected to the measurement set up are demonstrated in Figure 5.17 (b). The two plates in this work are made of 2 x 2 cm^2 silicon wafers and the working area of the GIS was 346.36 mm^2. The backsides of the wafers are metalized to make them ohmic contacts. GIS electrodes with ZnO NWs were porous silicon (PS), n-type Si with high and low resistivity (ρ = 5-8 Ω·cm and ρ = 10^{-3} Ω·cm), and Au layer sputtered on n-type Si (gold layer was alloyed at 385°C for 45 min. in N_2/H_2 atmosphere (1:1)). Another electrode in GIS was the silicon covered by Al (metal was alloyed at 450°C for 30 minutes at N_2/H_2 atmosphere (1:1) with the intent to create the ohmic contact between Si and Al layer). Substrates covered by n-type and p-type ZnO NWs incorporated into GISs are illustrated in Figure 5.18.

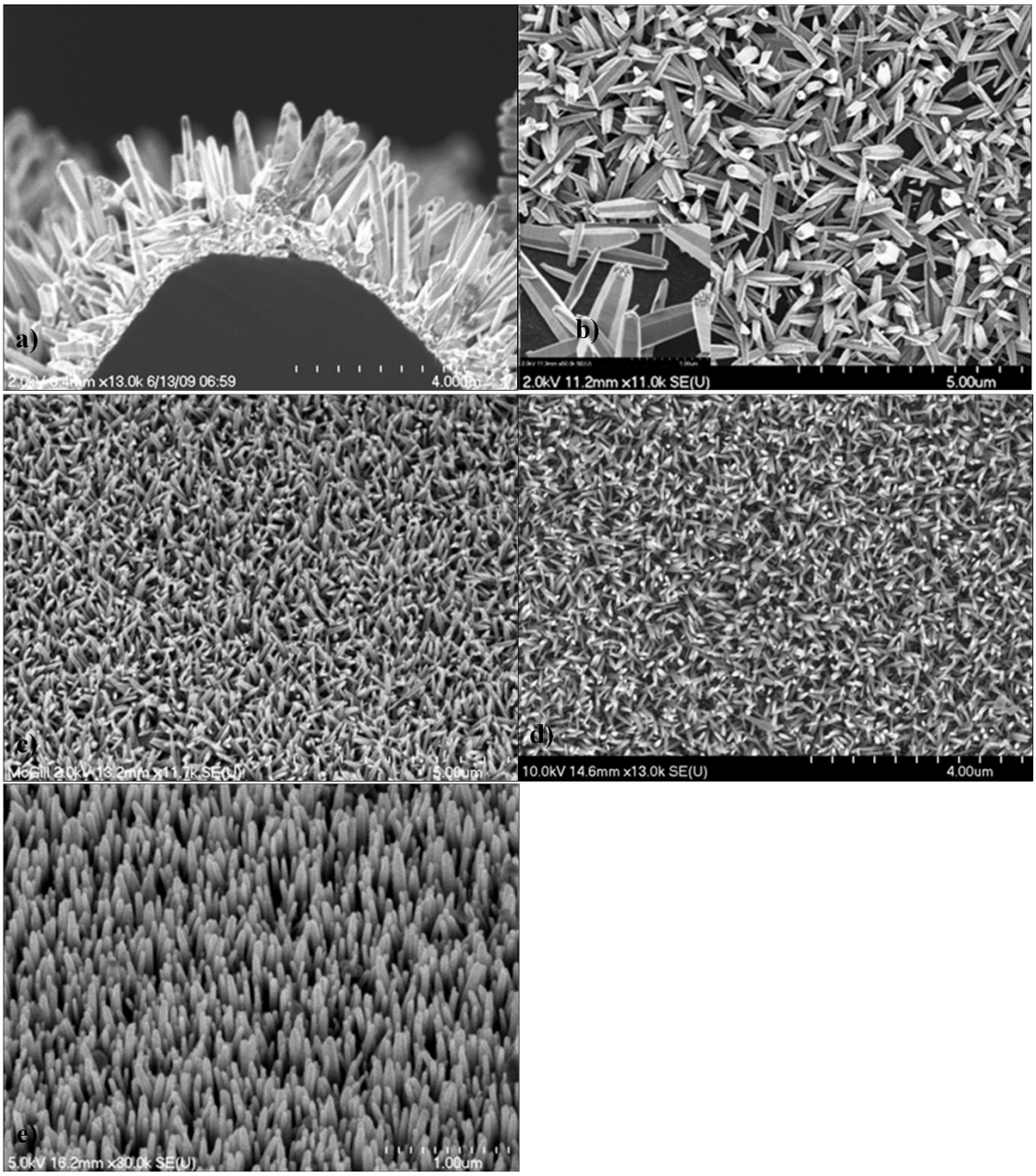

Figure 5.18. SEM images of ZnO NWs grown on a) the porous silicon and b) n^+-type Si ($\rho = 10^{-3}$ Ω·cm); SEM images of Ag-doped ZnO NWs grown on c) n-type Si (ρ = 5-8 Ω·cm), d) n^+-type Si, and e) gold layer (alloyed at 380°C for 45 minutes).

Porous silicon substrate with the grown perpendicular to the surface n-type ZnO NWs is illustrated in Figure 5.18 (a). Next, n-type ZnO NWs electrochemically grown on n^+-type

Si illustrates low distribution, random-angled, and with the nanoprotrusions on the NWs apexes. SEM images of the Ag-doped ZnO NWs grown on the n-type Si with low and high resistivity and on Au layer are shown in Figure 5.18 (c - e). The NWs tips' diameters were between 20 nm and 200 nm depending on their morphology.

Electrochemical growth parameters used to synthesize ZnO NWs are reported in Appendix A. EDXS analysis confirmed the uniform distribution of Ag inside ZnO NWs, and PEC cell measurements have illustrated p-type conductivity in Ag-doped ZnO NWs, as reported in Appendix A. The obtained n-type and p-type ZnO NWs electrochemically grown on the substrates with different conductivities were integrated into GISs.

The connection to Keithley-2400 single measurement units (SMUs) was achieved through connection of electrical wires attached to GIS to the cables on the handmade stand. The cables were connected inside the vacuum chamber to the outgoing triaxial cables connected to the SMUs, which were used to applied voltage sweeping in the range from 0 V to 400 V maximum and detected the created ionic currents and breakdown voltages in GISs [96]. The measurement set up and performances of the fabricated GISs are discussed in following section.

5.3.2. Gas Ionization Sensor Performance and Analysis

The fabricated gas ionization sensors were (1) tested in vacuum for different concentrations of gases, and (2) tested for detection of gas leakage in air. The measurement methodology and setup is described first. Then, the I-V characteristics, the breakdown voltages at different concentrations of gas and in different gases were studied. Finally, performance of the novel GISs was summarized.

5.3.2.a. Measurement Methodology and Setup

The goal of this investigation is to measure I-V characteristics of the gas ionization sensor, including the pre-breakdown current-voltage characteristics and the gaseous breakdown voltages measured for different gas types in a vacuum and in air.

Guarding was used to reduce a leakage current. Triax cables were employed for the low-current measurements. The core and the inner shield are kept at the same potential, and the leakage current between them was zero. The leakage current which appeared between inner and outer shields was neglected because the core was connected to the GIS and the current in the core was measured.

The input was a linear staircase voltage sweep. This sweep started from 0 V and ended at the maximum voltage (420 V). The programmable parameters (in the software provided with the Keithley 2400, having current resolution 10 pA), were the starting voltage, the end voltage, the voltage step levels, and the source delay at each step. The output changed in equal intervals until the stop source level was reached at the maximum voltage. The time duration at each step included the source delay (about 10 ns) and the time to perform the measurement (integration period). The time to perform measurement was determined by Number of Power Line Cycles (NPLC), which expressed the integration period by basing it on the line frequency. If it was set to 1 then the integration period was 1/60 s (for 60 Hz line power), and therefore it was equal to about 16.67 msec. The charging current was recorded at each voltage step. The damping time of the charging current was determined by the effective RC constant of the circuit. The capacitive current $I_{cap}(t)$ was given as [96]

$$I_{cap}(t) = I_0 \exp(-t/RC)$$
$$I_0 = C\Delta V / \Delta t \tag{5.23}$$

where t was elapsed time, I_0 was the peak of charging current, C was the cell capacitance, ΔV was the voltage step, and Δt was the pulse rise time. The value of the added delay time was high enough to have negligibly low value of the charging current in comparison to the real pre-breakdown currents. The schematic of the voltage sweep applied to GIS is illustrated in Figure 5.19.

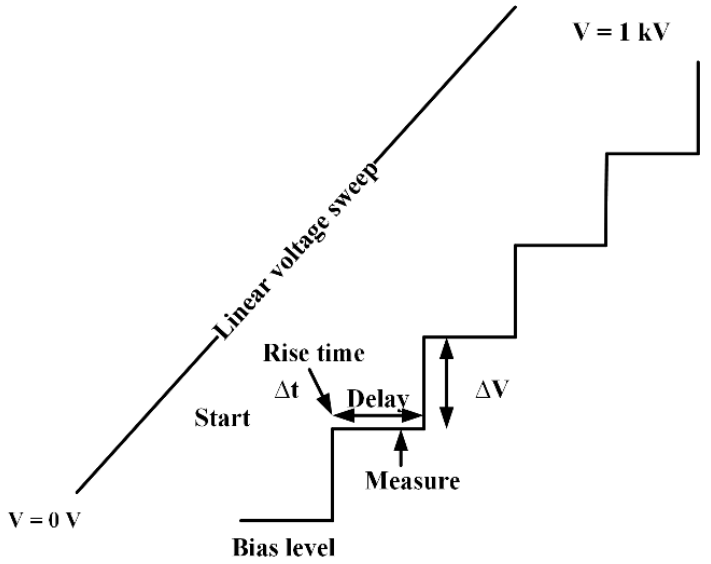

Figure 5.19. The input linear staircase voltage sweep used in the experimental testing of GISs.

The employed time delay value was 50 ms to ensure that I_{cap} dies off, and ΔV was less than 1 V.

5.3.2.b. Characterization of GISs

In this section the test results of fabricated GISs are reported. Gas ionization sensors were used in Field Ionization (FI) and Field Emission (FE) modes, meaning that ZnO NWs were applied as anode or as cathode, respectively.

First, the sensitivity of the novel sensors was studied by detecting argon in a vacuum. The studies of variations in breakdown voltages in FE and FI modes were reported. It was expected that in GISs with n-type ZnO NWs the low values of the breakdown voltages should be detected in FE mode because of high amount of electrons available above Fermi energy level. In contrast, GISs with p-type ZnO NWs should generate low breakdowns in FI mode because of the high concentration of holes available to accept gas electrons at energy levels lower than Fermi energy level. In both cases the electrons emitting from the nanowires (FE mode) and gas electrons (FI mode) would tunnel through a short distance at small energy lost. Experimental results of the breakdown voltages at low concentrations of Ar using fabricated GISs with n-type or p-type ZnO NWs are illustrated in Figure 5.20.

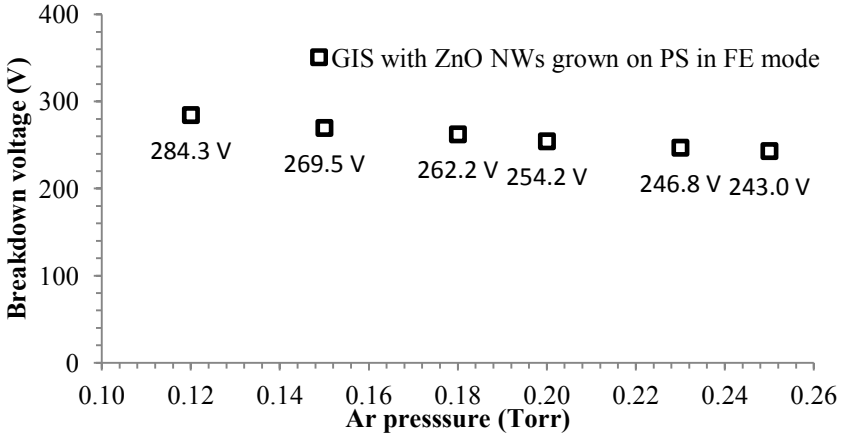

a)

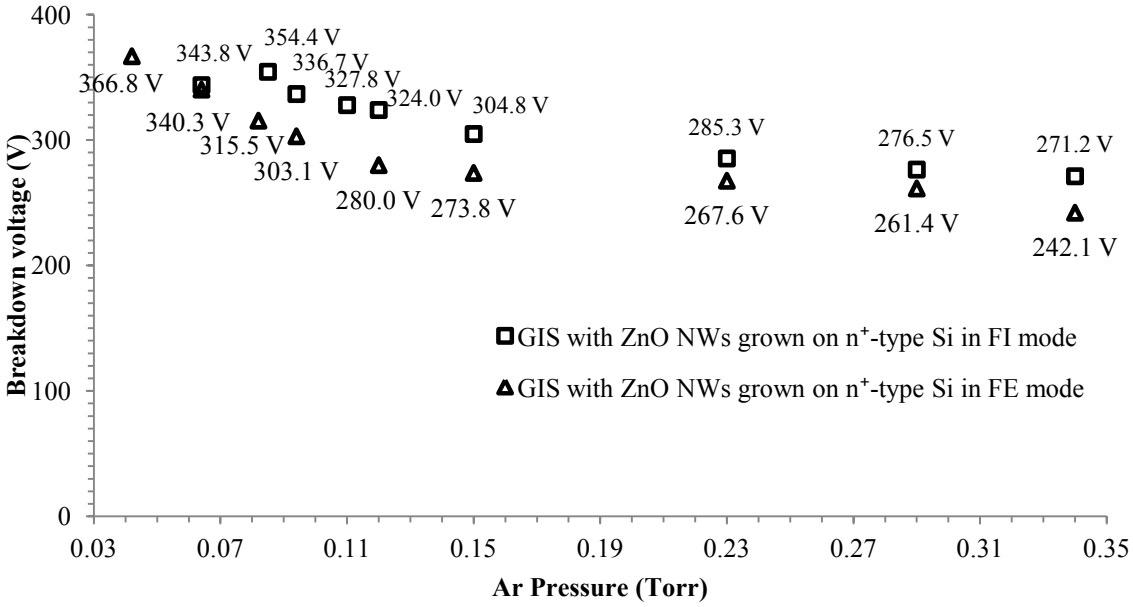
400
300
200
100
0
Breakdown voltage (V)
0.03
0.07
0.11
0.15
0.19
0.23
0.27
0.31
0.35
Ar Pressure (Torr)
366.8 V
343.8 V
354.4 V
336.7 V
327.8 V
324.0 V
304.8 V
340.3 V
315.5 V
303.1 V
280.0 V
273.8 V
285.3 V
267.6 V
276.5 V
261.4 V
271.2 V
242.1 V
GIS with ZnO NWs grown on n+-type Si in FI mode
GIS with ZnO NWs grown on n+-type Si in FE mode

b)

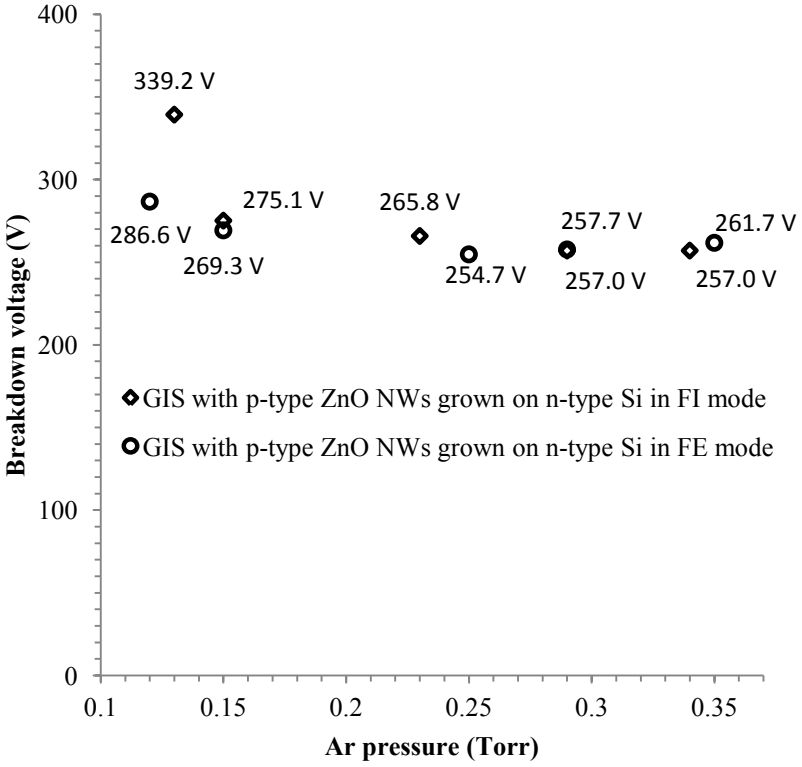
400
300
200
100
0
Breakdown voltage (V)
0.1
0.15
0.2
0.25
0.3
0.35
Ar pressure (Torr)
339.2 V
286.6 V
275.1 V
269.3 V
265.8 V
254.7 V
257.7 V
257.0 V
261.7 V
257.0 V
GIS with p-type ZnO NWs grown on n-type Si in FI mode
GIS with p-type ZnO NWs grown on n-type Si in FE mode

c)

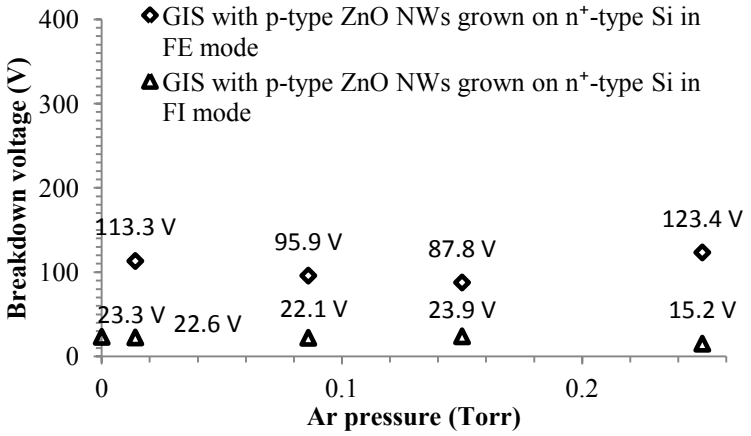

d)

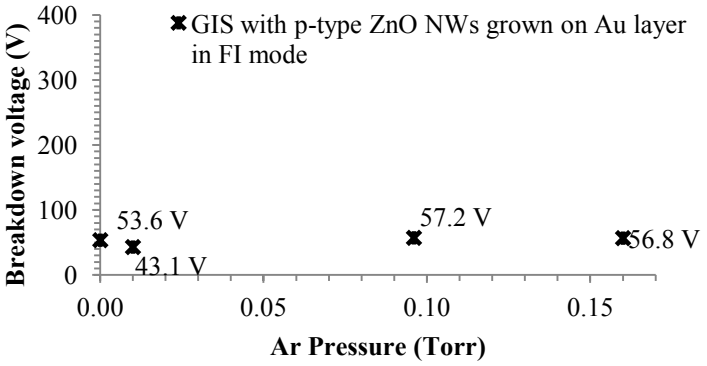

e)

Figure 5.20. Breakdown voltage versus Ar pressure is detected by using a) GIS with n-type ZnO NWs grown on PS in FE mode, b) GIS with n-type ZnO NWs grown on n^+-type Si in FE and FI modes, c) GIS with p-type ZnO NWs grown on n-type Si in FE and FI modes, d) GIS with p-type ZnO NWs grown on n^+-type Si in FE and FI modes, and e) GIS with p-type ZnO NWs grown on Au layer in FI mode.

The values of the breakdown voltage versus the Ar concentration illustrated behavior similar to the Paschen's curve in terms of the decreasing of breakdown voltage with increasing in the gas concentration as shown in Figure 5.20 (a – c). The observed degraded performance of GIS with ZnO NWs grown on n^+-type Si was attributable to the low amount of the electric field emitters contributing to the production of the high electric fields, as shown in Figure 5.20 (b). Since, most of the nanowires have been grown under angle to the substrate and have low density. Also, this GIS was tested in FE

and FI modes illustrating decreased values of the breakdowns in FE mode compared to the FI mode voltages. The small difference in values of breakdown voltages in FE and FI modes illustrate existence of the high amount of surface states in ZnO NWs. Next GIS with p-type ZnO NWs grown on n-type Si illustrates almost the same breakdowns in FE and FI modes for the same reason as in previous gas detector, Figure 5.20 (c). The performance of this GIS was low because of the high voltage drop on the resistive substrate ($\rho \approx 5\ \Omega\cdot$cm created resistance of 100 Ω for wafer thickness of 500 μm) compared to previously observed GISs, where resistivity of the substrates was $10^{-3}\ \Omega\cdot$cm, which created resistance of 0.5 Ω for the same Si wafer thickness. The decreased resistivity of the substrate in the subsequent GIS, where p-type ZnO NWs were grown on n^+-type Si, illustrated the lowest breakdown voltages in FI and FE modes compared to other GISs, Figure 5.20 (d). Well defined difference between breakdowns in FE and FI modes was observed. The lower breakdown voltages were in FI mode since p-type ZnO NWs were employed. Lastly, GIS with p-type ZnO NWs grown on Au layer was used in FI mode only, because p-type nanoemitters provide superior performance in this mode. This gas detector has illustrated slightly lower performance compared to the previously discussed GIS because of the degraded at some extend geometry of the NWs, Figure 5.20 (e). As it can be seen the uniform distribution, geometrical shape of ZnO NWs apexes, and an adequate doping level of field emitters greatly improved the performance of GIS. In addition, the nanoprotrusions on NWs pinnacles significantly improved local electric field and the area of the ionization. From the above investigation on detection of Ar at low pressures, the last two gas detectors were chosen for detection of nitrogen, argon, oxygen, and helium in an air and in a vacuum.

At start, detection of gases was performed by GIS with p-type ZnO NWs grown on n^+-type Si. The compliance of the current was chosen 100 mA. Gas flow into an air was regulated by mass flow controller. The applied flow (120 units) contributed to about 0.1 Torr of Ar pressure at constant mechanical pump work, which corresponds to Ar gas density (ρ) of 0.213 g/m^3 (ρ=(P(in Pa)M)/(RT), where ideal gas constant (R) is 8.314 J/(K·mol), molar mass of Ar (M) is 39.948 g/mol, and room temperature (T) is 300 K). In these tests the vacuum chamber was open and flow of gas into air was detected by GIS. I-V characteristics of GIS for detection of the gas leakage into an air are illustrated in Figure 5.21.

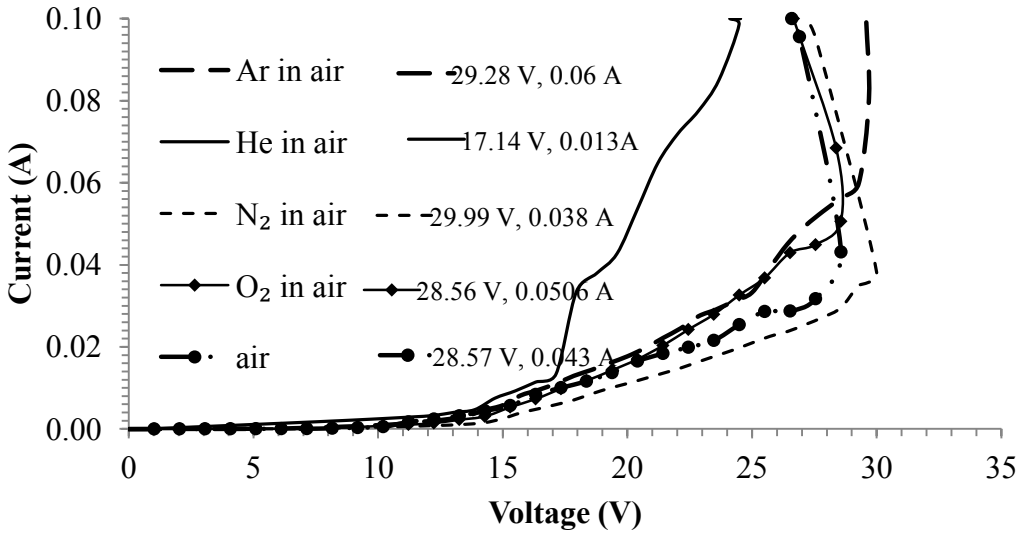

Figure 5.21. I-V characteristic of GIS with p-type ZnO NWs grown on n^+-type Si in FI mode for detection of gas traces in an air.

The obtained results illustrated that the breakdowns in GIS happened at high ionic currents, more than 0.01 A, Figure 5.21. The smallest value of the voltage in field-limited regime in GIS was at leakage of He, and it was 17.14 V at generated ionic current of 13.4 mA, because of the longest free mean path due to small ionic radius of He compared to

the other gases free mean paths. Breakdown voltages in leak of the oxygen (28.56 V), argon (29.28 V), and nitrogen (29.99 V) in an air were very close to the breakdown in an air (28.57 V). The air and N_2 follow a similar curve where air has slightly lower breakdown compared to N_2. The reason is that air is a mixture of gases where nitrogen is the dominant gas, 78%. The generated current at breakdowns in air (43 mA), in air with the trace of oxygen (50.6 mA), and in the air with the argon (60 mA) varied from each other for about 10 mA. The generated breakdown current in air with trace of nitrogen (38 mA) had only minor difference from generated current in air (43 mA). In summary, investigation on the detection of gas escape in an air has shown that fabricated sensor can be applied as gas leakage detector of He based on the distinguished breakdown voltage (17.14 V) which is different from breakdown in air (28.57 V), or gas leakage detector of O_2 and Ar based on variations in generated current at breakdowns.

Following the detection of different concentration of gases in vacuum using the same GIS was disclosed. Different concentrations of gas was introduced into vacuum chamber under vacuum (10^{-5} Torr), and experimental data on GIS performance was obtained. The first gas, which has been assessed by GIS, was Ar, as shown in Figure 5.22.

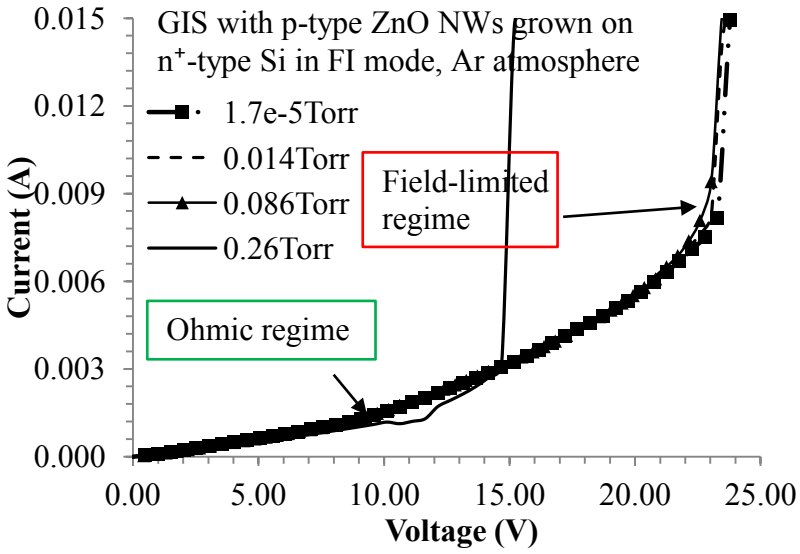
GIS with p-type ZnO NWs grown on
n+-type Si in FI mode, Ar atmosphere
1.7e-5Torr
0.014Torr
0.086Torr
0.26Torr
Field-limited regime
Ohmic regime
Current (A)
Voltage (V)
0.015
0.012
0.009
0.006
0.003
0.000
0.00
5.00
10.00
15.00
20.00
25.00

a)

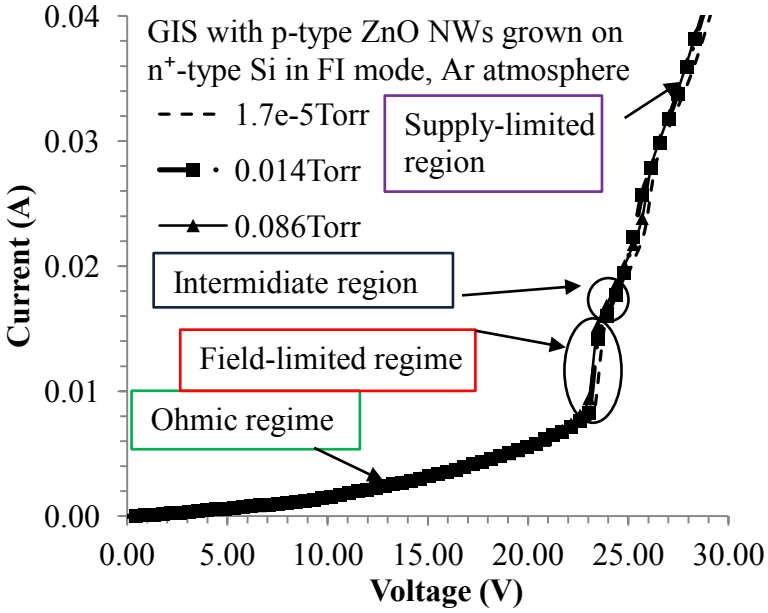
GIS with p-type ZnO NWs grown on
n+-type Si in FI mode, Ar atmosphere
1.7e-5Torr
0.014Torr
0.086Torr
Supply-limited region
Intermidiate region
Field-limited regime
Ohmic regime
Current (A)
Voltage (V)
0.04
0.03
0.02
0.01
0.00
0.00
5.00
10.00
15.00
20.00
25.00
30.00

b)

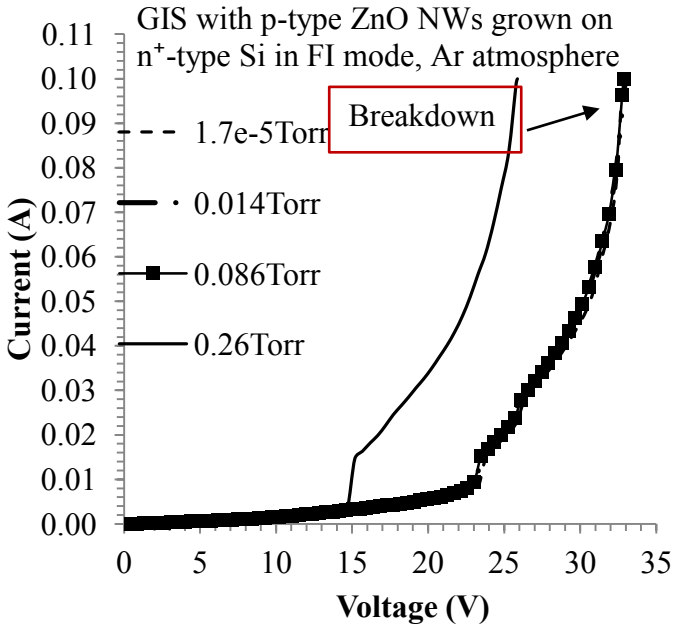

c)

Figure 5.22. I-V characteristics of GIS with p-type ZnO NWs grown on n^+-type Si in FI mode for detection of different concentrations of Ar gas in vacuum (a - c).

The curves illustrate four regions in Figure 5.22. Ohmic region where field strength is small and current flows because of the existing radiation-generated electron-ion pairs as $I=eE\mu_p p$ where concentration of the gas ions is negligible. Next region represents beginning of the ionization in the field-limited regime. The sharp increasing of the current is observed in this region similar to the theoretical current, as illustrated in Figure 5.7. Field-limited current increases with electric field intensity and depends on gas ionization energy. This regime is followed by the intermediate region where the increasing of voltage and current is observed because of the rebound to the tips gas particles exceeding the polarization energy, as indicated in Figure 5.22 (b). Thus, gas molecules are approaching to the ionization region only from the gas region, and the arrival rate begins to be proportional to the supply function as in Equation (5.13). So, current reaches supply-limited ionization regime. It starts to depend on supply function

and polarizability of the gas, and illustrates Ohmic behavior similar as in theoretical curve of Figure 5.8. Finally, breakdown is observed at higher ionic currents, as illustrated in Figure 5.22 (c). Also, the variation of the breakdown voltage in GIS with the amount of Ar gas was observed. At small amount of gas, $1.7 \cdot 10^{-5}$ Torr, the breakdown voltage was the largest one (23.3 V), as shown in Figure 5.22. The tests of GIS on detection of different concentrations of He, N_2, and O_2 are shown in Figure 5.23.

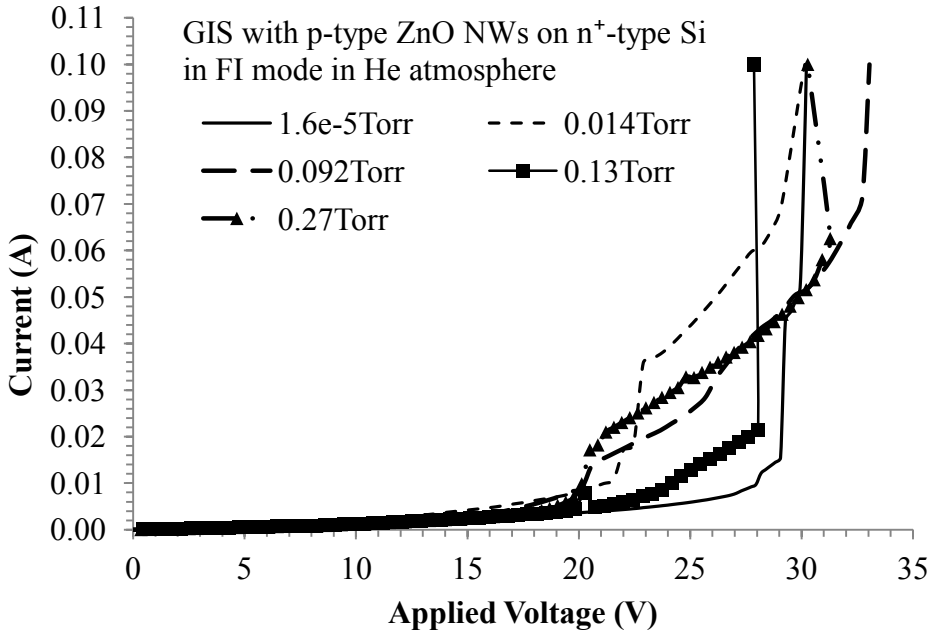

a)

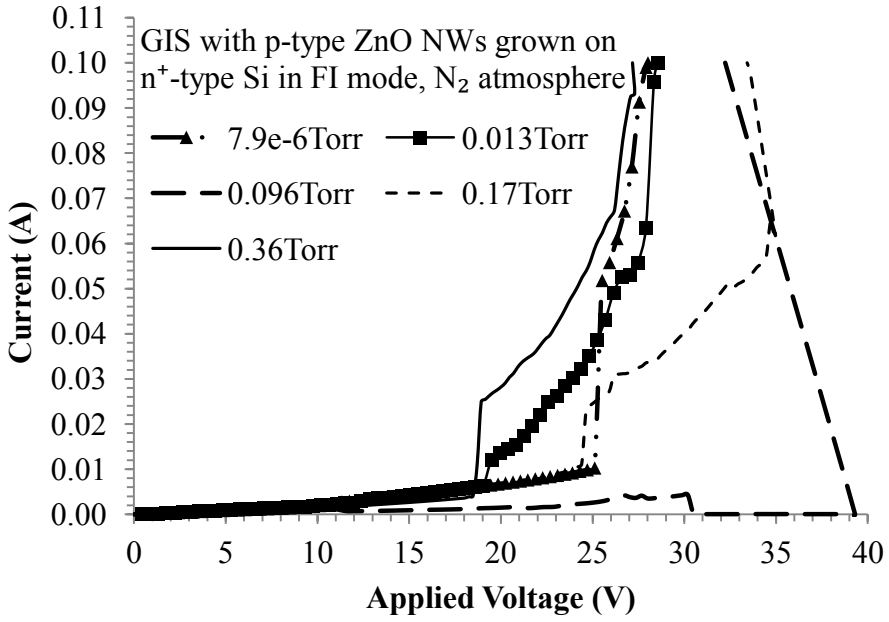

b)

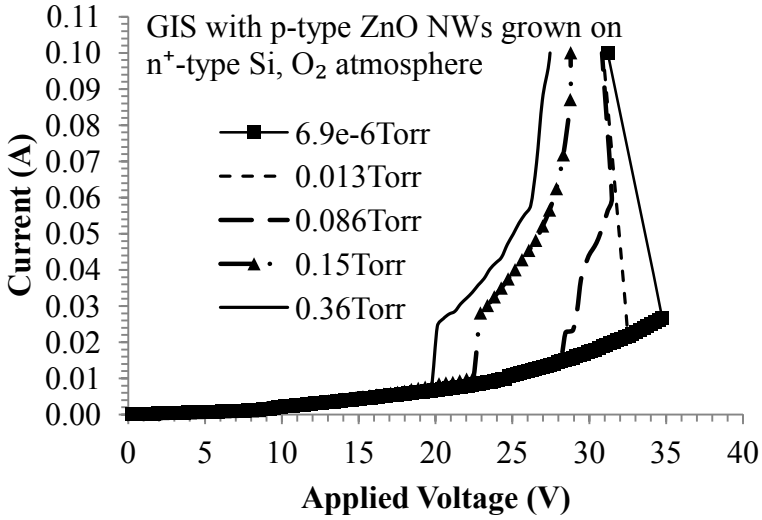

c)

Figure 5.23. I-V characteristics of GIS with p-type ZnO NWs grown on n^+-type Si in FI mode for detection of different concentrations of He in vacuum (a), I-V characteristics of GIS with p-type ZnO NWs grown on n^+-type Si in FI mode for detection of different concentrations of N_2 in vacuum (b), I-V characteristics of GIS with p-type ZnO NWs grown on n^+-type Si in FI mode for detection of different concentrations of O_2 in vacuum (c).

I-V characteristics of the device in different concentrations of He illustrates that the breakdown voltage at different concentrations of He gives similar values, as Figure 5.23

(a) indicates. The negative differential resistivity was observed at 0.13 Torr when current was going from Ohmic regime into field-limited region because of the increase in the ion-electron recombination rate at non-uniform electric fields at the nanowires tips at constant generation rate. The breakdown voltages in field-limited region are used to detect the gas or its concentration since current depends on the gas concentration and gas ionization energy. After tests in He GIS with p-type ZnO NWs grown on n^+-type Si was employed to detect different concentrations of N_2. The lowest voltage was 18 V at 0.36 Torr in field-limited region and breakdown voltage was 23.3 V, and the maximum voltage was 39.5 V at 0.096 Torr in field-limited region and the maximum breakdown voltage was 33.6 V at 0.17 Torr, Figure 5.23 (b). Negative differential resistivity regions over certain ranges were observed in I-V curve at N_2 gas pressure 0.096 Torr. The first region with negative resistivity is at 11 V after Ohmic region. This is attributable to the increase in the ion-electron recombination rate at non-uniform electric fields at the nanowires tips at constant generation rate. Then a quasi-exponential current rise is starting at 12 V. Repeated negative differential resistivity regions were observed at 19.8 V, 26.4 V, and 29.55 V. Also, the decreasing voltage was observed in ionic current at 0.096 Torr. This is a manifestation of the corona discharge. The observed I-V characteristics of GIS in O_2 atmosphere illustrated as in previous cases after the breakdown further increasing in current resulted in decreased voltage or in other words in corona discharge, as shown in Figure 5.23 (c). The summary of the breakdowns in different gases in GIS with p-type ZnO NWs grown on n^+-type Si is reported in Figure 5.24.

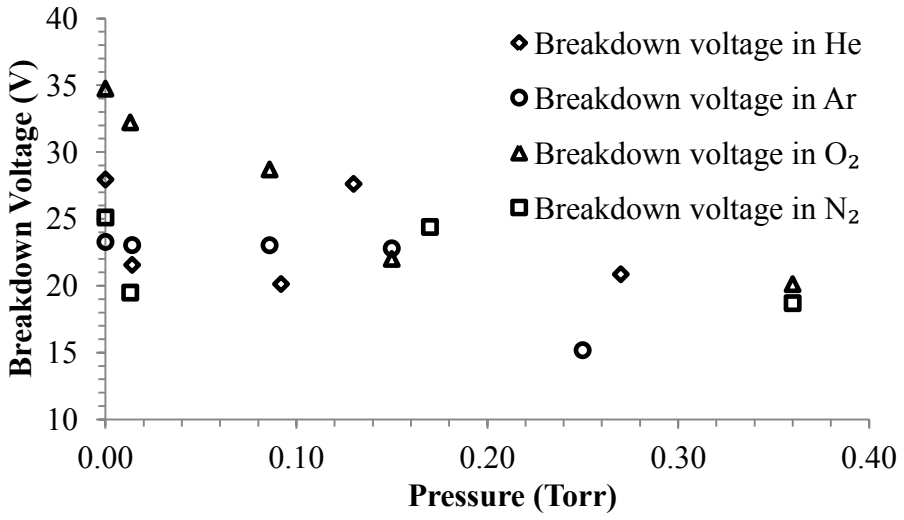

Figure 5.24. Breakdown voltages versus gas concentrations.

The breakdown voltages in different types of gases versus varying gas concentrations have illustrated that breakdown voltage in Ar gas had lowest value compared to the others gases at low pressures as around 10^{-5} Torr following by breakdown in N_2, in He, and in O_2, Figure 5.24. The breakdown voltages in oxygen illustrated pronounced decrease in their values with increased concentration of the gas as in Paschen's curve. Experimental data provide distinguishable breakdown voltages in field-limited regions in different gaseous atmosphere. Ohmic current can be employed to detect gases because the gas conductivity ($eE\mu_i n_i$) is different for each gas. At applied bias voltages of 1 V and 5 V the ionic current in Ar, He, O_2, and N_2 at 0.01 Torr was measured, Figure 5.25.

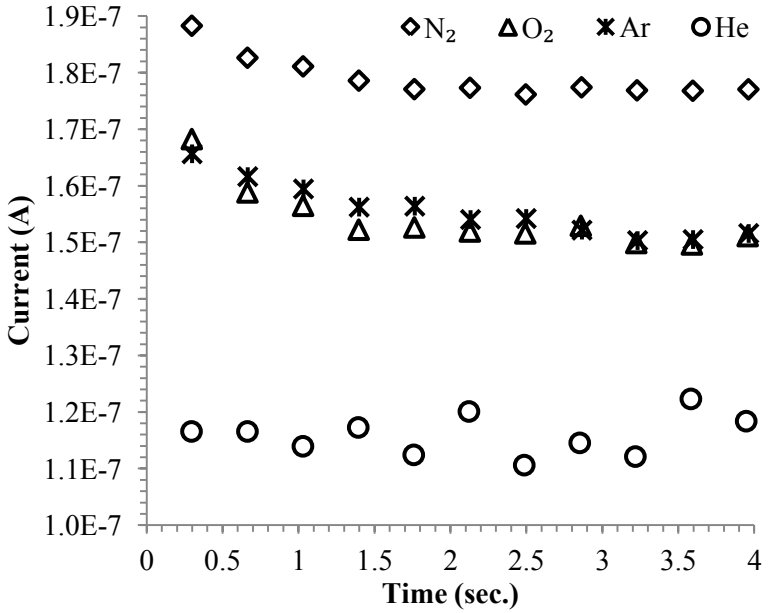

a)

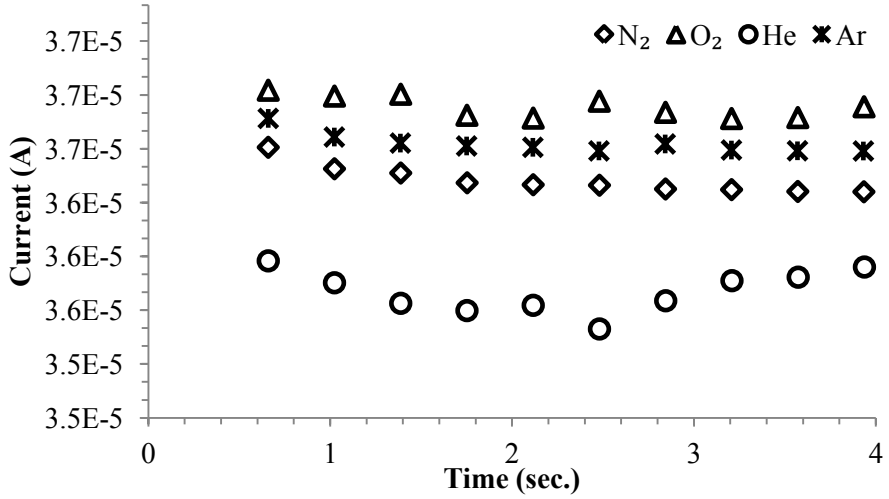

b)

Figure 5.25. Ionic current generated in Ar, He, N_2, O_2 at 0.01 Torr versus time in GIS with p-type ZnO NWs grown on n^+-type Si when constant voltage was applied: a) 1 V, b) 5 V.

The results of the tests illustrated that GIS sensor was capable to detect gases based on the generated ionic current from the 1 V or 5 V batteries, Figure 5.25. At applied 1V ionic current created in argon and oxygen were almost the same 0.152 μA, and formed

current in nitrogen was the highest one, 0.178 μA, as shown in Figure 5.25 (a). Also, the lowest currents were generated in He gaseous atmosphere such as 0.116 μA and 35.8 μA at applied 1 V and 5 V, respectively. Values of the generated currents at 5 V bias were hundreds times higher compared to formed ionic currents at 1 V bias, as indicated in Figure 5.25 (b). Moreover, ionic currents produced in oxygen, in argon, and in nitrogen at bias of 5 V were 36.7 μA, 36.6 μA, and 36.4 μA, respectively.

Next GIS with p-type ZnO NWs grown on Au layer was used to detect gases in a vacuum in FI mode. The compliance of the current was 1 μA. First, I-V characteristics of GIS with p-type ZnO NWs grown on Au layer were recorded in Figure 5.26.

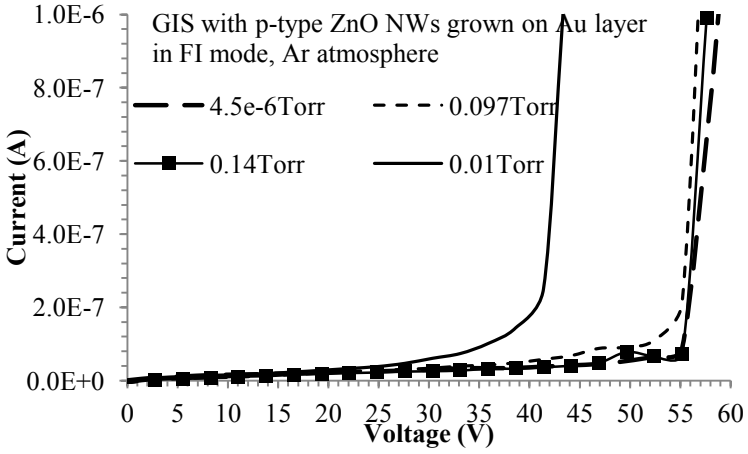

a)

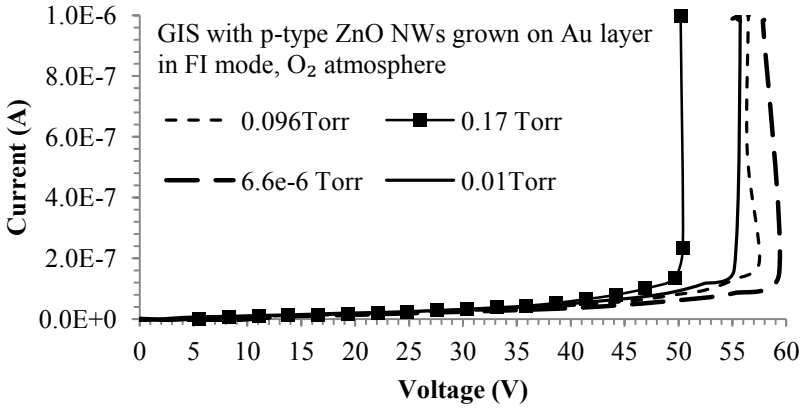
GIS with p-type ZnO NWs grown on Au layer in FI mode, O_2 atmosphere
0.096Torr
0.17 Torr
6.6e-6 Torr
0.01Torr
Current (A)
1.0E-6
8.0E-7
6.0E-7
4.0E-7
2.0E-7
0.0E+0
0 5 10 15 20 25 30 35 40 45 50 55 60
Voltage (V)

b)

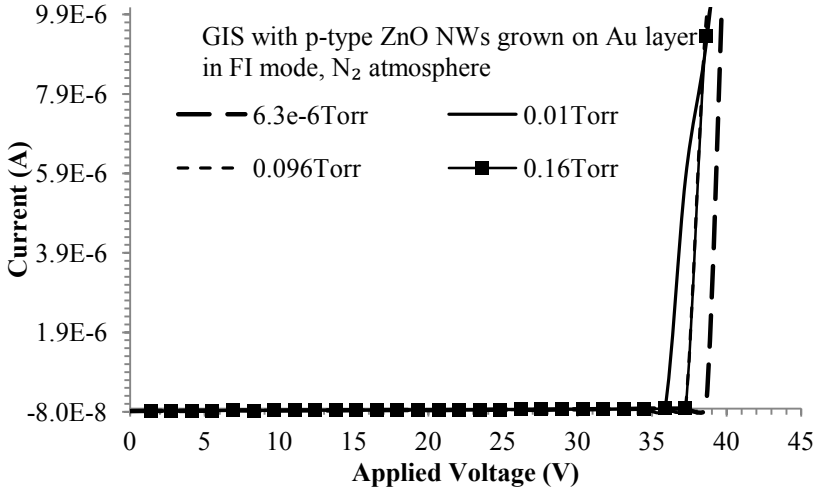
GIS with p-type ZnO NWs grown on Au layer in FI mode, N_2 atmosphere
6.3e-6Torr
0.01Torr
0.096Torr
0.16Torr
Current (A)
9.9E-6
7.9E-6
5.9E-6
3.9E-6
1.9E-6
-8.0E-8
0 5 10 15 20 25 30 35 40 45
Applied Voltage (V)

c)

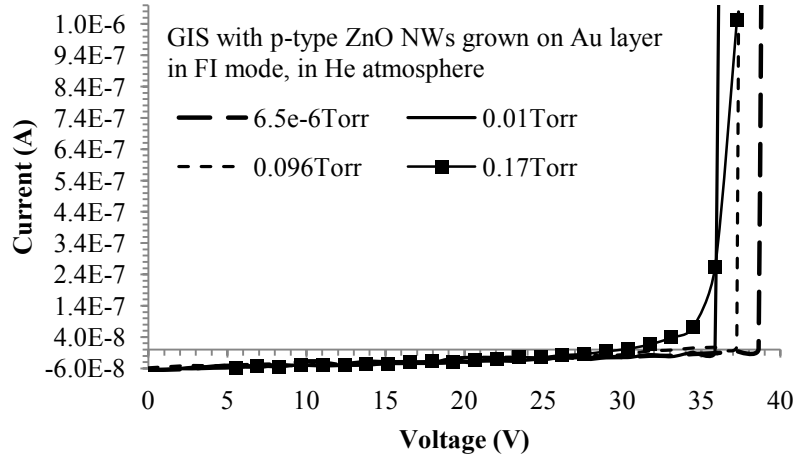
GIS with p-type ZnO NWs grown on Au layer in FI mode, in He atmosphere
6.5e-6Torr
0.01Torr
0.096Torr
0.17Torr
Current (A)
1.0E-6
9.4E-7
8.4E-7
7.4E-7
6.4E-7
5.4E-7
4.4E-7
3.4E-7
2.4E-7
1.4E-7
4.0E-8
-6.0E-8
0 5 10 15 20 25 30 35 40
Voltage (V)

d)

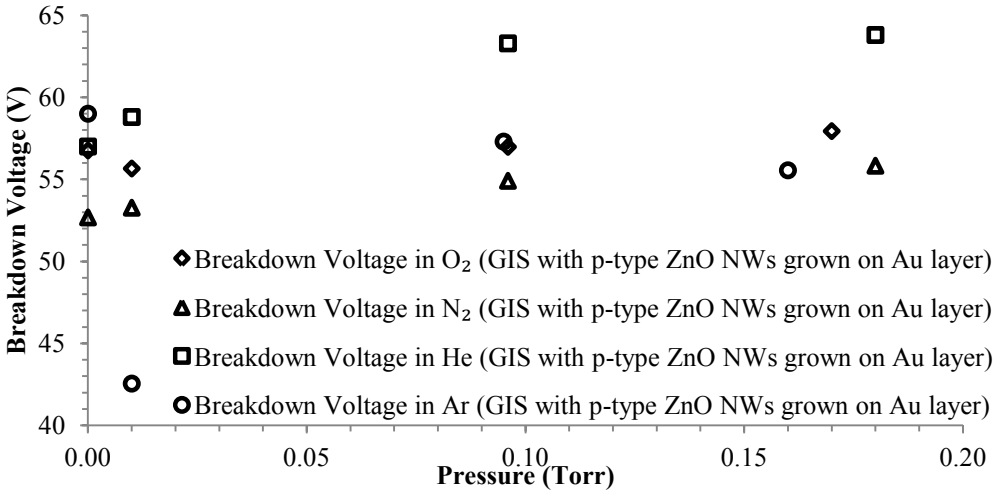

e)

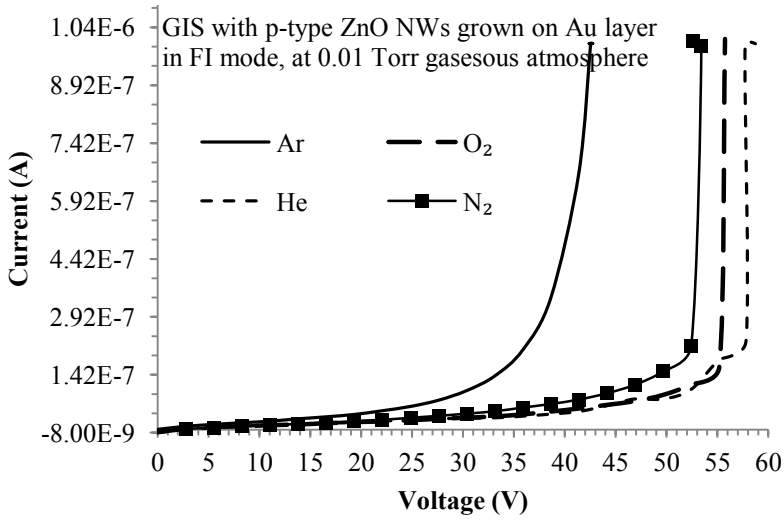

f)

Figure 5.26. I-V characteristic of GIS with p-type ZnO NWs grown on Au layer in FI mode: a) detection of different concentrations of Ar, b) detection of different concentrations of O_2, c) detection of different concentrations of N_2, d) detection of different concentrations of He, e) breakdown voltages in GIS with p-type ZnO NWs grown on Au layer versus gas concentrations of Ar, He, O_2, N_2, f) I-V characteristics of GIS with p-type ZnO NWs grown on Au layer in FI mode in 0.01 Torr gaseous atmosphere in Ar, O_2, N_2, and He.

The breakdowns in all gases in field-limited regime were detected at low gas concentrations in all studied gases as shown in Figure 5.26. The distinguishable values of

the voltage in different gases and different concentrations were observed in each gas. Following graph illustrates the voltages generated by GIS with p-type ZnO NWs grown on Au layer at different gas. Well defined distinguishable breakdown voltages can be observed at pressure of 0.01 Torr. The breakdowns in N_2 and O_2 had no variations because of the increasing gas pressure. But they have distinct values from each other. Ar illustrated minimum breakdown at 0.01 Torr following by increasing of the breakdown voltages with gas pressure. I-V characteristics of the investigated GIS with p-type ZnO NWs grown on Au layer in different gases at constant pressure of 0.01 Torr was investigated next. I-V characteristic for different gas generated distinct curves in field-limited regime at constant pressure of 0.01 Torr.

Further experimentation used ohmic current to detect different gases at applied biases of 5 V and 10 V. The average value of the generated ionic current at constant gas pressure 0.01 Torr is reported in Table 5.5.

Table 5.5. Field-limited current values detected in GIS with p-type ZnO NWs grown on Au layer at applied bias voltages of 5 V and 10 V at constant gas pressures of 0.01Torr.

Gas	Ar		O_2		He		N_2	
Bias voltage [V]	5	10	5	10	5	10	5	10
Current [nA]	6.81	14.7	5.14	10.6	5.57	12	5.67	11.1

The results illustrate the similarities in prebreakdown region. For bias voltage 5V current was 5.14 nA, 5.57 nA, 5.67 nA, and 6.81 nA for O_2, He, N_2, and Ar, respectively, and for bias voltage 10 V current was 10.6 nA, 11.1 nA, 12 nA, and 14.7 nA for O_2, N_2, He, and Ar, respectively. The highest current was created in Ar, and the lowest current was formed in O_2. Also, the values of the generated ionic currents in He and in N_2 switched the order when bias voltage was increased to 10 V as shown in Table 5.5. GIS with p-

type ZnO NWs grown on Au layer has demonstrated improved performance, good selectivity and repeatability.

In FE mode the GISs under investigation in some cases had slight decrease in voltage with increase of current in I-V curves. This is a manifestation of the corona discharge. Townsend avalanche phenomena was observed at currents 10^{-7} A to 10^{-6} A. To estimate field enhancement factor in GIS with p-type ZnO NWs grown on Au layer we used the slope in the linear region of the generated dark discharge current at vacuum condition (P = $1.8 \cdot 10^{-5}$ Torr) where ionization-induced current is negligible. Thus, the conductivity of the device (G) can be expressed as G = I/V = JA/Eγd. I-V characteristics of GIS with p-type ZnO NWs grown on Au layer is illustrated in Figure 5.27.

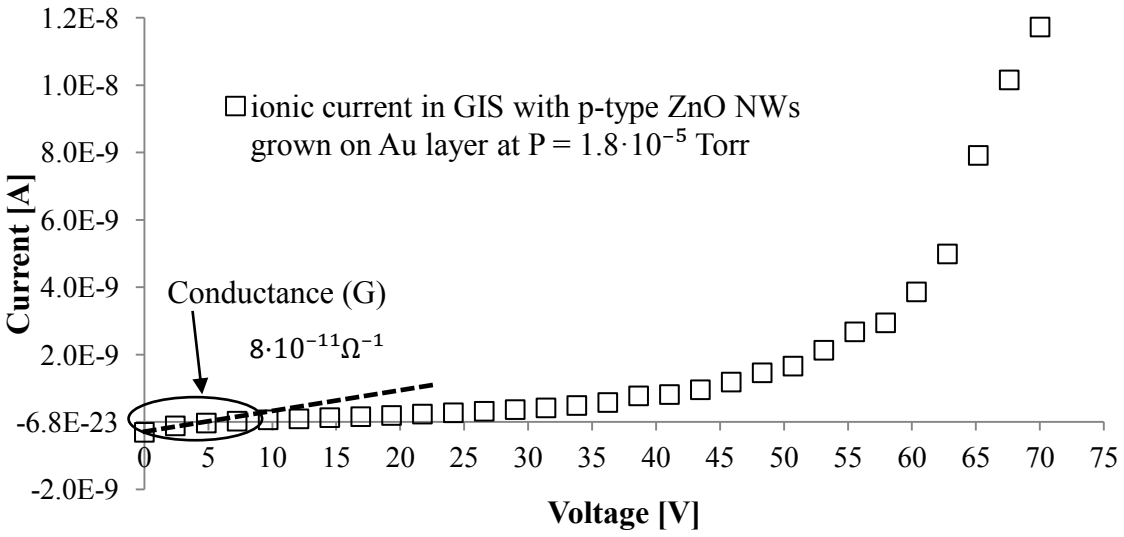

Figure 5.27. I-V characteristics of GIS with p-type ZnO NWs grown on Au layer at P = $1.8 \cdot 10^{-5}$ Torr.

The linear region is emphasized in Figure 5.27. From the slope of the curve in linear region the conductivity is obtained such as $8 \cdot 10^{-11}$ [A/V] at P = $1.8 \cdot 10^{-5}$ Torr, in GIS

with p-type ZnO NWs grown on Au layer. Calculated field enhancement factor is 5132. The geometry of the nanowire includes the length of 1 μm, radius of 12 nm, h of -26, interspace of 50 nm, a of 1, and calculated b of 2683.8. The enhancement factor calculated using Equation (5.17) in one nanowire is $1.026 \cdot 10^5$.

In the case of p-type ZnO NWs grown on n^+-type Si we used Equation (5.15) to estimate field enhancement factor. For this the effective area of electrons emission was derived using SEM analysis. From the SEM image of p-type ZnO NWs grown on Au layer area of 1000 nm × 1000 nm provides with 82 NWs with diameters between 30 nm and 50 nm. The effective number of the NWs on the surface of the gas sensor is around $[346.36 \cdot 10^{12} nm^2/(1000)^2 nm^2] \cdot 82 = 2.84 \cdot 10^{10}$, and calculated emitting area assuming that all area of the tip emit electrons is about $2.84 \cdot 10^{10} \cdot (20nm)^2 \cdot \pi = 35.6885 \cdot 10^{12}$ (nm^2) =35.6885 (mm^2). A typical field-emission current density-applied field (J-E) curve and the Fowler-Nordheim plot $\ln(J/E^2)$ versus I/E are experimentally attained and illustrated in Figure 5.28.

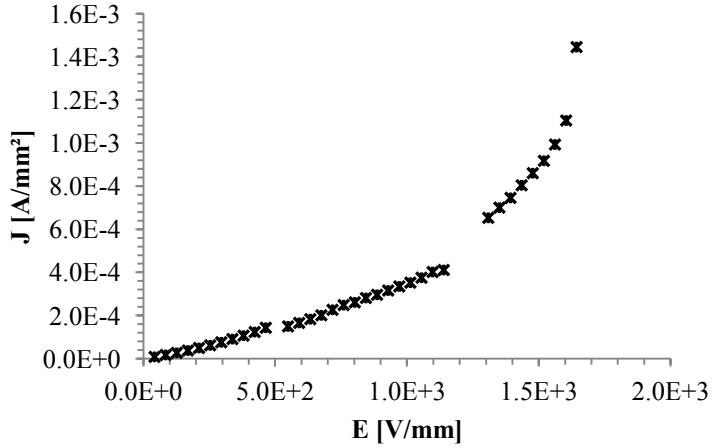

a)

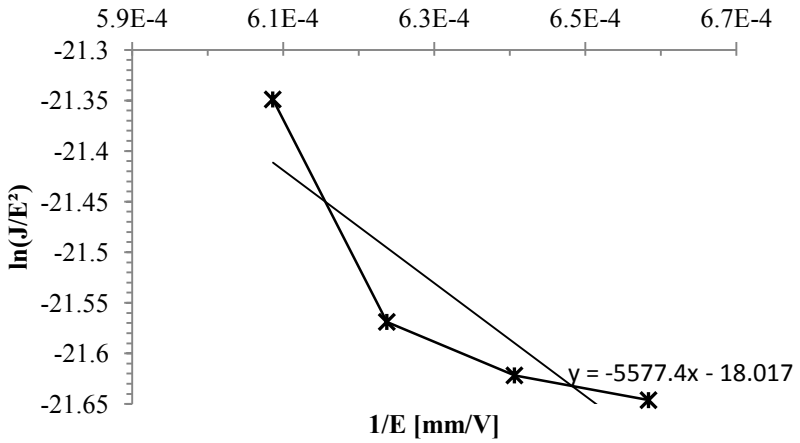

b)

Figure 5.28. a) J-E curve generated in GIS with p-type ZnO NWs grown on n^+-type Si showing the electric field (1.64 kV mm^{-1}) for an emission current density of 1.44 mA mm^{-2}, and b) Fowler-Nordheim plot $\ln(J/E^2)$ versus 1/E corresponding to (a).

The function of $\ln(J/E^2)$ is derived from Equation (5.15) as

$$\ln\left[\frac{J}{E^2}\right] = -\frac{v(f)\cdot b\cdot \phi^{3/2}}{\gamma E} + \ln\left(\frac{a\cdot \gamma^2}{(1.07)^2\cdot \phi}\right) \tag{5.24}$$

where first term ($\frac{b\cdot \phi^{3/2}}{\gamma}$) is the slope of the curve can be employed to calculate field enhancement factor. From slope the obtained field enhancement factor is 14941.8 at ZnO work function of 5.3 eV which is higher compared to GIS with p-type ZnO NWs grown on Au layer (γ = 5132). In fact, similar enhancement factor of the ZnO nanobelts of $1.4\cdot10^4$ was reported by W. Wang et al. [105]. The field enhancement in one nanowire is calculated from Equation (5.17) for space between NWs (100 nm) much less compared to the NW's length (1000 nm). If h = -26, a = 1, NW's radius 20 nm then calculated b = 8554.86 and enhancement factor of one nanowire (γ_0) is $1.5\cdot10^5$ where around 5 nanoprotrusions. The field enhancement factor of one nanoprotrusion is about $3.0\cdot10^4$. Significant field enhancement factors are obtained because of the morphology of created

nanowires (decreased diameters of the tips, nanoprotrusions on the NWs apexes) and uniform distribution of grown ZnO NWs.

The summary of the breakdown voltages in Ar in GISs with metallic and semiconductive nanowires in Field Emission mode are illustrated in Table 5.6.

Table 5.6. Breakdown voltages in nanowires-based GISs in Ar atmosphere (FE mode).

Gas Ar [Torr]	V_{B1}[V]	V_{B2} [V]	V_{B3} [V]	V_{B4} [V]	References V_B
	FE mode	FE mode	FE mode	FE mode	FE mode
0.1	284	280	287	96	210 [105], 163 [54], 310 [55]
0.15	270	274	269	88	162 [105]
0.23	247	268			
0.25	243		255	123	

V_{B1} - GIS (n-type ZnO NWs on PS) in FE mode
V_{B2} - GIS (n-type ZnO NWs on n^+-type Si)
V_{B3} - GIS (p-type ZnO NWs on n-type Si)
V_{B4} - GIS (p-type ZnO NWs on n^+-type Si)

As it can be seen, GIS (V_{B4}) developed in a course of our investigation illustrated the lowest breakdown voltages in Ar in FE mode.

Following, the summary of the breakdown voltages in Ar in GISs with metallic and semiconductive nanowires (FI mode) are illustrated in Table 5.7. Once more, GISs with doped ZnO NWs illustrated superior performance compared to other ionization sensors.

Table 5.7. Breakdown voltages in nanowires-based GISs in Ar atmosphere (FI mode).

Ar Gas	V_{B2} [V]	V_{B3} [V]	V_{B4} [V]	V_{B5} [V]	References V_B
	FI mode	FI mode	FI mode	FI mode	FI mode
0.1 Torr	324	339	22	57	68 [54], 173/290 [96], 375 [55], 353 [106]
0.15 Torr	305	269	24	57	173/270 [96]
0.23 Torr	285	266			
0.25 Torr			15		173/235 [96]

V_{B5} - GIS (p-type ZnO NWs on Au layer) in FI mode

The summary of the breakdown voltages in N_2, O_2, and He in GISs with metallic and semiconductive nanowires are illustrated in Table 5.8.

Table 5.8. Breakdown voltages in N_2, O_2, He using NWs-based GISs.

Gas		V_{B4} in FI mode [V]	V_{B5} in FI mode [V]	References in FI mode [V]
N_2	0.01Torr	19	53	475[106]
	0.1 Torr	24	55	450[106]
O_2	0.01Torr	32	56	
	0.1 Torr	29	57	
He	0.01Torr	22	59	
	0.1 Torr	20	63	

As it is shown in Table 5.8, the novel GISs with p-type ZnO NWs fabricated in present work significantly improved performance. Moreover, these devices illustrated superior repeatability and selectivity. They were used in different type of gases at different compliances 1μA, 1 mA, and 10 mA, and 100 mA demonstrating repeatable results with standard deviation between 2.6 and 6.2. The best performance and high generated currents (in mA) were demonstrated by GIS with p-type ZnO NWs grown on n^+-type Si, following by GIS with p-type ZnO NWs grown on Au layer. Experimental investigations have been shown that these sensors can be used to detect different gases in an air and in a vacuum. Gas recognition can be based on the generated ohmic current at applied bias voltage or the breakdown voltage in field-limited regime.

The conducted research on performance of the GISs with n-type and p-type ZnO NWs illustrated that GIS with p-type ZnO NWs significantly improved performance of the sensor (breakdown voltages in a range of 15 V to 40 V) and illustrated good sensitivity and repeatability. The p-type ZnO NWs with nanoprotrusions illustrated the highest field enhancement factor ($\gamma = 1.5 \cdot 10^4$).

6. Concluding Remarks, Contributions and Suggestion for Future Work

6.1. Concluding Remarks and Contributions

In this work, growth of crystalline ZnO NWs with controlled geometric shape and distribution on the substrate is reported. SEM analyses have shown that geometric shape of the nanostructures depends on the conductivity of the substrates used for electrochemical growth of ZnO NWs, as well as the temperature and concentration of electrolyte control the crystalline structure, shape of the nanowires in particular their tips, and their distribution on the substrates. The nanowires were doped using Ag and Al impurities dopants. Ag-doped ZnO NWs illustrated p-type conductivity and Al-doped ZnO NWs have shown enhanced n-type conductivity. It was observed that the p-type conductivity of the nanowires is strongly dependent on the conductivity of the substrates.

COMSOL multiphysics is used to optimize the physical dimensions of ZnO NWs and their distribution to suit the best for fabrication of the GIS. The simulations showed that the geometry of the nanowires as well as the screening effect are the dominant factors on altering the electric field between the two parallel plates. It is illustrated that ZnO NWs with a large tips curvatures are advantageous, since they provide the highest electric fields at the vicinity of the NWs pinnacles. The nanowires with structures to suit the GIS the best are synthesized using electrochemical technique, utilized to design the GIS.

A gas ionization sensor (GIS) based on grown ZnO nanowires was designed, and fabricated. P-type and n-type crystalline ZnO NWs grown on semiconductor or metallic substrates were successfully placed between the two parallel plates. The fabricated GISs

are characterized, while nanowires were used either as an anode or cathode electrodes between two parallel planes. The best performance and high generated currents (in mA) are demonstrated by GIS made with p-type ZnO NWs grown on n^+-type Si, following by GIS made with p-type ZnO NWs grown on Au layer. Experimental investigations have been shown that these sensors can be used to detect various gases in an air and in a vacuum. Gas recognition can be based on the generated ohmic current at applied bias voltage or the breakdown voltage in field-limited regime. Electrical characteristics of the gas ionization detector demonstrated superior performance, sensitivity, and repeatability compare to those fabricated using metallic nanowires, and reported in the literature. The enhancement factor of about 15000 was calculated for the devices made of p-type ZnO NWs grown on n^+-type Si, and about 5000 for those made of p-type ZnO NWs grown on Au layer.

We can summarize the contributions of this research to the field of nanowires fabrications and their applications in developing a sensitive GIS as:

- Electrochemically grown self-assembled crystalline ZnO NWs with controlled geometry of the apexes and distribution on the substrate.
- One-step doping of ZnO NWs during electrochemical fabrication. P-type ZnO NWs employing Ag impurities and n^+-type ZnO NWs using Al impurities are achieved.
- Controlled doping has been accomplished by using substrates with various conductivities.
- Gas ionization sensors based on n-type or p-type ZnO NWs are designed and fabricated.

- GISs were used to detect leakage of gases in atmosphere as well as pure gases at very low pressures. Gas detectors illustrated very good performance, selectivity, and repeatability.
- The GISs were studied in both field ionization (FI) and field emission (FE) modes. The studies show that GISs made with p-type nanowires have low breakdown voltages in FI mode, and GISs fabricated with n-type nanowires have low breakdown voltages in FE mode.
- GISs with p-type ZnO NWs have illustrated low-voltage field-ionization in field-limited region in different gases and variation of ohmic current at applied bias voltage. Thus, detection of gases can be based on detection of the ohmic current at applied bias voltage, or by detection of the breakdown voltage in field-limited regime.
- High value of field enhancement factor was accomplished in p-type ZnO NWs grown on n^+-type Si where nanoprotrusions on NWs tips increased the local electric fields.

6.2. Suggestion for Future Works

Further development on the controlled doping to tailor the electrical and magnetic properties of ZnO NWs can be explored.

Future work can be performed on

— development of the novel devices with tailored geometry, conductivity, and magnetic properties of crystalline ZnO nanowires;

— studying the breakdowns and ionization behavior of GIS in low gas pressures and in mixtures of gases;

— creation of an array of the miniaturized GISs with ZnO NWs to develop an odor sensor.

References

[1] R. B. Sadeghian and Mojtaba Kahrizi, “A novel miniature gas ionization sensor based on freestanding gold nanowires,” *Sensors and Actuators A*, vol. 137, pp. 248-255, March, 2007.

[2] S. Xavier, S. Mátéfi-Tempfli, E. Ferain, S. Purcell, S. Enouz-Védrenne, L. Gangloff, E. Minoux, L. Hudanski, P. Vincent, J.-P. Schnell, D. Pribat, L. Piraux, and P. Legagneux, "Stable field emission from arrays of vertically alighed free-standing metallic nanowires," *Nanotechnology*, vol. 19, 215601, pp. 1-7, April, 2008.

[3] Y. Ye, L. Dai, L. Gan, H. Meng, Y. Dai, X. Guo, and G. Qin, “Novel optoelectronic devices based on single semiconductor nanowires (nanobelts),” *Nanoscale Research Letters*, 7:218, pp. 1-7, 2012.

[4] A. Mourachkine, O. V. Yazyev, C. Ducati, and J.-Ph. Ansermet, “Template nanowires for spintronics applications: nanomagnet microwave resonators functioning in zero applied magnetic field,” *Nano Letters*, *8(11)*, pp. 3683-3687, September, 2008.

[5] J. Geurts, “Crystal structure, chemical binding, and lattice properties”, Chapter 2, Zinc Oxide: From Fundamental Properties Towards Novel Applications, ed. C. F. Klingshirn, B. K. Meyer, A. Waag, A. Hoffmann, J. Geurts, Springer-Verlag Berlin Heidelberg, pp.7-37, 2010.

[6] C. Klingshirn, “Review Article. ZnO: From basics towards applications,” *Physica Status Solidi (b)*, *244(9)*, pp. 3027-3073, 2007.

[7] H. Morkoç and Ü. Özgür, “General properties of ZnO”, Chapter 1, Zinc Oxide: Fundamentals, Materials and Device Technology, Wiley-VCH Verlag GmbH & Co. KGaA, Weinheim, 2009, pp. 63-70. Available online: http://media.johnwiley.com.au/product_data/excerpt/34/35274081/3527408134.pdf as of 15/04/2013.

[8] M. J. Zheng, L. D. Zhang, G. H. Li, W. Z. Shen, "Fabrication and optical properties of large-scale uniform zinc oxide nanowire arrays by one-step electrochemical deposition technique," *Chemical Physics Letters,* vol. 363, pp. 123-128, September, 2002.

[9] D. Ramirez, T. Pauporte, H. Gomez, and D. Lincot, "Electrochemical growth of ZnO nanowires inside nanoporous alumina templates. A comparison with metallic Zn nanowires growth," *Phys. Stat. Sol. (a)*, *205 (10)*, pp. 2371-2375, 2008.

[10] Y. Leprince-Wang, G. Y. Wang, X. Z. Zhang, D. P. Yu, "Study on the microstructure and growth mechanism of electrochemical deposited ZnO nanowires," *journal of Crystal Growth*, vol. 287, pp. 89-93, 2006.

[11] J. Cui, "Growth condition dependence of zinc oxide nanostructures on Si substrates in an electrochemical process," *journal Mater Sci: Mater Electron,* vol. 19, pp. 908-914, March, 2008.

[12] J. B. Cui, "Structural and optical properties of periodically ordered ZnO nanowires," *Science in China Series E: Technological Sciences*, *52 (2)*, pp.313-317, February, 2009.

[13] R. Könenkamp, R. C. Word, M. Dosmailov, J. Meiss, and A. Nadarajah, "Selective growth of single-crystalline ZnO nanowires on doped silicon," *journal of Applied Physics*, vol. 102, pp. 056103-1-056103-3, September, 2007.

[14] J. B. Shim, J. W. Grant, W. R. Harrell, H. Chang, S.-O Kim, "Electrical properties of rapid hydrothermal synthesized Al-doped zinc oxide nanowires in flexible electronics," *Micro & Nano Letters*, 6(3), pp. 147-149, 2011.

[15] N.-H. Kim, S.-H. Jung, J. H. Park, K.-H. Lee, K. Cho, "A three-dimensional transparent electrode structure with Al-doped ZnO nanorods," *IEEE Transactions on Nanotechnology*, 10(6), pp.1347-1351, November, 2011

[16] M. A. Thomas and J. B. Cui, "Electrochemical route to p-type doping of ZnO nanowires," *J. Phys. Chem. Lett.*, *1(7)*, pp.1090-1094, 2010.

[17] J. Cui and U. J. Gibson, "Enhanced nucleation, growth rate, and dopant incorporation in ZnO nanowires," *J. Phys. Chem. B*, vol. 109, pp. 22074-22077, 2005.

[18] M.-P. Lu, J. Song, M.-Y. Lu, M.-T. Chen, Y. Gao, L.-J. Chen, and Z. L. Wang, "Piezoelectric nanogenerator using p-type ZnO nanowires arrays," *Nano Lett.*, *9(3)*, pp. 1223-1227, 2009.

[19] G. Zhu, R. Yang, S. Wang, Z. L. Wang, "Flexible high-output nanogenerator based on lateral ZnO nanowire array," *Nano Lett.*, *10(8)*, pp. 3151-3155, 2010.

[20] Z. L. Wang and J. Song, "Piezoelectric nanogenerators based on zinc oxide nanowire arrays," *Science*, *312 (5771)*, pp. 242-246, April, 2006.

[21] S. N. Cha, J.-S. Seo, S. M. Kim, H. J. Kim, Y. J. Park, S.-W. Kim, and J. M. Kim, "Sound-driven piezoelectric nanowire-based nanogenerators," *Advanced Materials*, vol. 22, pp.4726-4730, 2010.

[22] H. Zhou, M. Wissinger, J. Fallert, R. Hauschild, F. Stelzl, C. Klingshirn, and H. Kalt, "Ordered, uniform-sized ZnO nanolaser arrays," *Applied Physics Letters*, *91(181112)*, pp. 1-3, 2007.

[23] M. H. Huang, S. Mao, H. Feick, H. Yan, Y. Wu, H. Kind, E. Weber, R. Russo, P. Yang, "Room-temperature ultraviolet nanowire nanolasers," *Science*, *292(8)*, pp. 1897-1899, June, 2001.

[24] G. Visimberga, E. E. Yakimov, A. N. Redkin, A. N. Gruzintsev, V. T. Volkov, S. Romanov, and G. A. Emelchenko, "Nanolasers from ZnO nanorods as natural resonance cavities," *Physica Status Solidi C*, *7(6)*, pp. 1668-1671, 2010.

[25] Y. Zhang, R. E. Russo, S. S. Mao, "Quantum efficiency of ZnO nanowire nanolasers," *Applied Physics Letters*, vol. 87, pp. 043106-1 – 043106-3, 2005.

[26] M.-H. Lai, A. Tubtimtae, M.-W. Lee, and G.-J. Wang, "ZnO-nanorod dye-sensitized solar cells: new structure without a transparent conducting oxide layer," *International journal of Photoenergy*, vol. 2010, pp. 1-5, 2010.

[27] E. Galoppini, J. Rochford, H. Chen, G. Saraf, Y. Lu, A. Hagfeldt, G. Boschloo, "Fast electron transport in metal organic vapor deposition grown dye-sensitized ZnO

nanorod solar cells," *journal of Physical Chemistry Letters B*, vol. 110, pp. 16159-16161, 2006.

[28] O. Lupan, V. M. Guérin, I. M. Tiginyanu, V. V. Ursaki, L. Chow, H. Heinrich, T. Pauporté, "Well-aligned arrays of vertically oriented ZnO nanowires electrodeposited on ITO-coated glass and their integration in dye sensitized solar cells," *journal of Photochemistry and Photobiology A: Chemistry*, vol. 211, pp. 65-73, February, 2010.

[29] Y. F. Zhu, G. H. Zhou, H. Y. Ding, A. H. Liu, Y. B. Lin, and N. L. Li, "Synthesis of highly-ordered hierarchical ZnO nanostructures and their application in dye-sensitized solar cells," *journal of Crystal Research and Technology*, *45(10)*, pp. 1075-1078, 2010.

[30] J. Qiu, X. Li, F. Zhuge, X. Gan, X. Gao, W. He, S.-J. Park, H.-K. Kim, and Y.-H. Hwang, "Solution-derived 40 μm vertically aligned ZnO nanowire arrays as photoelectrodes in dye-sensitized solar cells," *Nanotechnology*, vol. 21, 195602, pp. 1-9, 2010.

[31] P. Atienzar, T. Ishwara, B. N. Illy, M. P. Ryan, B. C. O'Regan, J. R. Durrant, and J. Nelson, "Control of photocurrent generation in polymer/ZnO nanorod solar cells by using a solution-processed TiO_2 overlayer," *journal of Physical Chemistry Letters*, vol. 1, pp. 708-713, January, 2010.

[32] F.-T. Liu, S.-F. Gao, S.-K. Pei, S.-C. Tseng, C.-H. J. Liu, "ZnO nanorod gas sensor for NO_2 detection," *journal of the Taiwan Institute of Chemical Engineers*, vol. 40, pp. 528-532, 2009.

[33] J. X. Wang, X. W. Sun, Y. Yang, H. Huang, Y. C. Lee, O. K. Tan and L. Vayssieres, "Hydrothermally grown oriented ZnO nanorod arrays for gas sensing applications," *Nanotechnology*, vol. 17, pp. 4995-4998, 2006.

[34] H. T. Wang, B. S. Kang, F. Ren, L. C. Tien, P. W. Sadik, D. P. Norton, S. J. Peaton, J. Lin, "Detection of hydrogen at room temperature with catalyst-coated multiple ZnO nanorods," *Appl. Phys. A*, *81(6)*, pp. 1117-1119, 2005.

[35] J. Y. Park, S.-W. Choi, and S. S. Kim, "Fabrication of a highly sensitive chemical sensor based on ZnO nanorod arrays," *Nanoscale Research Letters*, *5(2)*, pp. 353-359, February, 2010.

[36] B. Weintraub, Z. Zhou, Y. Li and Y. Deng, "Solution synthesis of one-dimensional ZnO nanomaterials and their applications," *Nanoscale*, vol. 2, pp. 1573-1587, 2010.

[37] M. Liu, "SYNTHESYS OF ZNO NANOWIRES AND APPLICATIONS AS GAS SENSORS," M. Sc. thesis, Department of Chemistry, University of Saskatchewan, Saskatoon, September, 2010.

[38] K. Zhao, X. Chen, Z. Guo, J. Wang, Q. Chang, C. Gu, M. Li, J. Liu, "Field ionization from ZnO nanorod arrays for detecting formic acid in air," *Proc. IEEE-ICIA*, 2007, pp. 253-256.

[39] Y. Zhang, K. Yu, D. Jiang, Z. Zhu, H. Geng, L. Luo, "Zinc oxide nanorod and nanowire for humidity sensor," *Applied Surface Science*, vol. 242, pp. 212-217, 2005.

[40] Q. Qi, T. Zhang, Q. Yu, R. Wang, Y. Zeng, L. Liu, H. Yang, "Properties of humidity sensing ZnO nanorods-based sensor fabricated by screen-printing," *Sensors and Actuators B*, vol. 133, pp. 638-643, 2008.

[41] D. Pradhan, F. Niroui, and K. T. Leung, "High-performance, flexible enzymatic glucose biosensor based on ZnO nanowires supported on a gold-coated polyester substrate," *Applied Materials & Interfaces*, *2(8)*, pp. 2409-2412, July, 2010.

[42] Z. Zhao, W. Lei, X. Zhang, B. Wang, and H. Jiang, "ZnO-based amperometric enzyme biosensors," *Sensors*, vol. 10, pp. 1216-1231, February, 2010.

[43] J. Qiu, W. Yu, X. Gao and X. Li, "Sol-gel assisted ZnO nanorod array template to synthesize TiO_2 nanotube arrays," *Nanotechnology*, vol. 17, pp. 4695-4698, 2006.

[44] J. Goldberger, R. He, Y. Zhang, S. Lee, H. Yan, H.-J. Choi and P. Yang, "Single-crystal gallium nitride nanotubes," *Nature*, vol. 422, pp. 599-602, April, 2003.

[45] J. Hwang, B. Min, J. S. Lee, K. Keem, K. Cho, M.-Y. Sung, M.-S. Lee, and S. Kim, "Al_2O_3 nanotubes fabricated by wet etching of ZnO/Al_2O_3 core/shell nanofibers," *journal of Adv. Mater.*, *16(5)*, pp. 422-425, March, 2004.

[46] G. Clavel, N. Pinna, and D. Zitoun, "Magnetic properties of cobalt and manganese doped ZnO nanowires," *Phys. Stat. Sol. (a)*, *204(1)*, pp.118-124, 2007.

[47] R. B. Sadeghian and M. Kahrizi, "A novel miniature gas ionization sensor based on freestanding gold nanowires," *Sensors and Actuators: A Physical*, *137(2)*, pp. 248–255, July, 2007.

[48] R. B. Sadeghian and M. Kahrizi, "A Novel Gas Sensor Based on Tunneling-Field-Ionization on Whisker-Covered Gold Nanowires," *IEEE Sensors Journal*, *8(2)*, pp. 161–169, 2008.

[49] R. B. Sadeghian, S. Badilescu, Y. Djaoued, S. Balaji, V-V. Truong and M. Kahrizi, "Ultra-low voltage Schottky barrier field enhanced electron emission from gold nanowires electrochemically grown in modified porous alumina templates," *IEEE Electron. Dev. Lett.*, *29(4)*, pp. 312–314, 2008.

[50] R. B. Sadeghian and M. Kahrizi, "A Low Voltage Gas Ionization Sensor based on Sparse Gold Nanorods," Proc. 6th IEEE Sensors Conf., Atlanta, GA, 2007, pp. 648–651.

[51] R. B. Sadeghian and M. Kahrizi, "A Low Pressure Gas Ionization Sensor Using Freestanding Gold Nanowires," Proc. IEEE ISIE, Vigo, Spain, 2007, pp. 1387–1390.

[52] R. B. Sadeghian and M. Kahrizi, "A Field Effect Gas Ionization Sensor based on Self-standing Nanowire Arrays," presented at the Annu. Sci. Popularization Contest, 2006, Sherbrooke.

[53] R. B. Sadeghian and M. Kahrizi, "Miniaturized Gas Ionization Sensor," presented at the 5th CWMEMS Contest, Montréal, 2007.

[54] N. Azmoodeh, N. Chivu, R. B. Sadehian, M. Kahrizi, "A silver nanowire based gas ionization sensor," EUROCON2009, IEEE, pp. 1231-1235, 2009.

[55] E. Fard, "EFFECTS OF FABRICATION PARAMETERES ON POROUS SILICON STRUCTURE WITH SOME POTENTIAL APPLICATIONS," M.Sc. thesis, Dept. Electrical and Computer Eng., Concordia Univ., Montreal, Canada, 2009.

[56] R. B. Sadeghian and M. S. Islam, "Ultralow-voltage field-ionization discharge on whiskered silicon nanowires for gas-sensing applications," *Nature Materials*, vol. 10, pp 135-140, 2011.

[57] A. J. Bard and L. R. Faulkner, *Electrochemical Methods: fundamentals and applications*, 2nd ed., John Wiley & Sons, Inc., 2001, pp. 1-90.

[58] P. P. Konorov, A. M. Yafyasov, V. B. Bogevolnov, *Field Effect in Semiconductor-Electrolyte Interfaces: Application to Investigations of Electronic Properties of Semiconductor Surfaces*, Princeton University Press, 2006, pp. 1-11.

[59] R. Williams, "Electrochemical reactions of semiconductors," *j. Vac. Sci. Technol.*, *13(1)*, pp.12-18, 1975.

[60] C. M. A. Brett and A. M.O. Brett, *Electrochemistry Principles, Methods, and Applications*, Oxford University Press Inc., 1993, pp.2-68.

[61] T. Yoshida, D. Komatsu, N. Shimokawa and H. Minoura, "Mechanism of cathodic electrodeposition of zinc oxide thin films from aqueous zinc nitrate baths," *journal of Thin Solid Films*, vol. 451-452, pp. 166-169, 2004.

[62] S. N. Cha, B. G. Song, J. E. Jang, J. E. Jung, I. T. Han, J. H. Ha, J. P. Hong, D. J. Kang and J. M. Kim, "Controlled growth of vertically aligned ZnO nanowires with different crystal orientation of the ZnO seed layer," *Nanotechnology*, vol. 19, pp. 1-4, 2008.

[63] J. Liu, W. Wu, S. Bai, Y. Qin, "Synthesis of high crystallinity ZnO nanowires array on polymer substrate and flexible fiber-based sensor," *ACS Appl. Mater. Interfaces*, 3(11), pp. 4197-4200, 2011.

[64] I. Amarilio-Burshtein, S. Tamir, Y. Lifshitz, "Growth modes of ZnO nanostructures from laser ablation," *journal of Applied Physics Letters*, vol. 96, pp.103104-1-103104-3, 2010.

[65] G. Zhu, Y. Zhou, S. Wang, R. Yang, Y. Ding, X. Wang, Y. Bando, Z. L. Wang, "Synthesis of vertically alighned ultra-long ZnO nanowires on heterogeneous substrates with catalyst at the root," *Nanotechnology*, vol. 23, pp. 1-6, 2012.

[66] S. Ashraf, A. C. Jones, J. Bacsa, A. Steiner, P. R. Chalker, P. Beahan, S. Hindley, R. Odedra, P. A. Williams, P. N. Heys, "MOCVD of vertically aligned ZnO nanowires using bidentate ether adducts of dimethylzinc," *Chemical Vapor Deposition*, vol.17, pp. 45-53, 2011.

[67] C. Cheng, T. L. Wong, W. Li, C. Zhu, S. Xu, L. Wang, K. K. Fung, N. Wang, "Carbon-assisted nucleation and vertical growth of high-quality ZnO nanowire arrays," *AIP Advances*, vol. 1, pp. 032104-1-032104-6, 2011.

[68] J. Yang, J. Lang, L. Yang, Y. Zhang, D. Wang, H. Fan, H. Liu, Y. Wang, M. Gao, "Low-temperature growth and optical properties of ZnO nanorods," *journal of Alloys and Compounds*, vol. 450, pp.-521-524, 2008.

[69] J. E. Boercker, J. B. Schmidt, and E. S. Aydil, "Transport Limited Growth of Zinc Oxide Nanowires," *Crystal Growth and Design*, *9 (6)*, pp. 2783-2789, April, 2009.

[70] J. Qiu, X. Li, W. He, S.-J. Park, H.-K. Kim, Y.-H. Hwang, J.-H. Lee and Y.-D. Kim, "The growth mechanism and optical properties of ultralong ZnO nanorod arrays with a high aspect ratio by a preheating hydrothermal method," *Nanotechnology*, *20 (15)*, March, 2009.

[71] K. Govender, D. S. Boyle, P. B. Kenway and P. O'Brien, "Understanding the factors that govern the deposition and morphology of thin films of ZnO from aqueous solution," *journal of Materials Chemistry,* vol. 14, pp.2575-2591, 2004.

[72] M. Willander, P. Klason, L. L. Yang, Safaa M. Al-Hilli, Q. X. Zhao, O. Nur, "ZnO nanowires: chemical growth, electrodeposition, and application to intracellular nano-sensors," *Phys. Stat. Sol. (c)*, vol. 5 (9), pp.3076-3083, March, 2008.

[73] J. P. Kar, M. H. Ham, S. W. Lee, and J. M. Myoung, "Fabrication of ZnO nanostructures of various dimentions using patterned substrates," *journal of Applied Surface Science*, vol. 255, pp.4087-4092, 2009.

[74] A. Dev, S. Chaudhuri, B. N. Dev, "ZnO 1-D nanostructures: Low temperature synthesis and characterizations, " *Bull. Mater. Sci.*, *31(3)*, pp. 551-559, June, 2008

[75] S. Spitsina, I. Stateikina, M. Chaker, and M. Kahrizi, "Studies on self-assembled ZnO nanorods/nanowires grown on silicon substrates by electrochemical deposition," in Proc. of 3rd ICHMM-2011, May 22-26, 2011, Shanghai, China.

[76] P. Banerjee, W.-J. Lee, K.-R. Bae, S. B. Lee, and G. W. Rubloff, "Structural, electrical, and optical properties of atomic layer deposition Al-doped ZnO films," *J. Appl. Phys.*, 108, pp.043504-1-043504-7, 2010.

[77] J. Fan, A. Shavel, R. Zamani, C. Fábrega, J. Rousset, S. Haller, F. Güell, A. Carrete, T. Andreu, J. Arbiol, J. R. Morante, A. Cabot, "Control of the doping concentration, morphology and optoelectronic properties of vertically aligned chlorine-doped ZnO nanowires," *Acta Materialia*, 59, pp. 6790-6800, 2011.

[78] J. B. Cui, Y. C. Soo, and T. P. Chen, U. J. Gibson, "Low-temperature growth and characterization of Cl-doped ZnO nanowire arrays," *J. Phys. Chem. C*, 112, pp. 4475-4479, 2008.

[79] X. Yang, A. Wolcott, G. Wang, A. Sobo, R. C. Fitzmorris, F. Qian, J. Z. Zhang, and Y. Li, "Nitrogen-doped ZnO nanowire arrays for photoelectrochemical water splitting," *Nano Letters*, *9*(6), pp. 2331-2336, 2009.

[80] H. Y. Xu, Y. C. Liu, R. Mu, C. L. Shao, Y. M. Lu, D. Z. Shen, and X. W. Fan, "F-doping effects on electrical and optical properties of ZnO nanocrystalline films," *Appl. Phys. Lett.*, 86, pp-123107-1-123107-3, 2005.

[81] _____, "Introduction to energy dispersive X-ray Spectroscopy (EDXS)" [Online]. Available: http://micron.ucr.edu/public/manuals/EDS-intro.pdf as of 2/5/2013.

[82] _____, "Energy dispersive x-ray spectroscopy," Handbook of analytical methods for materials [Online]. Available: http://mee-inc.com/eds.html as of 2/10/2013.

[83] R. van de Krol, "Principles of photoelectrochemical cells," Chapter 2, Photoelectrochemical Hydrogen Production, ed. Roel van de Krol and M. Grätzel, Spinger Science+Business Media, LLC 2012, pp. 13-67, [Online]. Available: http://link.springer.com/book/10.1007/978-1-4614-1380-6/page/1as of 3/5/2013.

[84] N. C. Strandwitz, J. Good, N. S. Lewis, "Photoelectrochemistry of semiconductors," Electrochemistry Encyclopedia [Online]. Available: http://electrochem.cwru.edu/encycl/art-p06-photoel.htm as of 2/5/2012.

[85] A.M. Howatson, "Breakdown", chapter 3, An Introduction to Gas Discharges, Pergamon Press Ltd., 1965, pp. 51-105.

[86] E. Kuffel and M. Abdullah, Chapter 1-2, High-voltage Engineering, Pergamon Press Ltd., 1970, pp. 6-96.

[87] _____, Available: http://www.physics.nus.edu.sg/~L3000/Level3manuals/plasma%20physics.pdf as of 12/5/2012.

[88] _____, Available: http://fr.wikipedia.org/wiki/Loi_de_Paschen as of 12/15/2013.

[89] J. M. Meek and J. D. Craggs. "Electrical Breakdown of gases", chapter 2, edited by N. F. Mott and Sir Edward Bullard, Oxford university Press, 1953, pp. 80-100.

[90] _____, WebElements. Available: http://www.webelements.com/ as of 1/10/2013.

[91] _____, Ionization Energies (eV) of Atoms and Ions. Available: http://dept.astro.lsa.umich.edu/~cowley/ionen.htm as of 12/10/2012.

[92] E. W. Müller and K. Bahadur, "Field ionization of gases at a metal surface and the resolution of the field ion microscope," *journal "Physical Review"*, *102(3)*, pp. 624-631, 1956.

[93] T. T. Tsong, "Atom-probe field ion microscopy," *journal Physics Today*, pp. 24-31, 1993.

[94] E. W. Müller and T. T. Tsong, "Field ionization", Field Ion Microscopy: Principles and Applications, Elsevier Publishing Company, Ltd., 1969, pp.10-54.

[95] Y. Ohno, S. Nakamura, T. Kuroda, "Mechanisms of field ionization and field evaporation on semiconductor surfaces," *Japanese Journal of Applied Physics*, 17(11), pp.2012-2022, November, 1978.

[96] R. B. Sadeghian, "A FIELD EFFECT GAS SENSOR BASED ON SELF-STANDING NANOWIRE ARRAYS," Ph. D. Thesis in a Department of Electrical and Computer Engineering, Concordia University, Montreal, 2007.

[97] P. Soldán, E. P. F. Lee and T. G. Wright, "Static dipole polarizabilities (α) and static second hyperpolarizabilities (γ) of the rare gas atoms (He-Rn)," *Phys. Chem. Chem. Phys.*, vol. 3, pp. 4661-4666, 2001.

[98] X. Liu and J. Orloff, "Analytical model of a gas phase field ionization source," *journal Vac. Sci. Technol. B*, *23(6)*, pp. 2816-2820, 2005.

[99] J. D. Carey and S. R. P. Silva, "Nanostructured Materials for Field Emission Devices", Nanomaterials Handbook, ed. By Y. Gogotsi, pp. 666-667.

[100] R. G. Forbes, "The physics of generalized Fowler-Nordheim-type equations", IEEEXplore [Online], 2007. Available: http://ieeexplore.ieee.org/stamp/stamp.jsp?arnumber=04480924 as of 9/5/2012.

[101] R. G. Forbes, "Description of field emission current/voltage characteristics in terms of scaled barrier field values (f-values)", *journal of Vacuum Science Technology B*, 26(1), pp. 209-213, Jan/Feb, 2008.

[102] R. G. Forbes and J. H. B. Deane, "Reformulation of the standard theory of Fowler-Nordheim tunneling and cold field electron emission", Proceedings The Royal Society A [Online], vol. 463, pp. 2907-2927, 2007. Available online: http://rspa.royalsocietypublishing.org/content/463/2087/2907.full.pdf+html as of 9/6/2012.

[103] X. Qian, H. Liu, Y. Guo, Y. Song, Y. Li, "Effect of aspect ratio on field emission properties of ZnO nanorod arrays," *Nanoscale Res. Lett.*, , vol. 3, pp. 303-307, 2008.

[104] W. Wang, B. Zeng, J. Yang, B. Poudel, J. Huang, M. J. Naughton, and Z. Ren,"Alighned Ultralong ZnO nanobelts and their enhanced field emission," *Adv. Mater.*, vol. 18, pp. 3275-3278, 2006.

[105] R. B. Sadeghian, N. Chivu, and M. Kahrizi, "Subtorr Operation of a miniature Gas Ionization Sensor Based on Gold Nanowires," Sensors and Materials, 21 (1), pp.53-64, 2009.

[106] H. Wang, C. Zou, C. Tian, L. Zhou, Z. Wang, D. Fu, "A novel gas ionization sensor using Pd nanoparticle-capped ZnO," *Nanoscale Research Letters*, 6:534, 2011.

Appendix A

GIS with ZnO NWs: Simulations of GIS Models (COMSOL) and Experimental Results

A.1. Boundary Conditions

The applied boundary conditions were given as

$$\mathbf{n}_2 \times \left(\mathbf{F}_1 - \mathbf{F}_2\right) = 0 \tag{A.1a}$$

$$\mathbf{n}_2 \cdot \left(\mathbf{D}_1 - \mathbf{D}_2\right) = \rho_s \tag{A.1b}$$

where ρ_s is the surface charge density and n_2 is the outward normal from medium 2 which represents continuous electric field across a boundary (Equation (A.1a)), the discontinuity in the normal component of electric flux density (**D)** is the same as the surface charge density ρ_s on the boundary between two mediums (Equation A.1b).

The continuity equation represents the conservation of the electric charge, and it is expressed as

$$\nabla \cdot \mathbf{J} = 0 \tag{A.2}$$

where **J** is the current density vector.

The macroscopic properties of the medium were given as

$$\mathbf{D} = \varepsilon_0 \mathbf{F} + \mathbf{P} = \left(1 + \chi_e\right)\varepsilon_0 \mathbf{F} \tag{A.3a}$$

$$\mathbf{J} = \sigma \mathbf{F} \tag{A.3b}$$

$$\mathbf{F} = -\nabla \mathrm{V} \tag{A.3c}$$

$$-\nabla \cdot \left(\varepsilon_0 \nabla V - \mathbf{P}\right) = \rho \tag{A.3d}$$

where **P** is the polarization vector (describes how the material is polarized (C/m^2)), in our model the polarization was omitted (P = 0), χ_e is the electric susceptibility, ε_0 is the permittivity of a vacuum ($8.854 \cdot 10^{-12}$ (F/m)), ε_r is the relative permittivity or the dielectric constant of the medium, σ is the electric conductivity, V is the electric scalar potential, and ρ is the volume charge density (C/m^3).

A.2. Meshes of Models in COMSOL and Simulations Results

2D model includes 24147 elements. This is physics-controlled mesh with element size 'extremely fine'. 3D model has 112240 elements. This is user-defined mesh, where nanowires were meshed with the maximum element size 10^{-6} m and minimum element size of $5 \cdot 10^{-8}$ m. The maximum growth rate was 1.5. This means that the element size grows by at most 50% approximately from one element to another. The resolution of curvature, which defines the element size along curved boundaries, was 0.5. For example, for curvature radius $0.2 \cdot 10^{-6}$ m maximum allowed element size along the boundary is $0.2 \cdot 0.5 \cdot 10^{-6}$=100 nm. The resolution of narrow regions was chosen less than 1, it was 0.85. The distribution of the electric field intensity in 2D model is illustrated in Figure A.1.

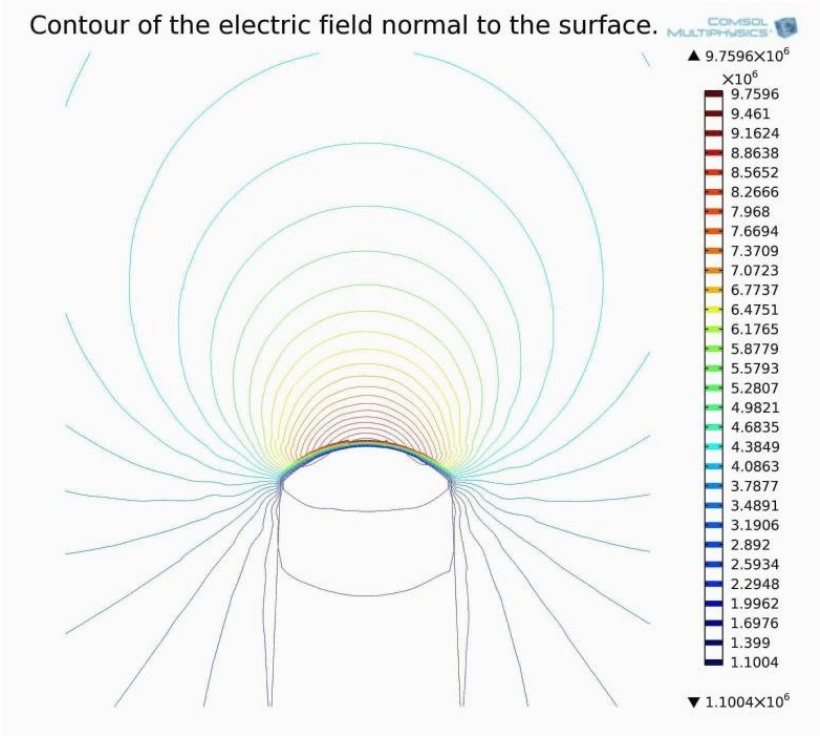

a)

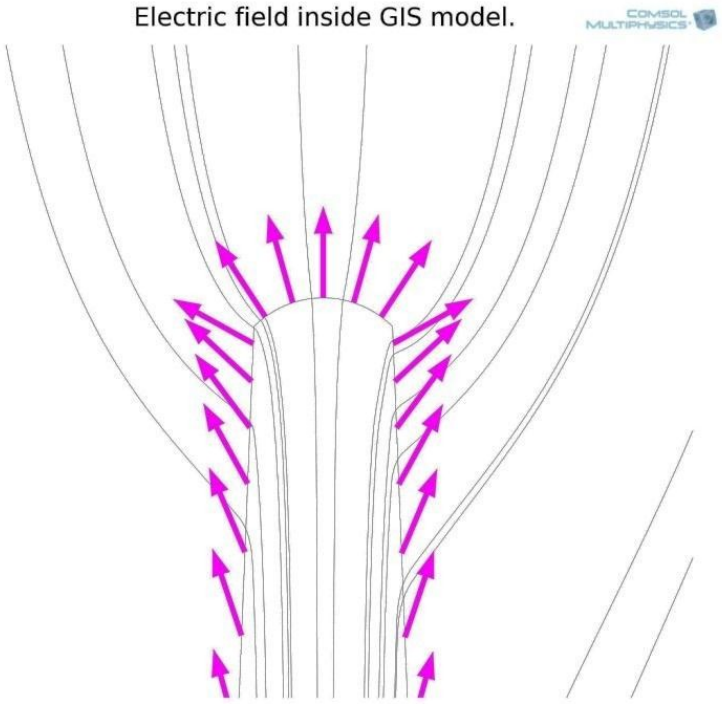

b)

Figure A.1. a) Equipotential lines of the electric field in 2D GIS model in vicinity of the ZnO NWs, b) direction and density of the electric field intensity.

The maximum electric field intensity was obtained in the vicinity of NW tip. Direction of the electric field was perpendicular to the surface of the curved NW tip. Also, the electric field along the nanowire was directed under angle to the surface less than normal.

Following illustrations are 2D and 3D models with applied lines used for investigation on the distribution of the electric field intensities and their dependence on applied voltage, Figure A.2.

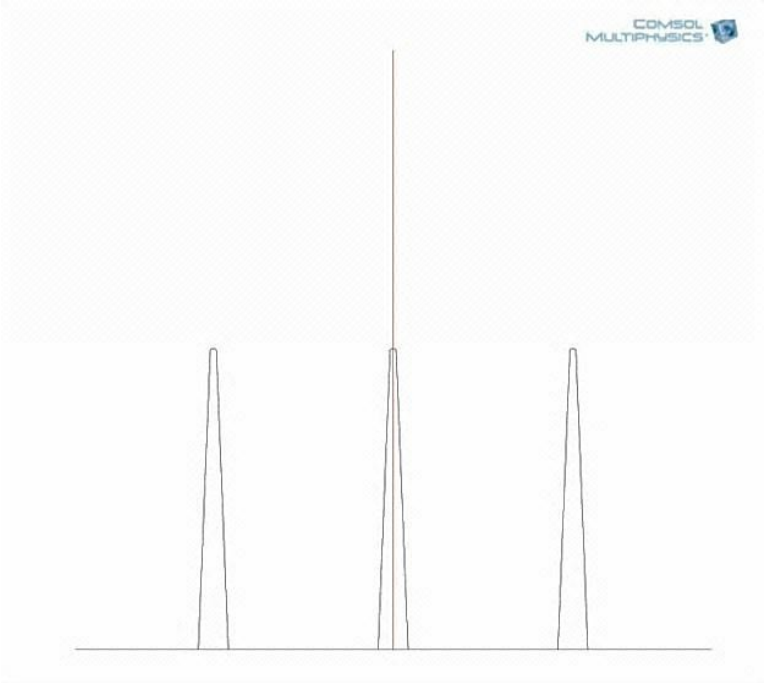

a)

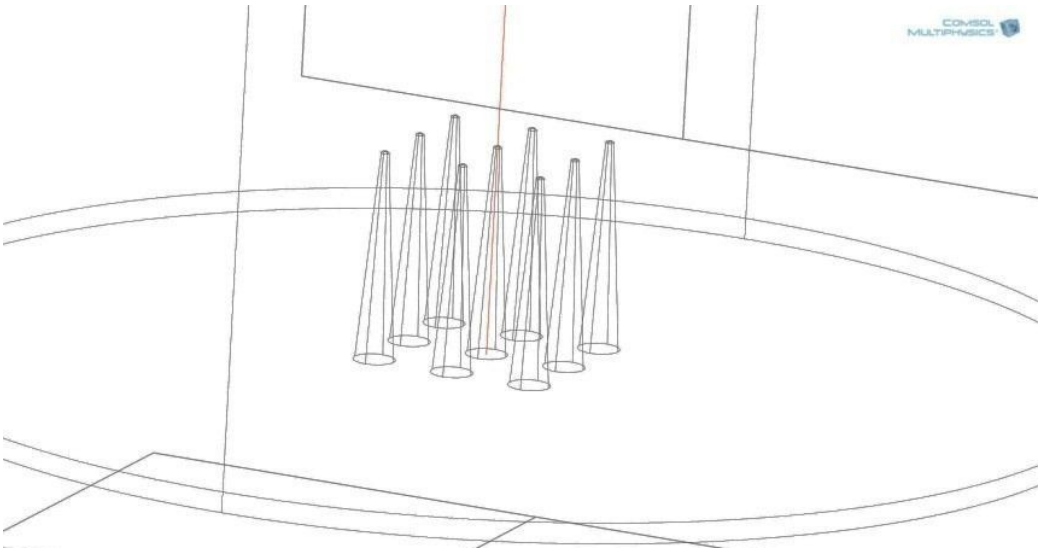

b)

Figure A.2. a) Chosen path for the electric field assessment with 500 nm space between NWs in 2D model, b) schematic of the studied path in 3D model.

The investigation was performed in the middle of the nanowire located in the middle of the 2D model and 3D model.

A.3. Novel GISs: Fabrication, Characterization and Experimental Results

Electrochemical growth parameters employed to grow ZnO NWs for integration into GISs are recorded in Table A.1.

Table A.1. Electrochemical parameters used to grow ZnO NWs integrated into GISs.

Substrate	Chemicals	Concentration [mM]	Applied voltage [V]	Growth temperature [°C]	Growth time [min.]
Porous Silicon	$Zn(NO_3)_2 \cdot 6H_2O$ $C_6H_{12}N_4$	6.3 6.3	-1.0	77	90
n^+-type Si	$Zn(NO_3)_2 \cdot 6H_2O$ $C_6H_{12}N_4$	5.4 5.4	-1.0	80	45
n-type Si	$Zn(NO_3)_2 \cdot 6H_2O$ $C_6H_{12}N_4$ $AgNO_3$	5.4 5.4 $4.45 \cdot 10^{-3}$	-1.0	80	30
n^+-type Si	$Zn(NO_3)_2 \cdot 6H_2O$ $C_6H_{12}N_4$ $AgNO_3$	5.4 5.4 $4.45 \cdot 10^{-3}$	-0.8	85	45
Au layer	$Zn(NO_3)_2 \cdot 6H_2O$ $C_6H_{12}N_4$ $AgNO_3$	5.4 5.4 $4.45 \cdot 10^{-3}$	-0.7	85	45

EDXS analysis was performed to confirm the presence of Ag inside ZnO NWs, Figure A.3.

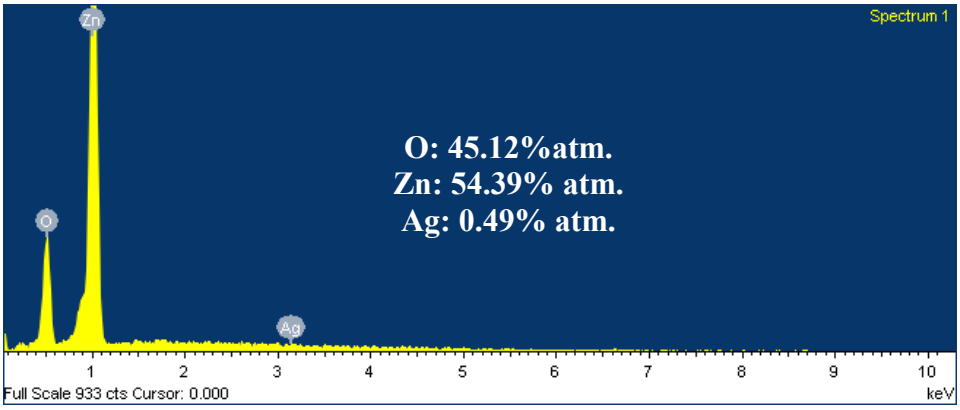

a)

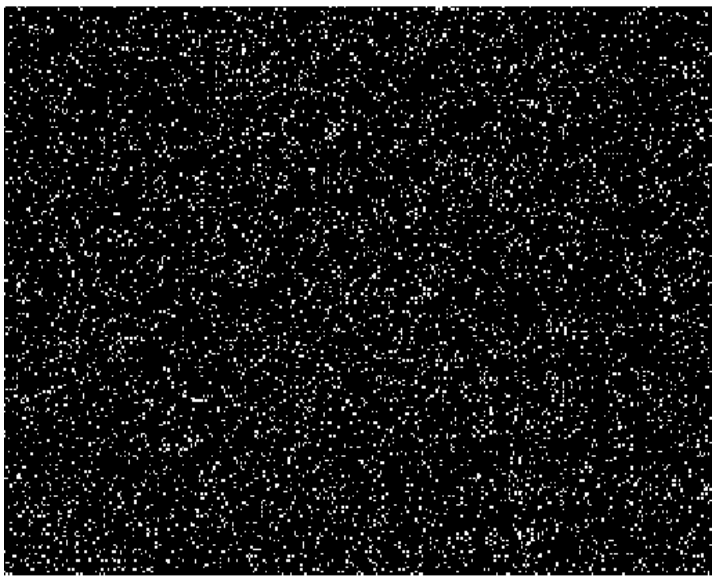

O Ka1

b)

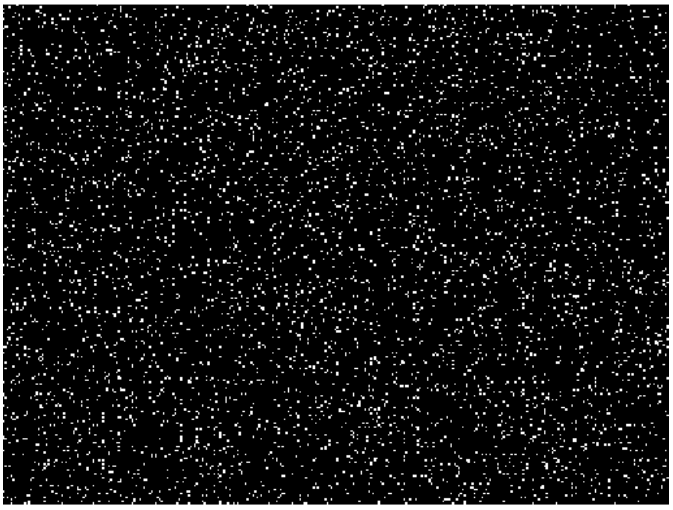

Zn La1_2

c)

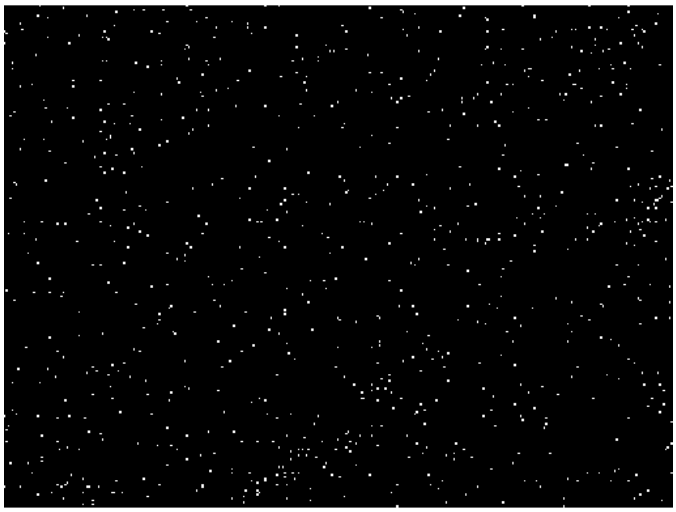

d)

Figure A.3. EDXS analysis of p-type ZnO NWs: a) Spectrum analysis, Mapping analysis: b) distribution of oxygen, c) distribution of Zn and d) distribution of Ag in Ag-doped ZnO NWs.

Energy dispersion X-ray spectroscopy confirmed uniform distribution of Ag in all ZnO NWs. Photoelectrochemical (PEC) tests were used to confirm p-type conductivity of grown ZnO NWs. Applied light on p-type ZnO NWs resulted in decreasing of the potential value inside electrochemical cell. Results of the PEC cell measurements performed on p-type ZnO NWs are illustrated in Table A.2.

Table A.2. PEC cell tests results of p-type ZnO NWs (0.8% of Ag) grown on n-type Si, n^+-type Si, and on Au layer integrated into GISs.

Substrate applied as capacitive plate in GIS	V_{dark} [mV]	V_{light} [mV]	$\Delta V=V_{light}-V_{dark}$ [mV]	Conductive type
n-type Si	-140	-100	40	p
n^+-type Si	-160	-145	15	p
Au layer	-300	-280	20	p

Results of the photoelectrochemical measurements have confirmed that electrochemically

grown Ag-doped ZnO NWs exhibited p-type conductivity. After morphological and material analyses as well as the p-type conductivity confirmation ZnO NWs were incorporated into GISs.

Experimental tests of GIS with p-type ZnO NWs grown on n^+-type Si as positively charged capacitive plate of device in different concentrations of O_2 are illustrated in Figure A.4.

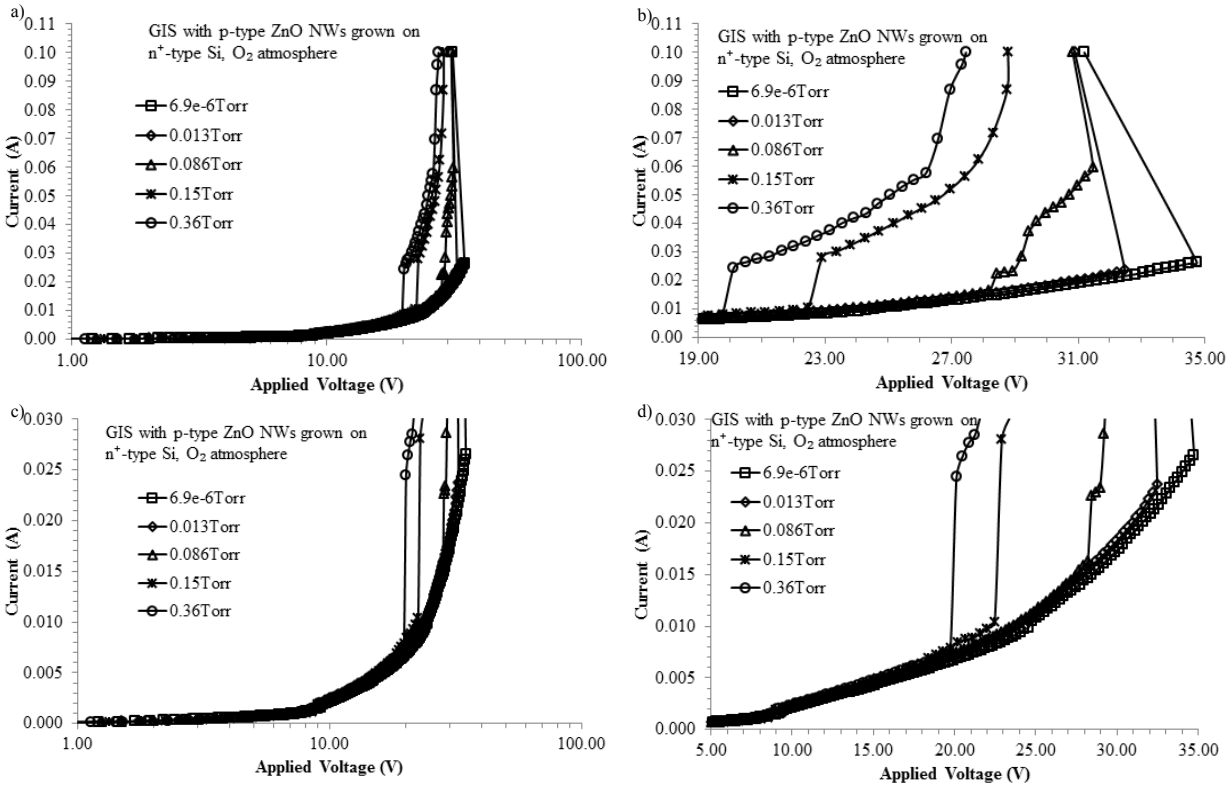

Figure A.4. I-V characteristics of GIS with p-type ZnO NWs grown on n^+-type Si in FI mode for detection of different concentrations of O_2 in vacuum (a - d).

Experimental tests of GIS (p-type ZnO NWs grown on n^+-type Si as positively charged capacitive plate of the gas detector) in different concentrations of N_2 are demonstrated in Figure A.5.

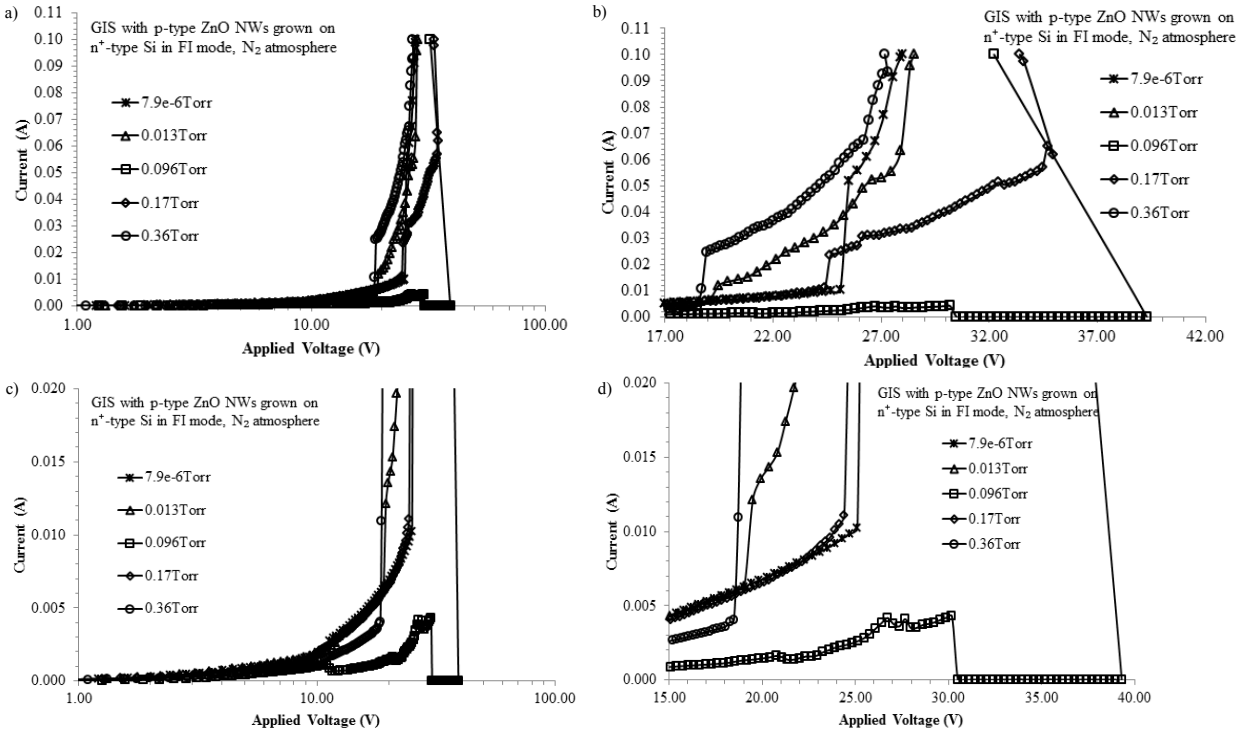

Figure A.5. I-V characteristics of GIS with p-type ZnO NWs grown on n^+-type Si in FI mode for detection of different concentrations of N_2 in vacuum (a - d).

Following, I-V characteristics of GIS (p-type ZnO NWs grown on n^+-type Si as anode of gas detector) in different concentrations of He are shown in Figure A.6.

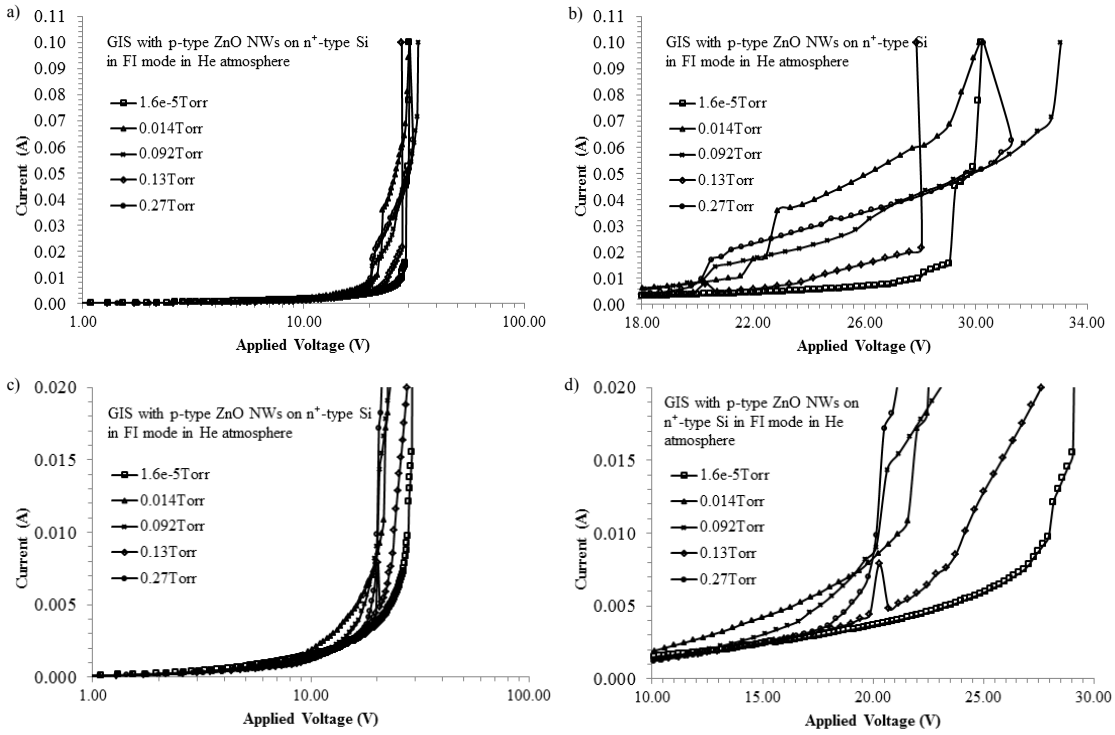

Figure A.6. I-V characteristics of GIS with p-type ZnO NWs grown on n^+-type Si in FI mode for detection of different concentrations of He in vacuum (a - d).

Subsequent, I-V characteristics of GIS (p-type ZnO NWs grown on n^+-type Si as anode) in different concentrations of Ar are reported in Figure A.7.

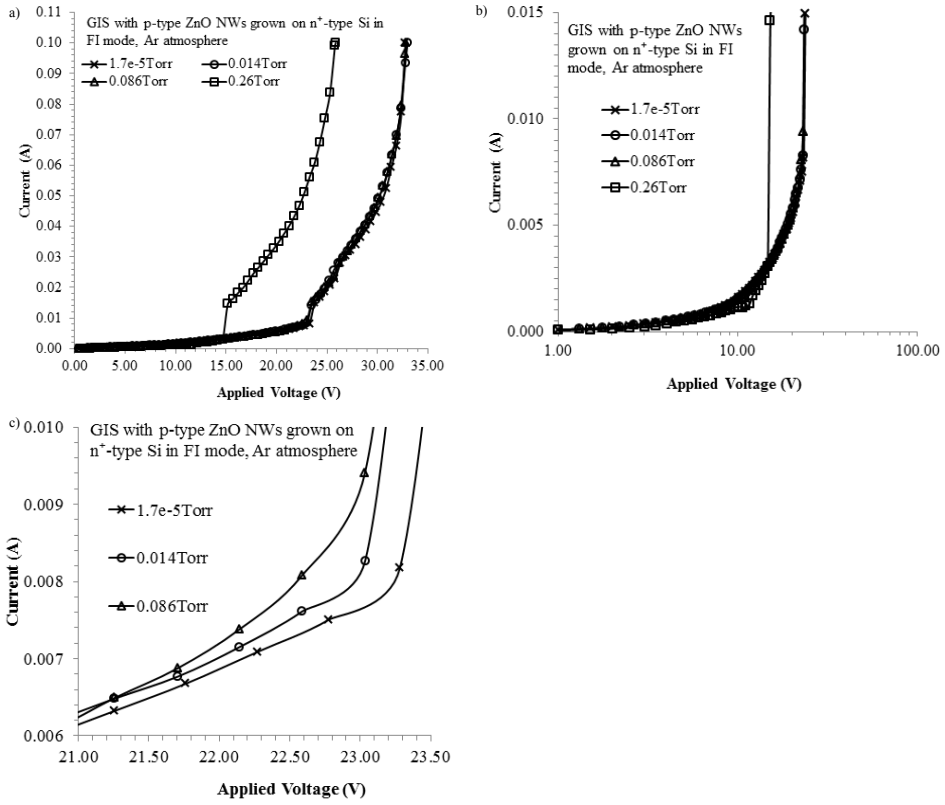

Figure A.7. I-V characteristics of GIS with p-type ZnO NWs grown on n^+-type Si in FI mode for detection of different concentrations of Ar gas in vacuum (a - c).

In all tests the breakdowns in GIS were at high ionic currents. Finally, experimental results on detection of the low concentrations of He, N_2, and O_2 by GIS (p-type ZnO NWs grown on n^+-type Si as anode of gas detector) obtained in field-limited regime, Figure A.8.

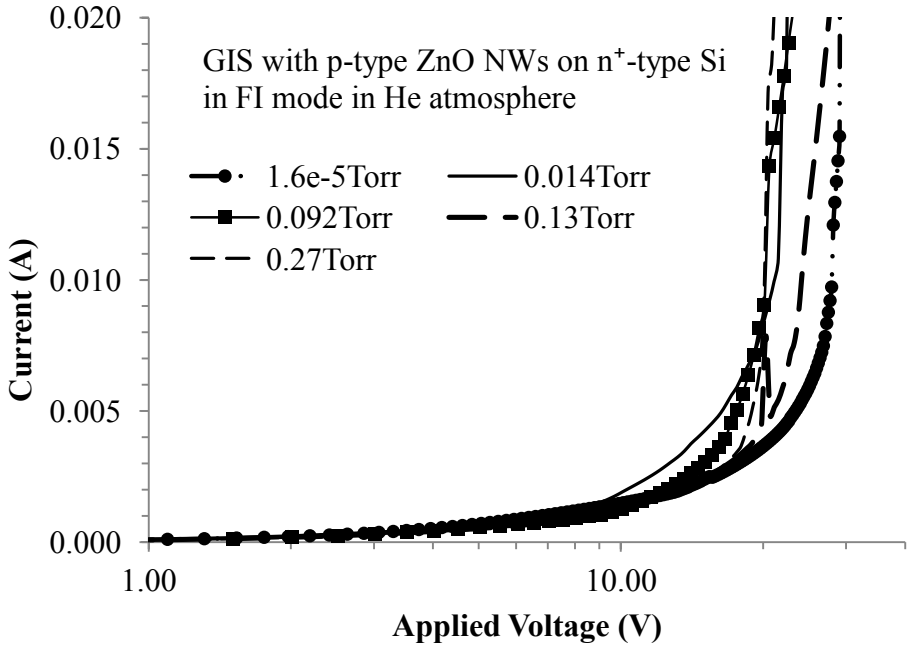
GIS with p-type ZnO NWs on n+-type Si
in FI mode in He atmosphere
1.6e-5Torr
0.014Torr
0.092Torr
0.13Torr
0.27Torr
Current (A)
0.020
0.015
0.010
0.005
0.000
1.00
10.00
Applied Voltage (V)

a)

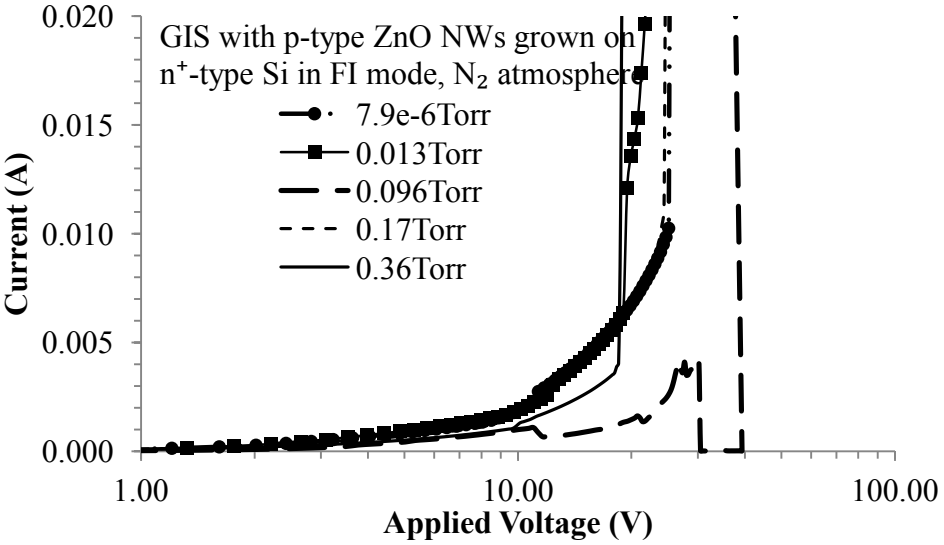
GIS with p-type ZnO NWs grown on
n+-type Si in FI mode, N2 atmosphere
7.9e-6Torr
0.013Torr
0.096Torr
0.17Torr
0.36Torr
Current (A)
0.020
0.015
0.010
0.005
0.000
1.00
10.00
100.00
Applied Voltage (V)

b)

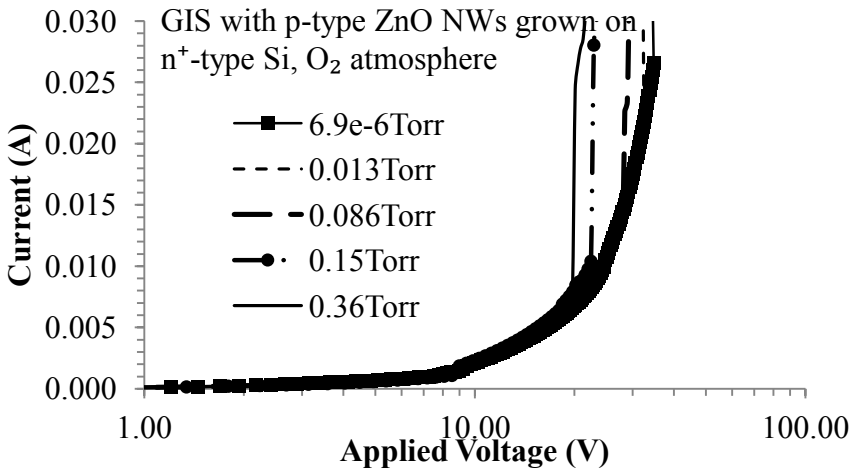

c)

Figure A.8. I-V characteristics of GIS with p-type ZnO NWs grown on n^+-type Si in FI mode for detection of different concentrations of He in vacuum (a), I-V characteristics of GIS with p-type ZnO NWs grown on n^+-type Si in FI mode for detection of different concentrations of N_2 in vacuum (b), I-V characteristics of GIS with p-type ZnO NWs grown on n^+-type Si in FI mode for detection of different concentrations of O_2 in vacuum (c).